University of Alberta

Time-resolved terahertz spectroscopy of bulk and nanoscale semiconductors

by

David G. Cooke ©

A thesis submitted to the Faculty of Graduate Studies and Research in partial fulfillment of the requirements for the degree of Doctor of Philosophy

Department of Physics

Edmonton, Alberta
Spring 2007

Library and Archives Canada

Published Heritage Branch

395 Wellington Street
Ottawa ON K1A 0N4
Canada

Bibliothèque et Archives Canada

Direction du Patrimoine de l'édition

395, rue Wellington
Ottawa ON K1A 0N4
Canada

Your file Votre référence
ISBN: 978-0-494-29659-2
Our file Notre référence
ISBN: 978-0-494-29659-2

NOTICE:
The author has granted a non-exclusive license allowing Library and Archives Canada to reproduce, publish, archive, preserve, conserve, communicate to the public by telecommunication or on the Internet, loan, distribute and sell theses worldwide, for commercial or non-commercial purposes, in microform, paper, electronic and/or any other formats.

The author retains copyright ownership and moral rights in this thesis. Neither the thesis nor substantial extracts from it may be printed or otherwise reproduced without the author's permission.

AVIS:
L'auteur a accordé une licence non exclusive permettant à la Bibliothèque et Archives Canada de reproduire, publier, archiver, sauvegarder, conserver, transmettre au public par télécommunication ou par l'Internet, prêter, distribuer et vendre des thèses partout dans le monde, à des fins commerciales ou autres, sur support microforme, papier, électronique et/ou autres formats.

L'auteur conserve la propriété du droit d'auteur et des droits moraux qui protège cette thèse. Ni la thèse ni des extraits substantiels de celle-ci ne doivent être imprimés ou autrement reproduits sans son autorisation.

In compliance with the Canadian Privacy Act some supporting forms may have been removed from this thesis.

While these forms may be included in the document page count, their removal does not represent any loss of content from the thesis.

Conformément à la loi canadienne sur la protection de la vie privée, quelques formulaires secondaires ont été enlevés de cette thèse.

Bien que ces formulaires aient inclus dans la pagination, il n'y aura aucun contenu manquant.

Canada

To

my grandfather, Michael Prestara, for teaching me many things I could never learn in school.

Abstract

The nature of charge carrier dynamics and conduction in bulk and nanoscale semiconducting materials is investigated with time-resolved terahertz (THz) spectroscopy (TRTS). This powerful technique uses picosecond (10^{-12} s) pulses of far-infrared light to map the electrodynamic response of a photoexcited material in the 0.2 - 3 THz (10^{12} Hz) frequency range on ultrafast time scales.

We show how TRTS can be used to extract the complex conductivity of a material induced by a femtosecond pump pulse, just picoseconds after excitation. A case study of a standard III-V semiconductor, GaAs, is presented to establish a baseline for TRTS in the Ultrafast Spectroscopy lab at the University of Alberta.

Fundamental conduction mechanisms are investigated in dilute nitride and bismide alloys of GaAs, materials of interest for optoelectronic devices. We find that while both nitrogen and bismuth incorporation reduces the fundamental energy bandgap of GaAs, bismuth does so without deteriorating the electrical properties whereas nitrogen severely reduces the electron mobility, limiting its usefulness in future devices. This is the first measurement of electron mobility in GaAsBi, and the results should have a significant impact on the optoelectronic device community.

The inherent sensitivity of the THz pulse to the conductivity of a material, sub-picosecond resolution, and noncontact nature make time-resolved terahertz spectroscopy an ideal technique for investigating carrier capture dynamics in semiconductor nanostructures. In this work, we demonstrate how THz pulses can be used to monitor this capture process directly in both quantum dot and quantum wire structures. We further show how the THz polarization can be used to probe

a photoconductive anisotropy arising from a linear ordering of both quantum wire and dot-chain systems.

Finally, we investigate how the confinement of charge carriers influences the electrodynamics of silicon films by varying the degree of structural disorder. A transition from free to localized behaviour is observed from bulk, crystalline silicon to silicon nanocrystals embedded in glass. The transition from metal-to-insulator can be observed directly as a suppression of the low frequency real conductivity, and can be explained using a model based on carrier backscattering.

Acknowledgements

I have had the pleasure of knowing and working with many people during my time at the University of Alberta, all of whom I am indebted to.

I am extremely grateful to my Ph.D. supervisor, Dr. Frank A. Hegmann, for all of his support and advice over the last five years. Through his countless hours of guidance in the lab, in his office and on the barstool, I have benefited both scientifically and personally. It was an honour to learn about THz research from Frank. FD.

I am very thankful to Dr. Oksana Ostroverkhova, whose verve and vigor in the lab was an inspiration to watch. The countless hours we spent watching noise become a signal taught me the definition of perseverance. Also, she has forever included *Black Friday* on all of our calendars.

I want to thank Dr. Markus Walther, whom I thoroughly enjoyed working with while he was a post-doc in our lab. He is an excellent physicist whose knowledge of THz science is paralleled only by his love of beer and mountains. And perhaps his inability to catch a fish, but one day we will fix that.

Thanks to all the current and former members of the Hegmann lab, especially to Dr. Kris Lui, Jianbo Gao, Grey Arnup and Andrzej Tomalik. I want to extend a special thanks to the Slepkovs, Aaron and Emily, who have been with me every step of the way. As my office and lab mate, Aaron and I had conversations that knew no boundaries, whether it was science, wine, politics...the list goes on. He is a true friend and an excellent physicist, whom I am honoured to have worked with.

It has been a privilege collaborating with Dr. Matthew B. Johnson, Dr. Greg Salamo, Dr. Al Meldrum, Dr. Quan Li, and Dr. Tom Tiedje, as well as members of their groups.

I'd like to thank the fantastic technical staff, especially Don Mullin for his genius solutions to so many problems in the lab. Many thanks to Greg Popowich, Tony Walford, Yolande Peske, Steve Rogers, Jay Haverstock, Jim MacKinnon and the machine shop gurus. Also many thanks to the administrative staff in the office, especially Sarah Derr.

I have had the opportunity to learn from several amazing teachers over the

years. In particular, I want to thank Dr. Frank Marsiglio, Dr. John Beamish and Dr. Andrzej Czarnecki for their insightful lectures on condensed matter physics and quantum mechanics.

Thank you to all the great friends I've made here over the years, especially Brad Schultz for the many, many hours of distractions. I'd also like to single out Allan MacDairmid and James Day, thanks guys.

Finally, I'd like to thank my parents, Milton and Michelle and my brother Michael for their unwavering support throughout my Ph.D. and life in general, and my fiancee Nicole MacDonald for her love and understanding while I wrote this thesis.

Table of Contents

I Terahertz spectroscopy 1

1 Introduction 2

2 Terahertz pulses 8
- 2.1 Generation . . . 8
- 2.2 Detection . . . 13
- 2.3 Ti:sapphire multipass amplified femtosecond laser system . . . 16
- 2.4 THz spectrometer with pump-probe capability . . . 18

3 Terahertz time-domain spectroscopy (THz-TDS) 21
- 3.1 Fresnel equations . . . 22
- 3.2 Substrate characterization . . . 24

4 Time-resolved terahertz spectroscopy (TRTS) 27
- 4.1 Methodology . . . 28
  - 4.1.1 One-dimensional scans . . . 28
  - 4.1.2 Two-dimensional scans . . . 35

II Theoretical models for conductivity in materials 39

5 Models of ac conductivity 40
- 5.1 Free carrier response - Drude model . . . 40
- 5.2 Localized carrier response - Lorentz model . . . 45
- 5.3 Carrier backscattering - Drude-Smith model . . . 48
- 5.4 Sources of carrier scattering . . . 53
  - 5.4.1 Defect scattering . . . 53
  - 5.4.2 Carrier-carrier scattering . . . 54
  - 5.4.3 Phonon scattering . . . 54

III Experimental Results and Discussion **56**

6 Gallium arsenide - A case study **57**
6.1 GaAs - Insulating state 57
6.2 GaAs - Photoconductive state 62

7 Isovalently doped gallium arsenide alloys **70**
7.1 Introduction to isovalent III-V alloys 70
7.1.1 GaN_xAs_{1-x} 71
7.1.2 A new alloy: $GaAs_{1-x}Bi_x$ 73
7.2 TRTS study of dilute GaAs nitrides and bismides 74
7.3 Conclusions 80

8 Electrodynamics of nanostructures **83**
8.1 Characteristic transport length scales 83

9 Quantum wire heterostructures **86**
9.1 Samples 87
9.2 Anisotropic photoconductivity 88
9.3 Temperature dependence 90
9.4 Conclusions 97

10 Quantum dot-chain heterostructures **98**
10.1 Introduction 98
10.2 Sample 100
10.3 Anisotropic photoconductivity 100
10.4 Temperature dependence 104
10.5 Fluence dependence 107
10.6 Conclusions 108

11 Silicon nanocrystals in SiO_2 **110**
11.1 Introduction 110
11.2 SiO_x (x = 1) Samples 112
11.3 Pump absorption 113
11.4 Carrier dynamics 115
11.4.1 Dispersive transport 115
11.4.2 Photoconductive decay 116
11.5 THz electrodynamics 121
11.6 SiO_x (x = 0 to 1.2) samples 130
11.6.1 Carrier dynamics of SiO_x films 133
11.7 Summary 135

IV Conclusions 137

Bibliography 140

A Experimental considerations 155
A.1 Water absorption 155
A.2 Time-domain filtering 157
A.3 Spatial filtering 157
A.4 Conditioning of the pump beam 161
A.5 Conductivity regimes 161
A.6 THz-TDS extraction program 163
A.7 Relation between optical parameters 165

B Walk-through tutorial 166
B.1 The laser system 166
B.2 Obtaining a THz pulse 167
B.3 One-dimensional scan 168
B.4 Two-dimensional scan 169
B.5 Data analysis 170

List of Symbols

Terahertz	THz
Time-resolved terahertz spectroscopy	TRTS
Terahertz time-domain spectroscopy	THz-TDS
Differential terahertz transmission	ΔT
Differential terahertz waveform	ΔE
Reference terahertz waveform	E_{ref}
Pumped terahertz waveform	E_{pump}
Titanium doped sapphire	Ti:sapphire
Complex conductivity	$\tilde{\sigma}$ $[\Omega\ \mathrm{cm}]^{-1}$
Real conductivity	σ_1 $[\Omega\ \mathrm{cm}]^{-1}$
Imaginary conductivity	σ_2 $[\Omega\ \mathrm{cm}]^{-1}$
Complex dielectric function	$\tilde{\epsilon}$
Real dielectric function	ϵ_1
Imaginary dielectric function	ϵ_2
Complex index of refraction	$\tilde{n}$
Substrate index of refraction	N
Real index of refraction	n
Extinction coefficient	κ
Field absorption coefficient	α $[\mathrm{cm}^{-1}]$
Field reflection coefficient	r
Angular frequency	ω $[\mathrm{s}^{-1}]$
Mobility	μ $[\mathrm{cm}^2/\mathrm{Vs}]$
Plasma frequency	ω_p $[\mathrm{s}^{-1}]$
Scattering time	τ [s]
Speed of light and backscattering parameter	c [m/s or unitless]
Permittivity of free space	ϵ_0 [F/m]
Permeability of free space	$\mu_0[\mathrm{N/A}^2]$
Electric field	$\vec{E}$ [V/m]
Magnetic field	$\vec{H}$ [A/m]
Displacement field	$\vec{D}$ $[\mathrm{C/m}^2]$
Magnetic flux density	$\vec{B}$ [T]

Free charge density	ρ [C/m^3]
Electric susceptibility	χ
Polarization vector	$\vec{P}$ [C/m^2]
Current density vector	$\vec{J}$ [C/cm^2 s]
Effective mass	m^* [kg]
Electric charge	e [C]
Electron-hole	e-h
Gallium arsenide	GaAs
Gallium arsenide nitride	GaNAs
Gallium arsenide bismide	GaAsBi
Silicon nanocrystal	Si-NC
Zinc telluride	ZnTe
Molecular beam epitaxy	MBE
Transmission electron microscopy	TEM
Quantum dot	QD
Quantum wire	QWR
Quantum well	QW
Full-width at half-maximum	FWHM
Beam waist	w [m]
Signal-to-noise ratio	S/N
Longitudinal optical	LO
Transverse optical	TO
Monolayer	ML
Wetting layer	WL

List of Tables

5.1 Drude scattering time for various materials (adapted from [1]). . . . 43

7.1 The extracted electron mobility from Drude fits to the complex conductivity in various samples for early t = 10 ps, with a 400 nm pump fluence of 3.7 $\mu J/cm^2$. ($n \sim 2-3 \times 10^{18}\ cm^{-3}$) †Derived from high frequency fits to the Drude model. 79

11.1 Parameters for the Drude-Smith fits in Figs. 11.9 and 11.10. 122

A.1 Relationships between complex optical parameters, given in SI units. 165

List of Figures

1.1 THz Gap. 3
1.2 (a) Typical THz pulse with baseline noise and pulse width indicated. The lock-in time constant was 30 ms, and three scans were averaged. (b) Power spectrum of the THz pulse in (a). 5

2.1 a) Photoconductive switch and b) optical rectification technique for generating THz pulses. 9
2.2 (a) The time varying electric field and resultant polarization due to an optical rectifying process. (b) The emitted THz electric field from the polarization transient in (a), according to Eq. 2.7. 12
2.3 Detected THz electric field dependence on the azimuthal angle of the 0.5 mm ZnTe source crystal. The line is a fit to the function $E_{THz} \propto \cos(3\theta)$-$\cos(\theta)$. 13
2.4 Schematic of ZnTe crystal orientation used to obtain the data in Fig. 2.3. 14
2.5 Schematic of a) photoconductive and b) free-space electro-optic detection of THz pulses. 14
2.6 Schematic of the femtosecond pulse laser system in the Ultrafast Spectroscopy Laboratory in the Department of Physics at the University of Alberta. 17
2.7 Schematic of time-resolved terahertz spectroscopy setup in the Ultrafast Spectroscopy Lab at the Department of Physics, University of Alberta. 18
2.8 (a) Three dimensional schematic and (b) photograph of the time-resolved terahertz spectroscopy setup in the Ultrafast Spectroscopy Lab at the Department of Physics, University of Alberta. 19

3.1 Electric and magnetic field vectors after reflection and transmission of an incident electromagnetic wave incident on a semi-infinite (thickness $\gg \lambda$) non-conducting (no free carriers) surface. 22

3.2 Schematic showing the labeling of regions in thick slab geometry used for extraction of the complex index of refraction of a material using THz-TDS. 24
3.3 Time domain data for a THz pulse traversing air (E_{ref}) and a 0.5 mm thick piece of sapphire (E_{sample}). Note that the large amount of post-pulse ringing is likely due to the amplifier compressor setting not being optimized. 25
3.4 Extracted index of refraction for a 0.5 mm thick sapphire substrate. 26

4.1 Schematic of time-resolved terahertz spectroscopy one-dimensional scan modes. 29
4.2 Electric and magnetic field vectors after reflection and transmission of an incident electromagnetic wave incident on a thin conducting film (d $\ll \lambda$). 30
4.3 Test of the validity of the thin film equation for four films: 10 nm and 30 nm thick gold films ($\omega_p = (2\pi)2.175 \times 10^{15}$ Hz, $\tau = 20$ fs), GaAs photoexcited with 800 nm pump ($\delta_{800nm} = 1\mu$m, n = 1×10^{18} cm^{-3}, $\tau = 100$ fs), and GaAs photoexcited with 400 nm pump ($\delta_{400nm} = 15$ nm, n = 1×10^{17} cm^{-3}, $\tau = 300$ fs). Shown is the (a) film conductivity (closed symbols - σ_1, open symbols - σ_2), (b) film index of refraction and (c) the ratio of film thickness to THz wavelength in the film. 32
4.4 Time domain data for transient spectroscopy on GaAs photoexcited with a 400 nm, F = 2μJ/cm^2, 20 ps after excitation at T = 10 K. . 36
4.5 (a) Amplitude and (b) phase of the complex transmission function derived from Fourier transforms of the $E_{pump}(t)$ and $E_{ref}(t)$ waveforms in Fig. 4.4. (c) The extracted complex conductivity. The solid lines are fits to the Drude model, using parameters given in (c). 38

5.1 Complex conductivity according to the Drude model. Inset is a plot of the Drude conductivity in the $\omega\tau \ll 1$ limit. 42
5.2 Spectral features expected for various materials based on the Drude model and literature scattering times given in Table 5.1, probed in the TRTS bandwidth of 0.2 - 3 THz. 44
5.3 Conductivity of a thin film on a GaAs insulating substrate in (a) the $\omega\tau \ll 1$ limit and (c) the $\omega\tau \sim 1$ regime. The calculated change in THz pulse transmission is given in (b) and (d) for the film conductivity in (a) and (c), respectively. 45

5.4 Lorentz conductivity of a thin film on a GaAs insulating substrate in (a) the underdamped ($\omega_0/2\pi$ = 3 THz, τ = 150 fs) and (c) the overdamped ($\omega_0/2\pi$ = 3 THz, τ = 15 fs) regime. The insets show the current response function, demonstrating the degree of dampening. The calculated change in THz pulse transmission using Eq. 5.8 is given in (b) and (d) for the film conductivity in (a) and (c), respectively. 47

5.5 (a-d) Drude-Smith conductivity for plasma frequency $\omega_p = 4 \times 10^{14}$ s^{-1}, scattering time τ = 10 fs and backscattering parameter ranging from 0 to -1 using Eq.'s 5.17 and 5.18. (e-h) Predicted changes in THz transmission through a 1 micron thick film on glass substrate, with the film conductivity corresponding to the plots in (a-d), using the complex transmission function calculated from the conductivities and Eq. 5.8. 51

5.6 Position autocorrelation function for the Drude-Smith model, derived by integrating Eq. 5.19 for three values of the backscattering parameter c. 52

6.1 Schematic of the band structure of GaAs, with energy gaps and satellite valleys indicated, as well as inter-band and intra-band transitions. Adapted from Ref. [2]. 58

6.2 THz-TDS reference (no sample) and sample (1.83 mm thick GaAs slab) scans. 59

6.3 Amplitude and phase data from the Fourier transform of the waveforms in Fig. 6.2 59

6.4 Transmission coefficient and phase difference for the waveforms given in Fig. 6.2 60

6.5 Extracted real (n) and imaginary (k) parts of the complex index of refraction for a 1.83 mm-thick SI GaAs using THz-TDS. 60

6.6 Extracted complex conductivity for a 1.83 mm-thick SI GaAs using THz-TDS. Lines are fits to the real and imaginary parts of the Lorentz model, with oscillator frequency $\omega_0 = 8.4 \pm 0.1$ THz and lifetime τ = 2 ps. 61

6.7 TRTS time domain data for a SI GaAs sample, 20 ps after 400 nm photoexcitation at 10 K, with extracted complex conductivity. Pump fluence is (a,b) 0.25, (c,d) 1.0 and (e,f) 2.0 $\mu J/cm^2$. The lines over the conductivity data are simultaneous Drude fits to σ_1 and σ_2 with parameters given in the figures, assuming an electron effective mass of 0.067 m_e. 64

6.8 Optical parameters extracted for GaAs photoexcited with 2.0 $\mu J/cm^2$ of 400 nm light, 20 ps after excitation, at 10 K. Shown is the a) optical conductivity, b) dielectric function, c) complex index of refraction and d) reflection and absorption coefficient, calculated using the relations given in Table A.1 in Appendix A.7. The solid and dashed lines are Drude fits to the real and imaginary parts of the optical parameters with plasma frequency $\omega_p/2\pi = 72.6$ THz and a scattering time $\tau = 264$ fs. 65

6.9 a) Ratio of imaginary to real part of the complex conductivity for 800 nm photoexcited GaAs at room temperature. Carrier densities are indicated and the lines are least squares linear fits to the data. b) Extracted scattering rates for the various carrier densities, and a linear least squares fit to the data showing the increase in carrier-carrier scattering, roughly linear with excitation, and the intercept phonon scattering rate of 3 ± 1 THz 66

6.10 (a) Normalized negative differential THz transmission after 800 nm and 400 nm excitation at room temperature under similar pump powers. The solid lines are fits to the spatially integrated solution to Eq. 6.1 with parameters given in (c) and (d). (b) Rise times of the scans shown in (a). The solution for the diffusion equation given in Eq. 6.1 is plotted for (c) 800 and (d) 400 nm excitation, respectively, with parameters given in the plot. 68

7.1 Schematic of GaAsN band structure, showing the resonant N level with the conduction band, and the resultant splitting into upper (E_+) and lower (E_-) bands. 72

7.2 Negative differential THz transmission ($-\Delta T/T_0$) for the GaAs buffer layer (solid black), GaAsBi (0.84 % Bi) (dashed), GaNAs (0.84 % N) (dotted) and GaNAsBi (0.85% N, 1.4% Bi) (grey) samples, at a pump fluence of 3.7 $\mu J/cm^2$. The open symbols are carrier densities normalized to the peak $-\Delta T/T_0$, derived from the Drude fits to the complex conductivity for the GaAs buffer (o), and GaAsBi (Δ) samples. Inset is the same data on a semi-log plot. 75

7.3 Extracted complex conductivity for a) GaAs buffer layer, b) GaAsBi (0.84% Bi) c) GaNAs (0.84% N) and d) GaNAsBi (0.85% N, 1.4% Bi) 10 ps after 400 nm excitation at a fluence of 3.7 $\mu J/cm^2$. The solid and dashed lines are fits to the real and imaginary Drude conductivity with a)$\omega_p/2\pi = 46 \pm 1$ THz , $\tau = 157 \pm 7$ fs, b) $\omega_p/2\pi = 57 \pm 1$ THz, $\tau = 115 \pm 4$ fs, c) $\omega_p/2\pi = 48 \pm 2$ THz, $\tau = 35 \pm 3$ fs, d) $\omega_p/2\pi = 86 \pm 2$ THz, $\tau = 12 \pm 1$ fs. 77

7.4 The time evolution of carrier mobilities extracted from Drude fits to complex conductivity data after 400 nm, 3.7 $\mu J/cm^2$ excitation. The electron effective mass is assumed to be that of bulk GaAs, m*=0.067 me. 78

7.5 Calculated carrier density profiles 4, 10, 20, 50 and 100 ps after 400 nm pump excitation, assuming an infinite surface recombination velocity, a pump penetration depth of 15 nm and an ambipolar mobility of 100 cm^2/Vs. Inset is the percentage of carriers reaching a distance of 200 nm, i.e. to the substrate, obtained by taking the ratio of the integrated density profiles beyond 200 nm to the integration to infinity. 80

9.1 TEM images of a 4 ML InGaAs quantum well (a-c) and 6 ML quantum wire (d-f) samples. (a) Plan-view TEM ($0\bar{2}2$ dark field (DF) condition: image contrasts are strain sensitive). (b) X-TEM from the $[2\bar{3}\bar{3}]$ direction ($0\bar{2}2$ bright field (BF) condition: strain sensitive). (c) X-TEM from the $[2\bar{3}\bar{3}]$ direction ($0\bar{2}2$ quasi-kinematical BF condition: chemical sensitive). (d) Plan-view TEM (022 DF condition: strain sensitive), FFT spectrum inset. (e) X-TEM from the $[01\bar{1}]$ direction (002 BF condition: chemical sensitive). (f) X-TEM from the $[2\bar{3}\bar{3}]$ direction (622 DF condition: chemical sensitive), and enlarged image inset. 89

9.2 Schematic of the 4 ML quantum well (QW) and 6 ML (QWR) InGaAs structures. The capping layer has been removed for clarity. . 90

9.3 Normalized differential THz transmission for the (a) 4 ML quantum well (QW) sample and (b) the 6 ML quantum wire (QWR) sample, with THz polarization $\perp$ (•) and $\parallel$ (○) to the wire growth direction. The sample temperature was 50 K and the 400 nm pump fluence was 1.0 $\mu J/cm^2$. 91

9.4 Temperature dependence of the normalized differential THz transmission $-\Delta T$ for the THz polarization $\parallel$ (○) and $\perp$ (•) to the QWR growth direction. 400 nm pump fluence was 1.0 $\mu J/cm^2$. Solid lines are fits to a bi-exponential decays convoluted with a Gaussian response function shown as a dotted line in (a). 92

9.5 Amplitude of the fast (○) and slow (•) $\perp$ component, $A^{\perp}$, from bi-exponential fits to $-\Delta T^{\perp}$ at a pump fluence of (a) 1.0 and (b) 0.6 $\mu J/cm^2$. (c) Temperature dependence of the slow time constant, τ_S, for both $\parallel$ (○) and $\perp$ (•) orientations at a pump fluence of 1.0 $\mu J/cm^2$. 93

9.6 Subtraction of the parallel and perpendicular THz differential transmission decays for temperatures from 275 - 10 K (a-f) after 1.0 μJ/cm^2, 400 nm excitation. Smooth, dark lines are fits to the data using the two-level model described in the text. 95
9.7 Schematic of the simple model of carrier capture described in the text. 96
9.8 Temperature dependence of the extracted capture times, τ_c, from the fits in Fig. 9.6. 96

10.1 (a) TEM image of QD sample surface morphology. THz polarization parallel ($\|$) and perpendicular ($\perp$) to the dot chains is indicated. (b) Schematic diagram of the sample (not to scale) showing arrangement of QDs on 1D WLs. (c) Cross-sectional TEM image of the sample showing the vertical ordering of the dots. 101
10.2 Normalized differential THz transmission, -$\Delta T(t)$, at 10 K for the THz polarization $\perp$ and $\|$ to the dot chains. The sample was excited with 400 m pump pulses with a fluence of 1.2 $\mu J/cm^2$. The transient response from SI GaAs is shown for comparison. 101
10.3 Negative differential THz transmission -ΔT/T$_0$ scans of the QD chain sample with the THz pulse polarization aligned $\|$ and $\perp$ to the wire direction, taken at 50 K. The pump wavelength was 547 nm at a fluence of 0.5 $\mu J/cm^2$. 103
10.4 (a) Normalized -Δ T for the THz polarization $\perp$ to the dot chains at three different temperatures, and (b) amplitudes of the fast and slow components. (c) Normalized -Δ T for the $\|$ orientation at three temperatures, and (d) corresponding component amplitudes. The pump fluence was held at 1.2 μ J/cm^2 for all temperatures. 104
10.5 Schematic of the thermal re-emission process with shading representing the carrier population. 105
10.6 (a) Temperature dependence of τ_F, the fast exponential decay time from biexponential fits to the -$\Delta T/T_0$ in both orientations to the QD chains. (b) Temperature dependence of the τ_S, the slow exponential decay time. The pump fluence was 1.2 $\mu J/cm^2$. 106
10.7 -ΔT scans for the (a) $\|$ and (b) $\perp$ orientations at 10 K for the fluences listed. (c) Dependence of the amplitude of the slow component with photoexcited carrier density for each polarization orientation at 10 K. 107
10.8 Schematic explaining the occupancy of the QDs, 1-D WLs and 2-D WLs with increasing fluence labeled with corresponding regions in Fig. 10.7(c). 108

11.1 EFTEM (a-c) and HRTEM (d-f) images of the T_a=900°C (a,d), 1000°C (b,e) and 1100°C (d,f) silicon nanocrystal samples. 113
11.2 Bright-field TEM image of the 200 nm thick poly-nc-Si film. The dark spots correspond to the silicon grain boundaries that have a crystalline axes aligned to diffract into the image plane. 114
11.3 Measured absorbance of Si-NC films annealed at three temperatures. The 900 and 1000°C films were 200 nm thick and the 1100°C film was 1 μm thick. 114
11.4 Pump-induced change in THz pulse transmission for several pump-probe delay times between 5 and 200 ps, demonstrating that although there was a considerable phase shift, this shift was constant for all delay times measured. 116
11.5 Differential THz transmission dynamics, $-\Delta T/T_0$, due to 400 nm excitation for (a) an epitaxial silicon-on-sapphire (SOS) film at a pump fluence of F=30 $\mu J/cm^2$, and (b)(g) Si-NC films (T_a=1100-500°C) at a pump fluence of F=315 $\mu J/cm^2$. 118
11.6 Log-log plots of the differential THz signals shown in Fig. 11.5(a)(e) but over longer time scales and scaled for clarity. The solid lines are fits to the decay dynamics: biexponential for SOS, stretched exponential for Si-NCs with T_a=900, 1000, and 1100°C, and power law for Si-NCs with T_a=800 and 900 °C (dashed). Fit parameters are given in the text. 119
11.7 Normalized differential THz transmission, $-\Delta T$, of the T_a = 1000 °C Si-NC film plotted on a (a) log-lin, (b) log-log and (c) log(-Ln(-ΔT))-log(t) plot. The linear form in (c) demonstrates the decay is of the stretched exponential form. 120
11.8 Normalized negative differential THz transmission, $-\Delta T$, of Si-NC films annealed at 1000°C in H_2 and N_2 (o) and N_2 only (Δ). The solid lines are stretched exponential fits to the data. The inset compares the room temperature photoluminescence (PL) of the two films, excited with both 325 and 442 nm CW laser lines. 122
11.9 Terahertz conductivity spectra showing (a) $\sigma_1(\omega)$ and (b) $\sigma_2(\omega)$ for the SOS film ($\square$) 100 ps after excitation ($30\mu J/cm^2$), poly-nc-Si film (o) 10 ps after excitation (110 $\mu J/cm^2$), and Si-NC films annealed at 900°C (Δ), 1000°C (∇), and 1100°C ($\diamond$) at probe time delays of 4, 10, and 100 ps, respectively ($550\mu J/cm^2$). Solid lines are fits to the Drude-Smith model with parameters given in Table 11.1. 123

11.10Real (open circles) and imaginary (open triangles) parts of the complex conductivity for (a) the SOS film 100 ps after excitation (30 μJ/cm^2), (b) the poly-NC-Si film 10 ps after excitation (110 μJ/cm^2), and (c - e) the Si-NC films annealed at (c) 900 C, (d) 1000 C and (e) 1100 C, 4, 10 and 100 ps after excitation (550 μJ/cm^2), respectively. Solid lines are fits to the Drude-Smith model with parameters given in Table 11.1. 124

11.11Terahertz conductivity spectra for the Si-NC film annealed at 1100°C at probe time delays of 10, 30, 100, and 200 ps after photoexcitation by the 400 nm pump pulse. ($\sigma_1(\omega)$ (open symbols) is positive and $\sigma_2(\omega)$ (filled symbols) is negative.) The solid lines are Drude-Smith fits to the data, with the probe time delay dependence of the corresponding scattering time τ and plasma frequency $\omega_p/2\pi$ shown in (b) and backscatter parameter c shown in (c). The terahertz conductivity spectra at a probe time delay of 5 ps is similar to that at 10 ps and is not shown in (a) for clarity. 127

11.12Complex conductivity data for the T_a = 1100°C film 100 ps after 400 nm excitation at a fluence of 540 $\mu J/cm^2$. The lines are fits to the Drude-Smith (black), Brüggeman EMA (grey) and nearest neighbor tunneling EMA (light grey) models, with solid and dashed lines being σ_1 and σ_2, respectively. 129

11.13Bright field TEM image of SiO_x film with x = 0, annealed at 1000°C. The crystalline grains are visible as dark spots in the image. 131

11.14Negative differential transmission of the SiO_x series with varying Si content from x = 0.0 to x = 1.2 for T_a = 700 and x = 0.2 - 1.2 for T_a = 900 and 1100°C. The 400 nm pump fluence was 580 $\mu J/cm^2$ with the samples at ambient room temperature. 132

11.15Peak negative differential THz transmission of the SiO_x T_a = 900°C film with varying Si content from x = 0.2 to x = 1.2. The 400 nm pump fluence was 580 $\mu J/cm^2$ with the samples at ambient room temperature. 134

11.16Room temperature frequency dependent complex conductivity of the 200 nm thick T_a = 1100°C SiO_x samples with x varying from 0.2 - 0.8, (a) 5 ps and (b) 20 ps after 400 nm excitation at a fluence of 580 $\mu J/cm^2$. 135

11.17Extracted dc conductivity from Drude-Smith fits to the transient complex conductivity of the T_a = 1100°C SiO_x series with x = 0.2 - 0.8 and taken at pump-probe time delays of 5 and 20 ps. 136

A.1 Time domain data of a THz pulse before and after a 40 and 130 minute dry N_2 purge, showing the reduction of post-pulse oscillations related to water absorption. The inset shows the Fourier power spectrum for these pulses, demonstrating the reduction in water absorption. 156

A.2 Comparison plot of the derived conductivity from THz pulses taken without and with a dry N_2 purge, removing atmospheric water vapour from the setup. The sample was a 1 μm thick SiO film on fused silica, annealed at 1000°C in a N_2/H_2 environment after 400 nm excitation. 156

A.3 THz pulse with and without numerical filter (dashed line) in the time domain, and the corresponding power spectrum (inset). 158

A.4 Calculated transmission function from Eq. A.3 for a diffraction-limited Gaussian THz beam with 1/e width defined by Eq. A.2 through several apertures of indicated diameter. The focal length of the focusing off-axis parabolic was 3 inches and the beam diameter before focusing was estimated as 3 cm, values representative of the THz setup used in this study. 158

A.5 Power spectrum of a THz pulse transmitted through three apertures of 1.0, 1.5 and 2.0 mm diameter placed at the beam focus. 160

A.6 Spatial profile across the focus of the THz pulse, measured by knife-edge scanning. The line is a Gaussian fit with $1/e^2$ width of 0.94 mm. 160

A.7 Transient conductivities of (a) GaAs (10 K, 400 nm pump, 1 $\mu J/cm^2$, 20 ps after excitation) and (b) SOS (300 K, 400 nm pump, 30 $\mu J/cm^2$, 100 ps after excitation). Corresponding $E_{ref}(t)$ and $-\Delta E(t)$ waveforms for the (c) GaAs and (d) SOS samples. (e) $-\Delta T/T_0$ scans for both samples, with the time delay of the spectroscopies indicated. 162

B.1 (a) Absolute change in THz peak transmission and (b) negative differential THz transmission as a function of pump-probe delay time, for a bulk GaAs sample at 10 K, with 400 nm pump at a fluence of 2 $\mu J/cm^2$. 169

B.2 (a) Scan for calibration of $-\Delta E(t)$ waveform. (b) Calibrated waveforms, with the point used for calibration indicated by a circle. . . . 170

B.3 Fourier transform (a) amplitude and (b) phase of the waveforms shown in Fig. B.2(b). 171

Part I

Terahertz spectroscopy

Chapter 1

Introduction

As our ability to manipulate matter on the nanometer scale increases, so too does the potential for new and improved devices which take advantage of quantum size effects. Lasers using semiconductor nanostructures as an active medium can be manufactured with lower threshold voltages and better thermal stability than their bulk counterparts, due to the enhanced confinement in a quantum well [3, 4], wire [5] or dot structure [6]. Optoelectronic devices can be tuned to operate at higher frequency because carriers can traverse a shorter distance, increasing the speed at which information can be processed. However, the operation and optimization of these devices depends on the knowledge of how charge carriers behave just picoseconds after optical or electrical injection. With the advent of the femtosecond laser, ultrafast spectroscopy has served as a powerful tool to fill in our understanding of charge carrier dynamics on femtosecond (10^{-15} s) to picosecond (10^{-12} s) time scales. Techniques such as time-resolved photoluminescence, degenerate and non-degenerate pump probe and time-resolved near-field spectroscopy have opened the window into charge generation, recombination and trapping processes, as well as high-field transport, formation of excitons, quasiparticle dressing and many other interesting effects (See Ref. [7] and references therein).

In condensed matter, there are many situations where the energy scales of interest lie in the 0.1 - 20 THz (1 THz = 1×10^{12} Hz) range, including the superconducting energy gap (conventional systems) [8], exciton transitions [9, 10], quasiparticle scattering rates in semiconductors [11, 12], and vibrational modes of large molecules [13] to name a few. Traditionally, to access this energy region of

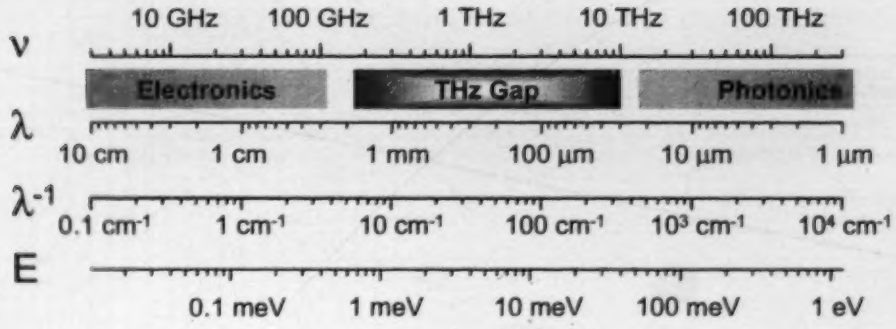

Figure 1.1: THz Gap.

the spectra, one had to resort to relatively weak sources of radiation such as thermal sources or backward-wave oscillators, that use cavity techniques to increase sensitivity, or huge facilities such as free-electron lasers (FEL) or synchrotrons with liquid He-cooled bolometer detection. In the past, the time resolution of pump-probe experiments using these accelerator-based techniques was limited to 100 ps in a pulse-sliced FEL [14] or 200 ps in a pulsed synchrotron source [15]. However, improved control over electron bunches and the development of "femtoslicing" has led to the generation of high power, coherent fs THz synchrotron radiation from a bend magnet [16, 17] and an undulator source [18] that is synchronized to a fs x-ray pulse. Pump-probe experiments have already been performed using these new, intense THz pulses [19].

Because of the lack of convenient, intense sources of THz radiation, very little was known about optical properties of materials in this 0.1 - 20 THz range and thus was coined the term "THz gap", corresponding to this region of the spectrum. Figure 1.1 shows where this THz gap is located in various energy scales, in between the microwave and infrared. Note that this corresponds to the border between the limits of photonics (visible - 50 μm) and electronics (microwave - 100 GHz). When a table-top source of pulsed, sub-picosecond, broadband THz radiation became available nearly two decades ago, THz spectroscopy was born and set its task on filling in this gap. Fig. 1.2(a) demonstrates a typical THz pulse generated and detected using a table-top system, derived from a widely available, amplified

Ti:Al_2O_3 mode-locked laser source with 800 nm, 100 fs output. The first feature of this plot to note is that it is the *electric field*, not the intensity, which is measured due to the development of coherent detection. With both the amplitude *and* the phase information of the electric field of the pulse, spectroscopy could be performed where both real and imaginary components of the optical coefficients are obtained without the use of complicated Kramers-Kronig relations. Note the time scale is in picoseconds, with the FWHM of the main positive peak of the pulse being approximately 0.25 ps wide. The baseline noise level is indicated, giving a rms S/N ratio of ~2000 for the electric field (4×10^6 for power), a testament to the robust coherent detection scheme. The Fourier transform of this pulse given in Fig. 1.2(b) reveals the frequency components of the pulse, stretching from 0.3 - 2.8 THz and covering much of the THz gap. The brightness of this THz source is beyond that of thermal sources, with gated detector sensitivity orders of magnitude better than bolometric detection. Furthermore, the sub-ps width of THz pulses and the inherent time-synchronization with the source laser pulse permit their use in a pump-probe technique, where the probing energy is in the THz gap. The complete amplitude and phase information of the probe pulse E-field allowed full extraction of the complex optical parameters in a static or nonequilibrium state just picoseconds after optical excitation. This allows THz researchers to answer many fundamental questions in semiconductor physics that previously could only be treated theoretically, if possible at all. Two examples of such fundamental studies are the direct observation of the onset of screening of the bare Coulomb interaction in a system of photoexcited electrons and holes [12], and the formation of excitonic states in photoexcited GaAs under resonant and nonresonant excitation [9].

This thesis will focus on applying the powerful technique of time-resolved terahertz spectroscopy (TRTS) to several semiconducting systems, with a specific interest in dilute isovalent alloys of GaAs (GaAsBi and GaNAs) and several nanostructured materials. Since GaAs was one of the first semiconductors characterized by time-resolved terahertz spectroscopy [11], a case study of this material is presented to establish a baseline for full transient frequency-resolved spectroscopy in this lab. The study progresses from standard time-domain spectroscopy of unexcited GaAs, where the dielectric properties are dominated by optical phonons, to photoexcited GaAs, where injected carriers in the conduction band dominate the

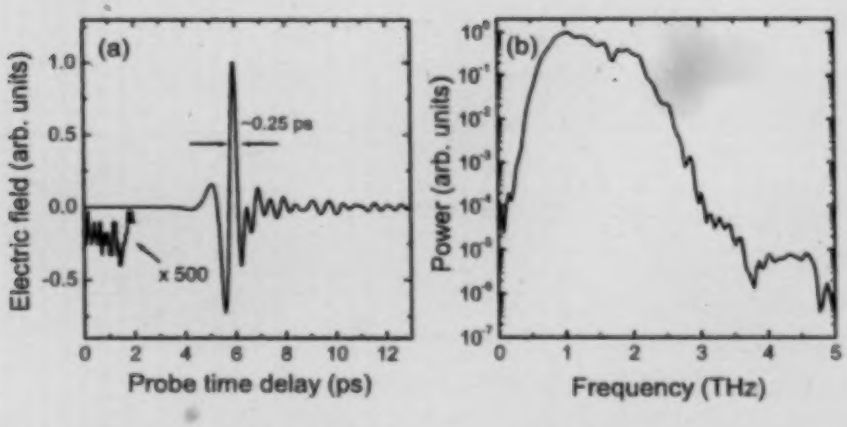

Figure 1.2: (a) Typical THz pulse with baseline noise and pulse width indicated. The lock-in time constant was 30 ms, and three scans were averaged. (b) Power spectrum of the THz pulse in (a).

electrodynamics and are best described as free. A review of the various scattering mechanisms influencing the carrier mobility in GaAs is presented, exploring the effects of temperature and excitation density.

Once the transient electrodynamics of photoexcited GaAs are established, we will investigate how doping with very small amounts of nitrogen and bismuth, isovalent with As, influences the electronic properties of GaAs. Currently, N alloying is very interesting from a technological viewpoint, due to the large bandgap bowing effect observed in dilute GaNAs alloys, where the bandgap energy is reduced drastically by N incorporation of less than 4% into the 1.3 - 1.5 μm range [20]. This energy range is of interest for various telecommunication applications, solar cells [21] and electronic applications such as heterojunction bipolar transistors used in microwave amplifiers, prolific in cellular phone technology [22]. A major drawback concerning the application of GaNAs to devices is that nitrogen reduces the electron mobility considerably due to a resonant interaction of N with the conduction band of GaAs [23, 24], forcing device designers to increase operating voltages. An alternative to GaNAs has arisen in the last two years using the larger Bi dopant,

rather than N, which also shows a bandgap bowing effect that is almost as large as N [25]. We demonstrate, using TRTS, that the electron mobility is largely unaffected by Bi incorporation, presumably because Bi has a resonant interaction with the valence band, rather than the conduction band. Conversely, GaNAs shows a strong deviation from Drude conductivity, including a suppression of the real part of the conductivity at low frequencies corresponding to a disruption of long-range transport. Our results indicate that Bi is an excellent alternative to N in terms of band-gap reduction without compromising electron mobility, a discovery that may impact future devices.

Carrier capture dynamics in III-V based quantum wire and dot structures have been extensively researched in recent years due to their potential for photonic devices such as lasers [6] or photodetectors [26]. These structures are often self-assembled, driven by strain from the active layer lattice mis-match with the substrate. This formation process, known as Stranski-Krastinow, results in the formation of a two-dimensional wetting layer [27]. Often, it is the case that carriers are injected optically or electrically into barrier or wetting layer regions and must be captured into the active dot or wire regions for the device to work. This capture process is therefore intimately tied to the operating characteristics of these devices, and previous work has shown that the capture occurs on a sub-picosecond to tens of picoseconds time scale, depending on the device. Much of this work has used techniques such as time-resolved photoluminescence, time-resolved near-field microscopy and non-degenerate pump-probe techniques, all of which rely on carrier population of the active layer and are insensitive to the processes occurring beforehand. Processes such as exciton formation and relaxation to an emitting state are convoluted with the onset of photoluminescence and require complicated models that rely on an accurate knowledge of the energy levels of the device. We show in this thesis that because TRTS is inherently sensitive to photoconductivity and therefore carrier mobility, it is ideally suited to monitor this capture process into lower mobility states without being convoluted with the processes governing light emission. Furthermore, using the polarization of the THz probe pulse, the intrinsic ordering of laterally aligned samples results in a photoconductive anisotropy which can be used to map out the response of two and one-dimensional carriers, making TRTS an extremely powerful, alternative technique to monitor carrier cap-

ture dynamics in semiconductor nanostructures. Specifically, the capture process of self-assembled and laterally-aligned InGaAs/GaAs (311A) quantum wires and InGaAs/GaAs quantum dots (100) are examined.

Finally, we explore the transient complex conductivity of photoexcited silicon films, with varying degrees of structural disorder driving the system from a Drude conducting material in epitaxial silicon to a near-insulating behaviour in densely packed silicon nanocrystals in glass formed by thermal annealing of silicon-rich oxide. There has been considerable interest in nanocrystalline silicon in recent years, owing to the enhanced optical properties arising from quantum confinement [28]. We show in this thesis that the frequency resolved conductivity response of these nanocrystal films deviates strongly from photoexcited bulk silicon, and can be described quite well with a classical Drude-Smith model where macroscopic transport is limited by carrier backscattering, so charge carriers are only mobile on nanometer length scales. We also show, in agreement with previous transient absorption studies, that the decay of mobile charge carriers is dominated by trapping at non-passivated Si/SiO_2 interface states on a sub-ps to 100 ps time scale, depending on the size of the nanocrystals.

Chapter 2

Terahertz pulses

2.1 Generation

The generation of electromagnetic radiation can be completely described by Maxwell's equations in the presence of a medium. Here, the electric and magnetic field strengths $\vec{E}$ and $\vec{H}$ are altered in the presence of a medium with free charge density ρ to the electric displacement $\vec{D}$ and magnetic induction $\vec{B}$. The equations are

$$\nabla \times \vec{E} + \frac{\partial \vec{B}}{\partial t} = 0 \tag{2.1}$$

$$\nabla \cdot \vec{B} = 0 \tag{2.2}$$

$$\nabla \times \vec{H} = \frac{\partial \vec{D}}{\partial t} + \vec{J} \tag{2.3}$$

$$\nabla \cdot \vec{D} = \rho \tag{2.4}$$

where $\vec{D} = \epsilon \vec{E}$, with ϵ being the dielectric constant, $\vec{B} = \mu \vec{H}$, with μ being the magnetic moment of the material, and $\vec{J}$ is the current density. Combining Eq. 2.1 with Eq. 2.4 using the vector identity $\nabla \times (\nabla \times \vec{A}) = -\nabla^2 \vec{A} + \nabla(\nabla \cdot \vec{A})$ gives

$$\frac{\partial}{\partial t}(\nabla \times \vec{B}) = \nabla^2 \vec{E} - \frac{1}{\epsilon} \nabla \rho \tag{2.5}$$

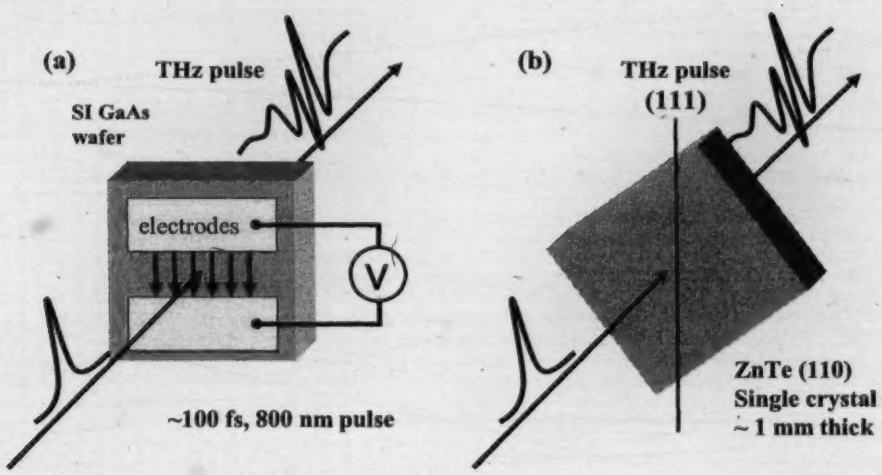

Figure 2.1: a) Photoconductive switch and b) optical rectification technique for generating THz pulses.

that, when combined with Ampère's law Eq. 2.3, and assuming no free charge (ρ=0) gives the wave equation

$$\nabla^2 \vec{E} - \epsilon\mu \frac{\partial^2 \vec{E}}{\partial t^2} = \mu \frac{\partial \vec{J}}{\partial t} \tag{2.6}$$

The right hand side of Eq. 2.6 is the fundamental source of radiation, namely non-uniform motion of charge. We can split this up even further by making the distinction between free and bound charge. Since the current $\vec{J}$ is in general comprised of both conduction $\vec{J}_{cond}$ and bound $\vec{J}_{bound}$ contributions, with $\vec{J}_{bound} = \frac{\partial \vec{P}}{\partial t}$ giving finally

$$\nabla^2 \vec{E} - \epsilon\mu \frac{\partial^2 \vec{E}}{\partial t^2} = \mu \left(\frac{\partial \vec{J}_{cond}}{\partial t} + \frac{\partial^2 \vec{P}}{\partial t^2} \right) \tag{2.7}$$

which is recognized as a wave equation with two source terms, the first derivative of a conduction current, $\partial \vec{J}_{cond}/\partial t$, and the second derivative of a polarization, $\partial^2 \vec{P}/\partial t^2$.

A photoconductive switch was one of the first methods of generating a THz pulse, first pioneered by D.H. Auston in the 1970s [29] but confined to a transmis-

sion line structure, and further developed to freely propagating THz pulses in the 1980s [30, 31, 32, 33, 34]. A schematic of such a switch is given in Fig. 2.1(a). Two conducting electrodes are patterned on a direct-gap semiconducting material, like semi-insulating (SI) GaAs, separated by a typical distance of 30 - 60 μm. A DC bias voltage on the order of 10 V is applied across the electrodes and an above bandgap femtosecond excitation pulse, focused to a $\sim$10 μm spot size near the anode region, creates free electron-hole pairs. Because of a trap-enhanced space-charge region near the anode, large fields exist on the order of 10^6 V/cm resulting in an enhancement of THz radiation by a factor of $\sim$50 over cathode illumination [35]. These charge carriers are accelerated in the bias field and emit a THz pulse in the far field given by $E(t) \propto \partial \vec{J}/\partial t$. The rise time of conductivity in the substrate material is the primary source of radiation which is the reason why high mobility, direct-gap semiconductors are the most popular choices for emitter substrate materials. The THz pulse is typically collected with a hyper-hemispherical silicon lens which is often in contact with the substrate to minimize multiple reflections that can arise from an air gap. Silicon is used because of the excellent index of refraction match between silicon (3.47) and GaAs (3.6) at THz frequencies that minimizes reflection losses, and since Si has almost no dispersion or absorption at THz frequencies. Bandwidths as high as 5 THz have been achieved using photoconductive switches, although they are usually used with high frequency oscillator laser sources ($\sim$ 100 MHz) rather than the low frequency amplified laser systems ($\sim$ 1 kHz). For this reason, very little pump-probe work has been done using switches [36], although in general it is possible.

Large aperture photoconductive switches have been used with amplified laser sources, so that the high energy pulse does not have to be focused down to a micron sized spot, which would exceed the damage threshold of the semiconductor in conventional switches [37]. The drawback is that for fields of $\approx 10^4$V/cm to be attained with a 1 cm spacing, one requires 10 kV across the electrodes. While a technical difficulty, this can be overcome by using pulsed high voltage sources and the current record for THz pulse energy (0.8 μJ, $E_{peak} \approx$ 350 kV/cm at focus) generated by a table-top fs laser source is held by a large aperture switch [38]. Another benefit of this large aperture illumination is the THz output is quasi-collimated, and so a substrate lens is not necessary.

A more popular technique for generating THz pulses with an amplified source is through a second-order nonlinear optical process such as optical rectification. Briefly, nonlinear optics is an extension of the linear optical response of a material to higher order terms which become important only at very high intensities. The polarization response of a material to an applied electric field is

$$P(t) \propto \chi^{(1)}E(t) + \chi^{(2)}E(t)^2 + \chi^{(3)}E(t)^3 + \cdots \tag{2.8}$$

where $\chi^{(n)}$ is the n^{th} order electric susceptability. Heuristically, one can view this higher order response as anharmonicity in the oscillation of charge within the material, which becomes significant only at higher fields (larger amplitude oscillation). These higher-order terms become significant for electric fields attained in femtosecond laser pulses ($\approx 10^7$ V/cm). Second-order effects, such as sum and difference frequency generation and parametric amplification, are routinely observed in the laboratory. The second order polarization response to two photons of frequency ω_1 and ω_2, represented by electric fields $E_1(t)=\cos(\omega_1 t)$ and $E_2(t)=\cos(\omega_2 t)$, is

$$P^{(2)}(t) \propto \chi^{(2)}cos(\omega_1 t)cos(\omega_2 t) = \frac{\chi^{(2)}}{2}cos[(\omega_1+\omega_2)t] + cos[(\omega_1-\omega_2)t] \tag{2.9}$$

with the first term being the sum frequency and the second being the difference frequency. A special case of the difference frequency occurs when $\omega_1 = \omega_2$, and a quasi-dc polarization (optical rectification) is created following the electric field pulse envelope, depicted in Fig. 2.2(a). By Eq. 2.7, an electromagnetic field is emitted according to $E_{THz} \propto \frac{\partial^2 \bar{P}(t)}{\partial t^2}$, as shown in Fig. 2.2(b), which is a THz pulse typically 0.5 ps full-width at half-maximum. The width of the THz pulse being roughly 5 times that of the generating fs pulse is a consequence of dispersion and absorption in the ZnTe crystal. This limits the phase-matching between the 800 nm generation pulse and the THz pulse as it propagates through the crystal, bandwidth-limiting the THz pulse to frequencies less than the TO phonon resonance at 5.3 THz. As a result, the pulse widens in the time domain. In our THz setup, the nonlinear medium is a 0.5 mm thick (110) ZnTe crystal, which has a relatively high second order nonlinearity, little absorption and dispersion in the 0.3 - 3 THz bandwidth. There are, however, two absorptive phonons at 1.6 and 3.7 THz [39]. Other crystals have been used as THz emitters through optical rec-

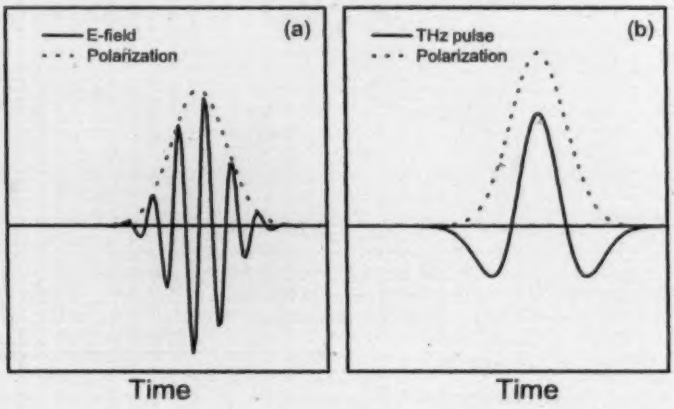

Figure 2.2: (a) The time varying electric field and resultant polarization due to an optical rectifying process. (b) The emitted THz electric field from the polarization transient in (a), according to Eq. 2.7.

tification, such as GaAs, GaP, GaSb, and GaSe. The organic crystal, DAST, has also been used as a THz emitter, with enhanced output in the 7-20 THz range over ZnTe [40]. Recently ultrabroadband THz pulses with bandwidth extending to 41 THz was demonstrated using shorter pulses and an ultrathin GaSe crystal, which minimized the effect of group velocity mismatch through the entire crystal volume of the 800 nm generation beam and the emitted THz radiation [41].

Because $\chi^{(2)}$ is in general a tensor, related to the crystallographic symmetry of ZnTe, the crystal must be oriented correctly with respect to the laboratory frame of reference to maximize the conversion efficiency. Figure 2.3 demonstrates the dependence of the emitted THz electric field on the azimuthal angle, θ, between the crystallographic $(\bar{1}10)$ axis in the [110]-oriented ZnTe crystal and the 800 nm generation pulse polarization. A schematic of this arrangement is given in Fig. 2.4. The detector system is set to detect the component of the THz electric field which is parallel to the generation beam polarization. This azimuthal angle dependence is well described by the theoretically predicted polarization dependence $E_{\parallel} \propto \cos(3\theta)$-

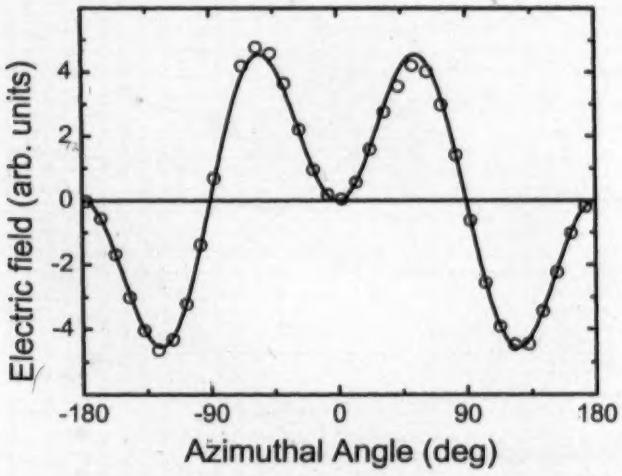

Figure 2.3: Detected THz electric field dependence on the azimuthal angle of the 0.5 mm ZnTe source crystal. The line is a fit to the function $E_{THz} \propto \cos(3\theta)$-$\cos(\theta)$.

$\cos(\theta)$ [42].

2.2 Detection

THz detection in some ways mirrors the two generation schemes listed in the previous section. In the photocurrent detection scheme, which mirrors the photoconductive switch, the bias voltage source is replaced with a current amplifier and fed into a lock-in amplifier for detection. A schematic of this setup is shown in Fig. 2.5(a). A gating pulse excites free carriers in the semiconductor region between the two electrodes. The electric field of the THz pulse, scanned in time with respect to the gating pulse by means of a delay stage, generates a current transient when it is overlapped with the gating pulse. This current transient is picked up by the amplifier and is directly proportional to the THz electric field. By scanning the gating pulse with respect to the THz pulse, the THz electric field can be mapped as a function of time. Typically the semiconductor material is chosen to have a sub-picosecond photoconductive lifetime to increase the bandwidth (decrease the

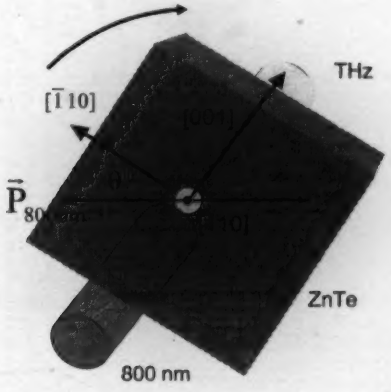

Figure 2.4: Schematic of ZnTe crystal orientation used to obtain the data in Fig. 2.3.

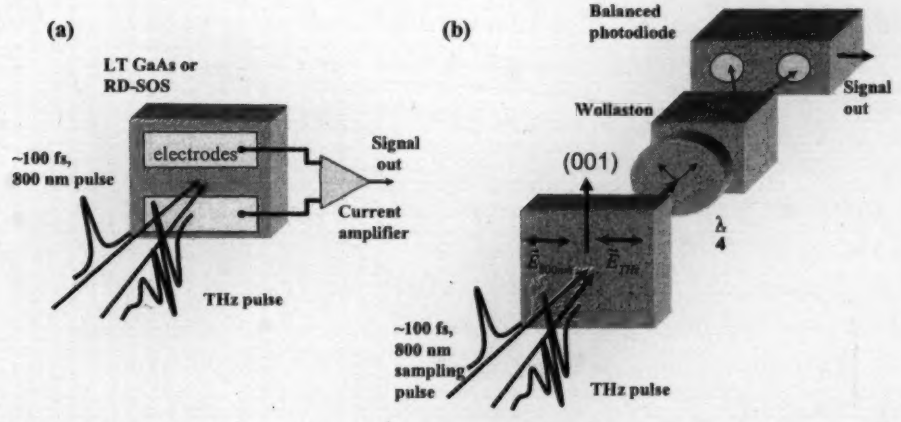

Figure 2.5: Schematic of a) photoconductive and b) free-space electro-optic detection of THz pulses.

response time) of the detector. Two materials that are often used because of their sub-ps recombination time and relatively high carrier mobility are low temperature grown GaAs (LT-GaAs) [43] and radiation damaged silicon on sapphire (RD-SOS) [44, 45]. In LT-GaAs, the low growth temperature promotes the formation of As clusters that act as traps to conduction electrons, reducing the relaxation time to ~ 1 ps [43]. In RD-SOS, the relaxation time is again related to traps generated by the radiation damaging the crystal lattice, interrupting the regular periodicity of the normally epitaxial Si film. The photoconductive relaxation rate is proportional to the extent of damage, reaching a sub-picosecond lifetime at the highest levels of damage, but this is commensurate with a decrease in carrier mobility [44, 46].

The second detection scheme is known as free-space electro-optic detection and uses the linear Pockels effect in an electro-optic (EO) crystal to detect the quasi-DC electric field of the THz pulse with respect to the 100 fs gating pulse. This technique was first demonstrated in 1996, by X.-C. Zhang's group [47], the group of P. Uhd Jepsen and M. Helm [48], and the group of T.F. Heinz [49]. A schematic of this is shown in Fig. 2.5(b). In absence of the THz field, a linearly polarized gating pulse traverses a ZnTe crystal unaffected, passes through a $\lambda/4$ plate and becomes circularly polarized. The orthogonal polarization components are then equally separated by a Wollaston prism and each is sent to one photodiode of a balanced two-photodiode detector. Since the pulse was circularly polarized, each photodiode reads the same voltage that is sent to a lock-in amplifier which subtracts the two and returns a zero reading. When the THz field overlaps the gating pulse in time, the polarization of the gating beam is tilted slightly by an amount proportional to the strength of the electric field (Pockels effect). Now, after the $\lambda/4$ plate, the polarization is elliptically polarized and after separation there is an imbalance in the two voltage signals, registered by the lock-in after subtraction as a signal. This signal is directly proportional to the electric field of the THz pulse, and by scanning the time delay between the gating beam and THz beam the entire THz waveform may be mapped out in time. The lock-in amplifier is locked to the frequency of an optical chopper which modulates the THz source beam at 270 Hz, synchronized to the repetition rate of the amplifier system through a frequency divide-by circuit ($\div 4$) away from any harmonic of the line frequency (60 Hz). By doing so, the amplifier is detecting only the modulation of the 1.08 kHz detection beam which

occurs at the same frequency as the chopping frequency, greatly improving the signal to noise. Typical signal-to-noise (S/N) ratios are 1000:1, which is excellent when compared to other free-space spectroscopic techniques. The two main reasons behind this excellent S/N ratio are the coherent detection that rejects incoherent background radiation, and the short sampling time. In other words, since the gate is "open" for $\sim$ 500 fs, there is only a very short sampling time during which this background radiation can contribute to the signal. ZnTe is the most commonly used EO crystal, although GaSe, GaP, InP, GaAs and DAST have also been used. A detailed study on the crystal orientation dependence of the THz detection in ZnTe is given in Ref. [50]. Because the nonlinear optical rectification process is instantaneous, one would assume that the bandwidth is only limited by the sampling pulse duration. However, the detection bandwidth is fundamentally limited by the phase mismatch between the THz pulse and the 800 nm detection beam due to a difference in refractive index at these two wavelengths [49]. Very thin ZnTe crystals, which minimize the influence of this phase mismatch, have been used to extend the detection bandwidth to 100 THz [51]. Other sources of bandwidth limiting are absorptive phonons at 1.6 and 3.7 THz in ZnTe [39], as well as a TO phonon at 5.31 THz [47].

2.3 Ti:sapphire multipass amplified femtosecond laser system

The time-domain THz spectrometer with pump-probe capability is driven by a multipass amplified Ti:sapphire femtosecond laser system. A schematic of the laser system is given in Fig. 2.6. To begin with, a seed femtosecond pulse is generated by a Kerr-lens modelocked Ti:sapphire oscillator operating at a 90 MHz repetition rate and providing an 800 nm average output power of approximately 375 mW. This translates into 4.7 nJ/pulse output, which then passes through an external prism pair for further compression. The final FWHM pulse width is approximately 35 fs, as determined by a second-order autocorrelator (18 fringes FWHM, $\Delta\tau \approx 2.7$ fs/fringe, $\Delta t = \Delta\tau/1.54$).

This seed pulse is directed into a multipass femtosecond amplifier system op-

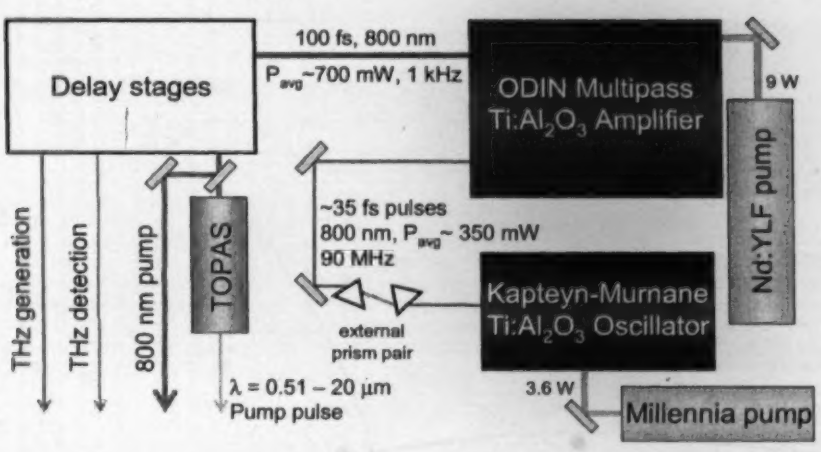

Figure 2.6: Schematic of the femtosecond pulse laser system in the Ultrafast Spectroscopy Laboratory in the Department of Physics at the University of Alberta.

erating at 1.08 kHz. The pulse is first spread in time by passing through a grating pair, so that the amplified pulse does not exceed the damage threshold of the Ti:sapphire gain medium. The pulse then passes 9 times through a Ti:sapphire crystal, co-linearly with a 532 nm, 100 ns pump beam from a frequency-doubled, Q-switched Nd:YLF laser which amplifies the 800 nm pulse energy incrementally in each pass through the crystal. The energy of this pump pulse is ~ 9 mJ/pulse. Finally the pulse is picked off, spatially filtered and sent into another grating pair, where it is compressed in time to a pulse width of $\approx$ 100 fs FWHM. The average energy at this point is typically 600 - 700 mW, or 550 - 650 μJ/pulse. This pulse is then split into a weak and a strong beam by passing through a 80:20 beamsplitter. The strong beam at this point continues on to the THz spectrometer as the pump pulse for optical excitation of the sample. The second portion of the output is further split by a 80:20 beam-splitter into a medium strength THz generation beam, and a weak THz detection beam, respectively. Thus the pulse energies used for THz generation by optical rectification in the ZnTe crystal is $\approx$45 μJ. The detection beam is further attenuated by a half-waveplate, polarizer combination before being gated by the THz pulse in the detection ZnTe crystal, and is approximately

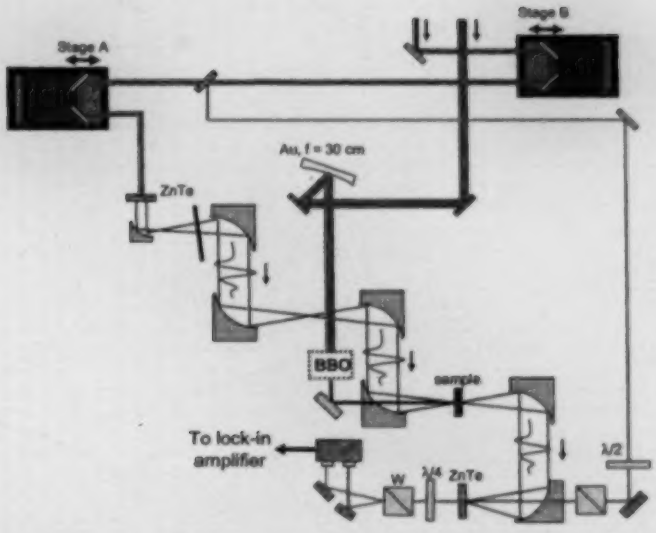

Figure 2.7: Schematic of time-resolved terahertz spectroscopy setup in the Ultrafast Spectroscopy Lab at the Department of Physics, University of Alberta.

10 μW at the balanced photodetector.

2.4 THz spectrometer with pump-probe capability

A schematic of the THz spectrometer is shown in Fig. 2.7, along with a three dimensional schematic and photograph in Fig. 2.8(a) and (b), respectively. The THz setup is in a sealable aluminum enclosure so that the setup can be purged of water vapour by dry nitrogen. The THz generation beam first produces a THz pulse by optical rectification in a 0.5 mm thick [110] oriented ZnTe crystal. The 800 nm generation beam is collimated at this point and the beam spot on the ZnTe crystal is appoximately 5 mm in diameter, producing a THz beam which should be collimated as well. It was noticed, however, that the peak THz signal was sensitive to the distance of the ZnTe crystal from the first collecting off-axis

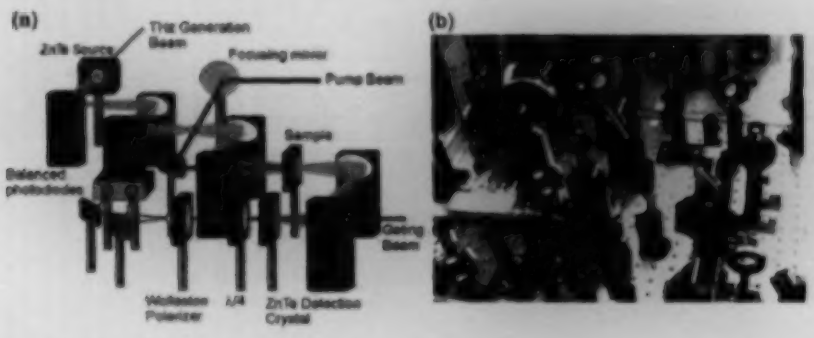

Figure 2.8: (a) Three dimensional schematic and (b) photograph of the time-resolved terahertz spectroscopy setup in the Ultrafast Spectroscopy Lab at the Department of Physics, University of Alberta.

parabolic mirror. This might be an indication that one of the parabolics was misaligned or that the collimation was off. The generated THz pulse propagates colinearly with the transmitted 800 nm generation beam, which is filtered out using a thin sheet of black polyethylene stretched over a ring mount, transmissive to the THz pulse but opaque to the 800 nm pulse. An undoped silicon wafer is more commonly used as a beam block in THz-TDS systems, however due to concerns of residual carriers in the Si excited by the 800 nm leakage through the ZnTe crystal we chose the non-photoconductive polyethylene. We note that polyethylene does have an absorption line at 2.2 THz, however this is much weaker than typical water absorption in the setup. The first collection parabolic is a 1" focusing optic, and the second is a 4", expanding the THz beam to a diameter of approximately 1". The THz pulse then propagates off several f = 3" parabolics to a focus at the sample position. For polarization sensitive experiments it was standard practice to have a free-standing wire-grid polarizer in the THz beam before the sample to ensure the polarization of the pulse was known (parallel to table). The focus of the THz pulse at this point is approximately 1 mm diameter ($1/e^2$) (see Appendix A.3). The sample is typically mounted on a 1.5 mm aperture, which allows most of the THz beam energy through (see Appendix A.3). The optical pump beam, which can be either the 800 nm fundamental, the 400 nm second harmonic generation from

a BBO crystal, or the output from a travelling-wave optical parametric amplifier system (TOPAS), is directed through a small hole in the parabolic mirror just before the focus for excitation of the sample colinearly with the THz pulse. The THz beam is then focused onto another 2.0 mm thick ZnTe crystal for free-space electro-optic detection. A weak, horizontally polarized 800 nm detection beam passes through a Glan Laser polarizer to clean up the polarization before passing through a small hole in the focusing optic before the ZnTe detection crystal, and overlaps the THz beam focus. The ZnTe crystal is oriented with the (001) direction pointing vertical and normal to the table. The detection beam then passes through an achromatic quarter waveplate on a micrometer rotation stage, and then finally through a Wollaston polarizer where its polarization components are split into two beams and sent into the balanced photodetector.

An Oxford sample-in-vapour liquid-He cryostat was often used to cool the sample over a temperature range from 5 K to 300 K. The cryostat was fixed on a platform above the THz focus, which passed though the optical port at the bottom. The sample was mounted on a 1.5 mm aperture, which was in turn mounted on a sample stick visible through the optical port. There were 4 positions to mount a sample in the cryostat for rapid changing of samples at the same temperature, simply by raising or lowering the stick position. The cryostat has both outer and inner windows. Initially, water-free fused silica windows were used on the front entry ports for both inner and outer windows to facilitate pump transmission, yet attenuating the higher frequency components of the pulse, and the two rear exit windows were polypropylene to maximize THz transmission. However, after repeated problems with cold leaks, the rear inner window was replaced with fused silica as well. The fused silica windows attenuate higher frequency components of the THz pulse, and the high index of refraction (1.97) introduces large reflection losses.

Chapter 3

Terahertz time-domain spectroscopy (THz-TDS)

Since it is the electric field of the THz pulse which is mapped in time, rather than the intensity, both amplitude and phase information are coherently detected and can be used to extract the real and imaginary parts of the index of refraction (or equivalently, the complex conductivity or dielectric function, see Appendix A.7) without the use of Kramers-Kronig relations. Another advantage is the brightness of THz pulses surpasses conventional thermal sources, and the coherent gated detection is orders of magnitude better than bolometric detection. The particular attraction of THz-TDS is the energy range which is probed (0.41 - 12.3 meV) which contains spectroscopic signatures for many material systems [52]. In liquid systems, torsional or damped rotational excitations of large molecules are in the THz range [53]. The analysis of either the traditional Fourier transformed [54] or the raw time-domain [55] THz transmission data can be used to identify various gaseous species. Rotational excitations of smaller molecules are often in the 2 meV range, and thus may be probed by a THz pulse [56]. In a simple dielectric, the index of refraction and absorption can be evaluated easily and unambiguously [57]. In condensed matter systems, quasiparticle scattering rates in doped semiconductors are in the THz range, and so THz pulses have been used to characterize both the overall conductivity of the wafer [58, 59] and the spatially resolved variations in carrier density and mobility [60]. Furthermore, superconducting energy gaps [8], and intersubband energy spacings in quantum wells [61] are all in the THz range.

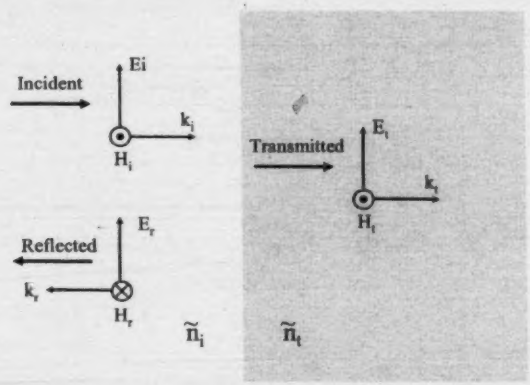

Figure 3.1: Electric and magnetic field vectors after reflection and transmission of an incident electromagnetic wave incident on a semi-infinite (thickness $\gg \lambda$) non-conducting (no free carriers) surface.

This makes the THz region an extremely important yet relatively unexplored part of the spectrum for new and old material systems. In this chapter, we will outline steady state spectroscopy where the studied systems are in equilibrium. The basic equations describing reflection and transmission of an electromagnetic field at an interface (Fresnel equations) are derived. Once this foundation is established, we will walk through an example of THz-TDS on a thick slab dielectric where the complex index of refraction is extracted. It is important to know the index of refraction for select materials in the THz region to correctly extract the complex conductivity of thin films, either deposited or photoexcited layers, which will be the main topic of this thesis in later chapters.

3.1 Fresnel equations

The requirement that the boundary conditions for the tangential components of the electric ($\vec{E}$) and magnetic field ($\vec{H}$), and the normal components of the electric displacement ($\vec{D}$) and magnetic flux ($\vec{B}$), be continuous across the interface of a medium determine the experimental observables such as reflection and trans-

mission of radiation. When the propagation direction of radiation is at normal incidence to the medium, the amplitudes of the incident (E_i, H_i), transmitted (E_t, H_t) and reflected (E_r, H_r) fields are related by

$$E_t = E_i + E_r \tag{3.1}$$

$$H_t = H_i - H_r \tag{3.2}$$

Using the relations $H = B/\mu = B/\mu_0$ (non-magnetic material), $|\vec{E}| = v|\vec{B}|$ and $v = c/n$ where n is the index of refraction, we arrive at

$$E_t n_t = E_i n_i - E_r n_r \tag{3.3}$$

which when combined with Eq. 3.1 gives the amplitude reflection ($\tilde{r}$) and transmission coefficient ($\tilde{t}$) at normal incidence, that in general are complex valued

$$\tilde{r} = \frac{\tilde{n}_i - \tilde{n}_t}{\tilde{n}_i + \tilde{n}_t} \tag{3.4}$$

$$\tilde{t} = \frac{2\tilde{n}_i}{\tilde{n}_i + \tilde{n}_t} \tag{3.5}$$

These equations completely describe the change in amplitude and phase of electromagnetic radiation as it crosses an interface of a bulk material. Once it traverses the interface and is in the material, its vacuum wavevector $\vec{k} = \omega/c\ \hat{z}$ must be replaced by the complex wavevector $\vec{q} = \omega/c\tilde{n}\ \hat{z}$. Passing through a distance d in the material translates into an additional transmission factor of

$$P = e^{i\frac{\omega}{c}\tilde{n}d} = e^{i\frac{\omega}{c}(n+i\kappa)d} = e^{i\frac{\omega}{c}nd}e^{-\frac{\omega}{c}\kappa d} \tag{3.6}$$

which results in both a phase shift term proportional to the real index of refraction (n) and an attenuation term proportional to the extinction coefficient (κ), the imaginary component of the complex index of refraction ($\tilde{n} = n+i\kappa$). Furthermore, the complex index of refraction is generally frequency dependent.

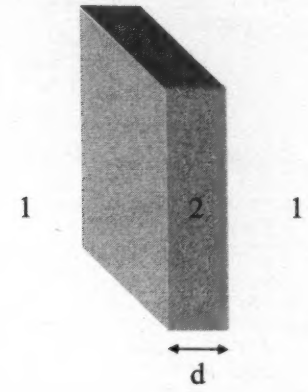

Figure 3.2: Schematic showing the labeling of regions in thick slab geometry used for extraction of the complex index of refraction of a material using THz-TDS.

3.2 Substrate characterization

Equations 3.5 and 3.6 are all that are required to extract the real and imaginary parts of the index of refraction for a given experimental geometry. The simplest example of a sample geometry is a thick slab, much larger than the THz wavelength in the medium (λ/N) so that etalon effects can be ignored by time-windowing out the reflections of the THz pulse. The geometry for this sample is shown in Fig. 3.2, with air (1) and sample (2) regions indicated. The subsequent Fourier transform of these scans provides the complex transmission function, $\tilde{T}(\omega)$, which can be related to $\tilde{n}$ by

$$\tilde{T} = \frac{\tilde{E}_{sample}(\omega)}{\tilde{E}_{ref}(\omega)} = \frac{t_{12}t_{21}P_2}{P_1} = \frac{4\tilde{n}}{(1+\tilde{n})^2}e^{i(\tilde{n}-1)\frac{\omega}{c}d} \tag{3.7}$$

Eq. 3.7 can be split into magnitude ($|T(\omega)|$) and phase ($\Phi(\omega)$) components to yield a coupled set of nonlinear equations

$$|T(\omega)| = \frac{4\sqrt{n^2+k^2}}{(n+1)^2+k^2}e^{-k\frac{\omega d}{c}} \tag{3.8}$$

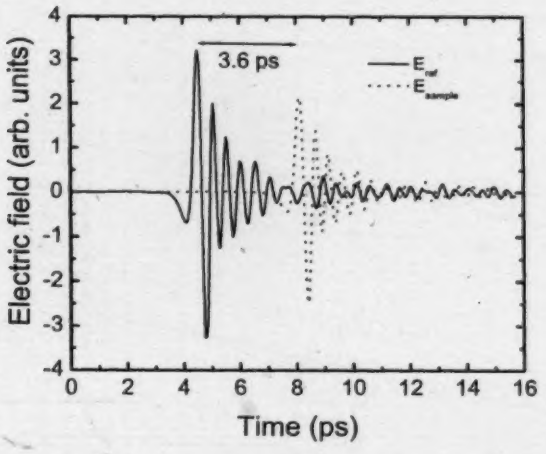

Figure 3.3: Time domain data for a THz pulse traversing air (E_{ref}) and a 0.5 mm thick piece of sapphire (E_{sample}). Note that the large amount of post-pulse ringing is likely due to the amplifier compressor setting not being optimized.

$$\Phi(\omega) = -(n-1)\frac{\omega d}{c} + atan\left(\frac{k(n^2+k^2-1)}{n(n+1)^2+k^2(n+2)}\right) \tag{3.9}$$

that must be solved numerically. If the material is non-absorbing, Eq. 3.8 and 3.9 can be decoupled with

$$n = -\Phi\frac{c}{\omega d} + 1 \tag{3.10}$$

$$|T(\omega)| = \frac{4\sqrt{n^2+k^2}}{(n+1)^2+k^2} \tag{3.11}$$

An example of this type of spectroscopy follows, where a 0.5 mm thick piece of intrinsic sapphire is used as a sample. Fig. 3.3 shows the THz waveforms with (sample) and without (reference) the sapphire in the sample holder at normal incidence. Even without FFT analysis, an estimate can be obtained for the index of refraction, n, from the time shift when the sample is in place. The time delay introduced by a medium is given by $\Delta t = (n-1)d/c$. For the 3.6 ps delay in

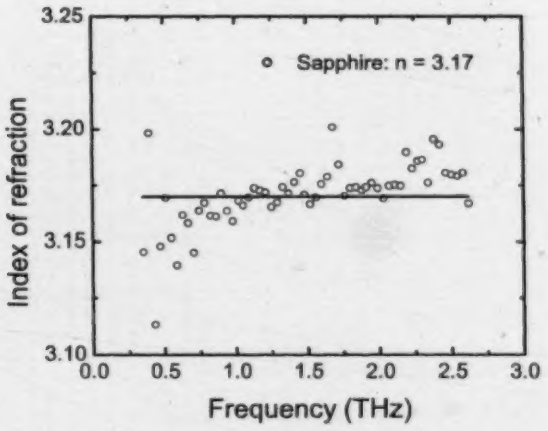

Figure 3.4: Extracted index of refraction for a 0.5 mm thick sapphire substrate.

a 0.5 mm thick sample gives $n = 3.16$. After FFT of these waveforms, the ratio of the sample and reference amplitudes $|E_{sample}/E_{ref}|$ gives $|T|$ and the difference of the sample and reference phases $\phi_{sample} - \phi_{ref}$ gives Φ, describe the complex transmission function, $\tilde{T}(\omega) = |T|e^{i\Phi}$. Using $|T|$ and Φ, Eq. 3.7 can be inverted numerically by a procedure outlined in Appendix A.6 to obtain the real and imaginary parts of the index of refraction, plotted in Fig. 3.4. One can see there is excellent agreement with the estimate using the time shift above and the extracted index, which is relatively constant at 3.17. The extinction coefficient was negligible and so is not shown.

Chapter 4

Time-resolved terahertz spectroscopy (TRTS)

While terahertz time-domain spectroscopy (THz-TDS) involves recording the electric field of the THz pulse on a femtosecond time scale, it is not a time-resolved technique. The dielectric constants obtained from the sample are static. Very early on in the mid-1980s however [62], it was realized that since the THz radiation is pulsed with durations on the order of 0.5 ps, it is possible to use them in a typical pump-probe configuration. Since the pioneering work by Nuss, Auston, and Capasso, terahertz pulse spectroscopy has become a widely used and powerful research tool with which to probe transient conductivity dynamics in materials on a picosecond time scale [63]. The low energy of the THz pulse (1 THz = 4.1 meV = 48 K) allows one to spectroscopically probe energy scales well below room temperature because of the coherent detection. THz pulses are thus ideally suited to probe nonequilibrium picosecond dynamics of systems with characteristic energy scales in the 0.4 - 12 meV range. The terminology used by the THz community to describe this technique is known as time-resolved terahertz spectroscopy (TRTS). Examples of bulk material systems that have been investigated by TRTS are conventional [64] and high-Tc [65, 66] superconductors, inorganic [11, 67, 45, 46, 9] and organic semiconductors [68, 69], amorphous and radiation damaged inorganic semiconductors [45, 46], insulators [70], and materials showing colossal magnetoresistance [71]. TRTS has been used to investigate solvation and transport dynamics in liquids as well [72]. Several groups have begun investigating the THz response

of photoexcited nanostructured materials, such as CdSe [73], TiO_2 [74], InP [75], InAs [76, 77], and ErAs [78] quantum dots, carbon nanotubes [79, 80, 36] and Si nanocrystal composite films [36]. In this thesis, we make three new additions to this list, namely self-organized InGaAs/GaAs quantum dot arrays [81], laterally organized InGaAs/GaAs quantum wires [82] and Si nanocrystal films derived from thermal annealing of Si-rich oxides [83]. We also use TRTS to explore the nature of conduction in a bulk system, dilute nitride and bismide alloys of GaAs [84].

4.1 Methodology

In a TRTS experiment, a femtosecond pump pulse is used to photoexcite the sample into a nonequilibrium state. A THz pulse then probes the pump-induced photoconductivity via transmission through the sample. The pump-probe time delay can be scanned so that the rise and fall of the induced photoconductivity can be mapped in time with a resolution limited primarily by the width of the THz pulse, or approximately 0.5 ps. There are two methods of operation in a TRTS experiment, a one-dimensional scan or a two-dimensional scan, so named because either one or two delay stages must be scanned. While the focus of this chapter is on TRTS, the outlined formulas used to extract the optical constants of thin photoexcited films can equally be used for THz-TDS studies of static conducting films (For example, Au films [85]).

4.1.1 One-dimensional scans

The first technique is simply to ignore the phase information carried by the electric field and only monitor the field amplitude attenuation as it traverses a photoconductive layer. One first adjusts the THz source time delay (Stage A, Fig. 2.7) such that the sampling beam and the peak of the THz pulse arrive at the detection ZnTe crystal at the same time. By doing so, the lock-ins are monitoring the peak electric field of the THz pulse, where all frequency components of the pulse are in phase with each other. A modulation is introduced in the pump beam by an optical chopper at 540 Hz synced to the amplifier repetition rate after a $\div 2$ circuit. This is twice the frequency of the chopping frequency of the THz source

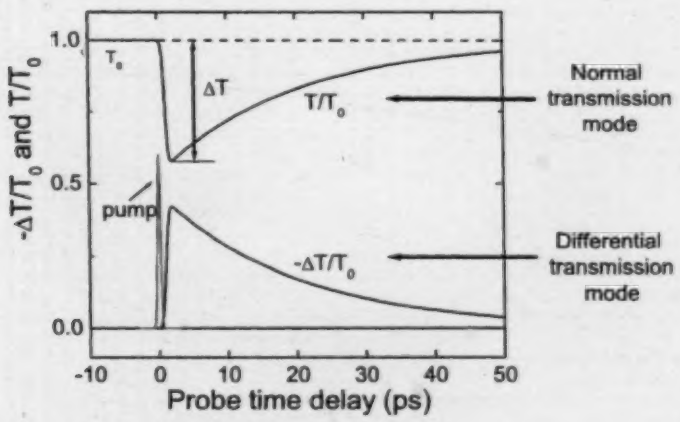

Figure 4.1: Schematic of time-resolved terahertz spectroscopy one-dimensional scan modes.

beam. The lock-in then monitors the modulation of the THz peak electric field at the frequency of the pump chopper, effectively reading $\Delta T = T_{pump} - T_0$. The advantage of this detection scheme is that the modulation is detected with a zero background, and the sensitivity of the lock-ins can be set higher. The THz source and detection beams are then scanned in time simultaneously by moving a shared retro-reflector delay stage (Stage B, Fig. 2.7) so that they remain coincident with each other at the sample, but are scanned in time with respect to the pump pulse. When the pump pulse overlaps the sample in time with the THz probe pulse, the induced photoconductivity in the sample reduces the transmission of the THz pulse due to free-carrier absorption. A schematic of the resultant scan is shown in Fig. 4.1, with both the normalized transmission (starting at 1 and decreasing) and the negative differential transmission, $-\Delta T/T_0$, shown. T_0 is the THz transmission at negative pump-probe delay times. In practice, two pump-probe delay scans are needed: the differential scan where pump beam is chopped obtaining $-\Delta T$, and the normal transmission mode where the THz source beam is chopped and the actual change in transmission is monitored over the peak to calibrate $-\Delta T$.

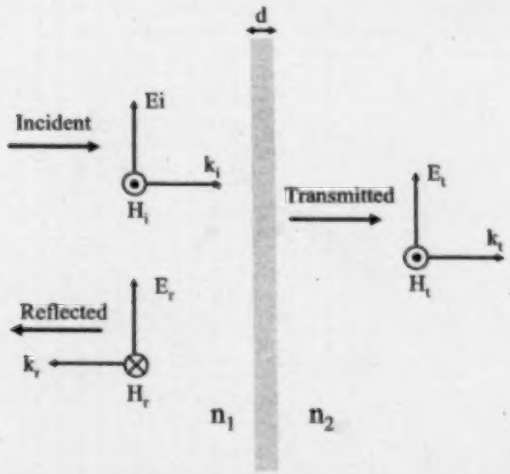

Figure 4.2: Electric and magnetic field vectors after reflection and transmission of an incident electromagnetic wave incident on a thin conducting film ($d \ll \lambda$).

Next we derive an expression for the complex transmission function through a thin conducting film in between two media with real index of refraction. In a TRTS experiment, the first media would be air and the second would be the semi-insulating dielectric substrate. The continuity equations describing the electric and magnetic fields at the boundary are given by

$$\hat{n} \times (\vec{H}_1 - \vec{H}_2) = \int_0^\infty \vec{J} dz = \vec{J} d \tag{4.1}$$

$$\hat{n} \times (\vec{E}_1 - \vec{E}_2) = 0 \tag{4.2}$$

At normal incidence this simplifies to

$$H_i - H_r - H_t = Jd \tag{4.3}$$

$$E_i + E_r - E_t = 0 \tag{4.4}$$

which is identical to the boundary equations used to derive the Fresnel transmission

and reflection coefficients at the boundary of a dielectric. Using the definition of admittance Y = H/E, the ratio of the magnetic field H to the electric field E, and combining Eqns. 4.3 and 4.4 we reach an expression for the transmitted electric field

$$E_t = \frac{1}{Y_1 + Y_2}(2Y_1 E_i - Jd) \tag{4.5}$$

where $Y_1 = \frac{H_i + H_r}{E_i + E_r}$ and $Y_2 = \frac{H_t}{E_t}$. Solving for the transmission coefficient, $t = E_t/E_i$ and substituting $J = \tilde{\sigma} E_t$ where $\tilde{\sigma}$ is the conductivity we get

$$\tilde{t} = \frac{2Y_1}{Y_1 + Y_2 + \tilde{\sigma} d} \tag{4.6}$$

Making the substitution $Y_a = \frac{N_a}{Z_0}$ where N_a is the index of refraction of the medium and Z_0 is the impedance of free space, 377 Ω, we reach our final expression for the transmission through a thin conducting film, known as the Tinkham equation [86]

$$\tilde{t}_{film} = \frac{2}{N + 1 + Z_0 d\tilde{\sigma}(\omega)} \tag{4.7}$$

where we have assumed the index of refraction of air is 1 and the substrate index of refraction is primarily real and equal to N. This equation is valid provided d $\ll \lambda/n$, the wavelength in the film, or $\frac{n\omega d}{c} \ll 1$, so that any internal reflections within the photoexcited layer can be averaged over and neglected. This condition is investigated for four examples shown in Fig. 4.3: a 10 nm and 30 nm Au film, GaAs photoexcited with 800 nm light and GaAs photoexcited with 400 nm light. One can see that the high conductivity of bulk Au makes even a 30 nm film a questionable application of the thin film equation, shown in Fig. 4.3(c), while a 10 nm film is within the valid region. Meanwhile, GaAs when photoexcited with fairly high fluence to a carrier density of 1.0×10^{18} cm^{-3} and a penetration depth of 1 micron, it is still in the region of validity. Finally, for 400 nm excited GaAs, the penetration depth is sufficiently low such that for any reasonable excitation the validity condition is satisfied.

Using the transmission coefficient for the unexcited dielectric slab (substrate), $t_{sub} = \frac{2}{N+1}$, we obtain the transmission function for a photoexcited layer with

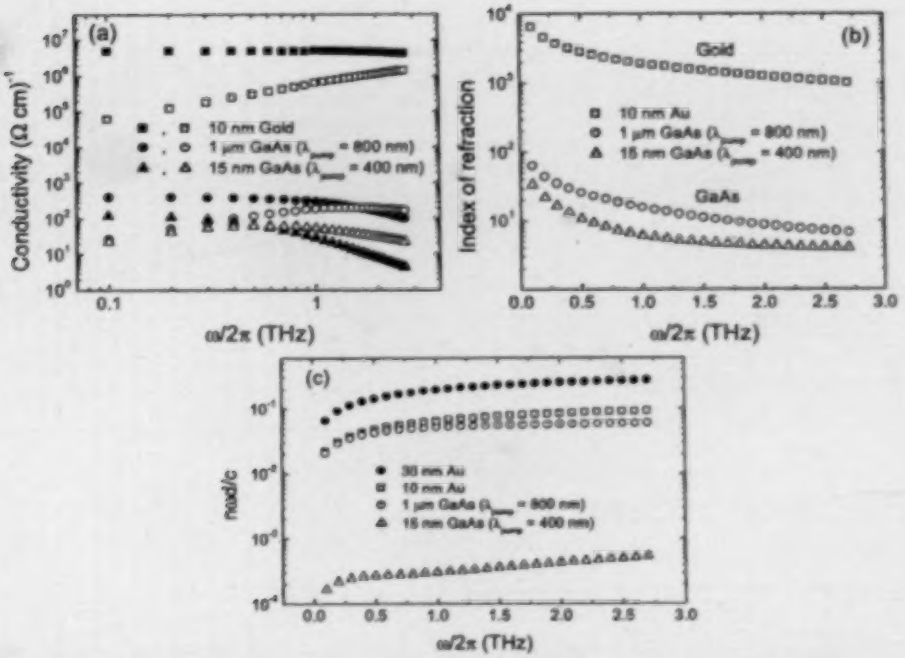

Figure 4.3: Test of the validity of the thin film equation for four films: 10 nm and 30 nm thick gold films ($\omega_p = (2\pi)2.175 \times 10^{15}$ Hz, $\tau = 20$ fs), GaAs photoexcited with 800 nm pump ($\delta_{800nm} = 1\mu$m, n = 1×10^{18} cm^{-3}, $\tau = 100$ fs), and GaAs photoexcited with 400 nm pump ($\delta_{400nm} = 15$ nm, n = 1×10^{17} cm^{-3}, $\tau = 300$ fs). Shown is the (a) film conductivity (closed symbols - σ_1, open symbols - σ_2), (b) film index of refraction and (c) the ratio of film thickness to THz wavelength in the film.

respect to the background unexcited substrate

$$\tilde{T}(\omega) = \frac{t_{film}}{t_{subs}} = \frac{\tilde{E}_{pump}(\omega)}{\tilde{E}_{ref}(\omega)} = \frac{N+1}{N+1+Z_0 d\tilde{\sigma}(\omega)} \tag{4.8}$$

For deep penetrating excitation, the distance traversed through the unexcited substrate is sufficiently different from the excited substrate so that an additional phase factor must be added. In this case, the thin film equation is written as

$$\tilde{T}(\omega) = \frac{t_{film}}{t_{subs}} = \frac{\tilde{E}_{pump}(\omega)}{\tilde{E}_{ref}(\omega)} = \frac{N+1}{N+1+Z_0 d\tilde{\sigma}(\omega)} e^{-iNd\frac{\omega}{c}} \tag{4.9}$$

One has to be careful when applying the thin film equation to higher index, deeper penetrating pump situations, but for all situations encountered in this thesis, the penetration depth is small enough such that Eq. 4.8 suffices. The criterion for Eq. 4.8 to be appropriate instead of Eq. 4.9 is $\frac{Nwd}{c} \ll \Phi$, the phase change of the THz pulse from the terms given in Eq. 4.8 alone. This equation will be used later in its entirety to extract the frequency dependent complex conductivity, however the analysis can be simplified enormously if we now make the assumption that the conductivity response is purely real, i.e. $\tilde{\sigma}(\omega) \approx \sigma_{dc}$ as it is for a Drude material in the Hagens-Rubens regime ($\omega\tau \ll 1$). The negative differential transmission can then be related to the pump-induced change in conductivity $\Delta\sigma$

$$-\Delta T(t)/T_0 = \frac{T_0 - T_{pump}}{T_0} = 1 - \frac{N+1}{N+1+Z_0 d\Delta\sigma(t)} \tag{4.10}$$

and can be solved for $\Delta\sigma$ as

$$\Delta\sigma(t) = \frac{N+1}{Z_0 d}\left(-\frac{\Delta T}{T_0}\right)\left[\frac{1}{1+\frac{\Delta T(t)}{T_0}}\right] \tag{4.11}$$

For small $|-\Delta T/T_0|$ ($< 20\%$), $\Delta\sigma(t) \approx \frac{N+1}{Z_0 d}|\frac{-\Delta T}{T_0}|$ and the differential THz transmission is directly proportional to the conductivity of the film. The validity of this approach depends on the response of the material being purely resistive, such that the amplitude of the field is uniformly attenuated for all frequency components in the pulse. If there is a significant change in phase across the bandwidth of the pulse, there will be an associated temporal shift in the time domain of the THz

pulse. Since in a one dimensional scan we monitor only the peak of the THz waveform, the time shift causes what appears to be a differential transmission signal even though there may be no attenuation of the peak. Effectively the peak moves in time, so we measure a dip in the transmission due to sliding off the peak. The direction of the time shift is important and reveals whether the phase change is related to a Drude or Lorentz (below resonance) response, which will be discussed in a later chapter.

Provided the phase shift is small and the response is well described as Drude, we can further analyze the differential transmission to obtain valuable information on the carrier dynamics, n(t), in the system as well as extract important transport coefficients, such as the carrier mobility μ. In general, however, the mobility can be time-dependent in which case $\sigma(t) = n(t)e\mu(t)$ and a more complex analysis is required to separate the carrier density from the mobility response (see next section). If the mobility is time-independent, then the decay of the conductivity is entirely due to the decay of free charge carriers. Furthermore, by measuring the peak $-\Delta T/T_0$ (assumed small for simplicity), the carrier mobility can be obtained using

$$\mu = \frac{N+1}{Z_0 e d n_{max}} \left(-\frac{\Delta T}{T_0} \right) \tag{4.12}$$

if the maximum injected carrier density, n_{max}, is known. This can be estimated from knowledge of the pump fluence, F, using

$$n_{max} = \frac{\eta F \lambda (1-R)}{hc\delta} \tag{4.13}$$

where η is the quantum efficiency, R is the reflection coefficient for the pump pulse, λ is the pump wavelength and δ is the pump penetration depth. In the case of inorganic semiconductors such as GaAs or Si, $\eta \cong 1$ is an excellent assumption and the mobility can be obtained directly [45]. In materials such as organic molecular single crystals or thin films where the quantum efficiency is unknown, the best one can do is to report an upper limit on the mobility by quoting the product $\eta\mu$ [68, 87, 69, 88].

In the situation where the response is purely resistive, one can ask what is the minimum detectable conductivity of a film using TRTS? Because this is de-

pendent on the thickness of the film, d, the quantity of interest is the minimum detectable sheet conductivity, $\sigma_\square = \sigma d$. Given a minimum detectable change in THz transmission of 1 part in 10^5 and using equation 4.11 gives

$$\sigma_\square = \frac{N+1}{Z_0} 10^{-5} \tag{4.14}$$

With N$\approx$ 3, this gives $\sigma_\square \approx 10^{-7}\ \Omega^{-1}$. Thus for a 15 nm thick film, for example, the minimum detectable conductivity is 0.07 $[\Omega\ \text{cm}]^{-1}$. For a GaAs room temperature electron mobility of 8000 cm^2/Vs, this corresponds to a minimum carrier density $n_{min} \approx 5.5 \times 10^{13}\ \text{cm}^{-3}$.

4.1.2 Two-dimensional scans

The coherent detection of the electric field records both the amplitude and phase of the THz pulse electric field, which can be used to extract the frequency-dependent complex dielectric function, or equivalently the complex conductivity, on picosecond time scales after optical excitation without the use of Kramers-Kronig relations. The methodology of so-called two-dimensional scans is similar to the THz-TDS technique described in Chapter 3, with the addition of a pump pulse that excites the sample into a non-equilibrium state. The lock-in is synchronized to detect changes in the detection beam at the frequency of the optical chopper frequency modulating the THz source beam. This reads a voltage proportional to the electric field of the THz pulse. The time delay between the THz source pulse and the detection pulse is scanned in time by moving delay Stage A in Fig. 2.7, mapping the THz pulse out in time with a typical sampling interval Δ of 50 fs. The resolution of the THz scan does not matter so long as the highest frequency of the bandwidth-limited THz pulse, typically 3 THz, is below the Nyquist frequency defined as f_c=$1/2\Delta$. For Δ = 50 fs, f_c = 10 THz which is more than sufficient. The duration of the scan sets the frequency resolution, given as $\Delta f = 1/N\Delta t$ where N is the number of sampling points. In practice, reflections in the time domain inside the sample, ZnTe source or detection crystal limit the duration of the scan and thus the frequency resolution. Including the reflections in the scan leads to Fabry-Perot etalon fringes in the frequency domain that interfere with data analysis. Typically this limits the scan to around 10 ps, giving a frequency resolution

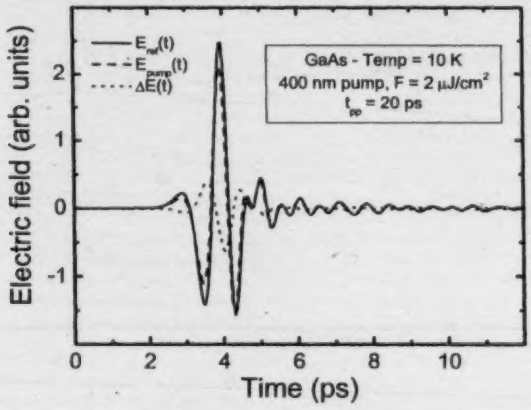

Figure 4.4: Time domain data for transient spectroscopy on GaAs photoexcited with a 400 nm, F = $2\mu J/cm^2$, 20 ps after excitation at T = 10 K.

of 0.1 THz.

An important detail is that the THz source beam that is scanned to map the THz pulse in time. Previously in this group, the detection beam was scanned while the THz source beam was fixed in time. As was first pointed out by the Schmuttenmaer group [43], this results in a complication when a pump pulse is introduced and the conductivity of the sample is changing on a time scale comparable to the THz pulse. Scanning the detection beam not only changes the time delay of the THz source beam, but also the pump beam, so that each point in the THz pulse is experiencing a slightly different pump-probe time delay. If the conductivity is decaying on a time scale comparable to the THz pulse, early times in the THz waveform could be experiencing a higher conductivity than later times. By scanning the THz source beam, the delay between the sampling beam and the pump beam are held fixed. This means that each point in the detected THz waveform are experiencing the same pump-probe time delay, and therefore no artifacts are introduced by the temporal overlap of the THz pulse with the pump pulse at the sample.

Two scans are needed to extract the transient conductivity of a material, a reference scan taken at negative pump-probe delay times where the THz pulse

arrives before the pump pulse, $E_{ref}(t)$, and a pumped scan where the pump-probe delay time is set to a specific positive delay time, $E_{pump}(t)$. The ratio of the Fourier transforms of these two pulses provides the complex transmission function $\tilde{T}(\omega)$ which can be analytically related to the complex conductivity by Eq. 4.8. In practice, just like the one dimensional scans, the change in the reference pulse $-\Delta E(t) = E_{pump}(t) - E_{ref}(t)$ is measured and then calibrated by looking at the one dimensional T/T_0 scan (see Appendix B.5). An example of the time domain data is provided in Fig. 4.4 using a 0.5 mm thick GaAs sample at a temperature of 10 K. With a substrate index of refraction N = 3.6 (See Fig. 6.5), there is a reflection (not shown in Fig. 4.4) corresponding to the THz pulse reflecting off the back surface, off the front surface and then back again. The time delay between the original transmitted pulse and the reflected pulse is $\Delta t = \frac{2LN}{c} = 12$ ps, which sets the limit for the scan.

Fourier transforms of the scans given in Fig. 4.4 provide the complex transmission function, containing all the information required to extract the complex conductivity of the sample. The amplitude, $|T(\omega)| = \frac{|E_{pump}(\omega)|}{|E_{ref}(\omega)|}$ and phase $\Phi(\omega) = \theta_{pump} - \theta_{ref}$ are plotted in Fig. 4.5(a) and (b), respectively. A simple manipulation of Eq. 4.8 using the polar form gives the following equations for the real and imaginary parts of the conductivity in terms of $|T(\omega)|$ and $\Phi(\omega)$

$$\sigma_1(\omega) = \frac{N+1}{Z_0 d}\left[\frac{1}{|T(\omega|}cos(\Phi) - 1\right] \tag{4.15}$$

$$\sigma_2(\omega) = -\frac{N+1}{Z_0 d}\left[\frac{1}{|T(\omega|}sin(\Phi)\right] \tag{4.16}$$

and the extracted complex conductivity of the photoexcited GaAs layer is given in Fig. 4.5(c), assuming the layer thickness, d, is well approximated by the pump penetration depth $\delta_{400nm} = 15$ nm [89]. Typically in a TRTS setup, the error in the phase $\Phi(\omega)$ is on the order of 0.02 rad at 1 THz, and the error in the absolute transmission $|T(\omega)|$ is about 3%, due to statistical fluctuations [90], however this can be reduced with multiple averaging.

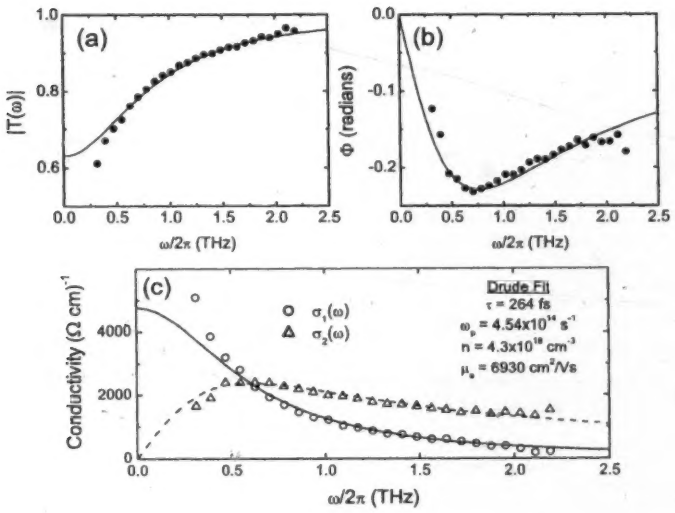

Figure 4.5: (a) Amplitude and (b) phase of the complex transmission function derived from Fourier transforms of the $E_{pump}(t)$ and $E_{ref}(t)$ waveforms in Fig. 4.4. (c) The extracted complex conductivity. The solid lines are fits to the Drude model, using parameters given in (c).

Part II

Theoretical models for conductivity in materials

Chapter 5

Models of ac conductivity

The frequency-dependent complex conductivity completely describes the linear response of both free and bound charge carriers to an applied electric field. In this chapter, we outline the theoretical models of optical conductivity in band semiconductors used in the works presented in this thesis. Many of these models have been formulated over a hundred years before this thesis was written, before the advent of quantum mechanics, and use classical ideas such as the kinetic theory of gases and the motion of harmonic oscillators to describe the optical properties of real material systems. It is remarkable that despite this simplistic view of a very complicated problem, they nevertheless describe the state of affairs quite well and are the basis of our current understanding of electrodynamics in solids.

5.1 Free carrier response - Drude model

Perhaps the simplest and most commonly used conductivity model is the Drude model. Here, charge carriers are considered free to respond to an electric field, with a collisional dampening rate $1/\tau$. When a field is turned on, carriers equilibrate to a velocity distribution with a mean value, $\vec{v}$. When the field is switched off, the carrier velocity distribution relaxes exponentially with time constant τ (scattering time), until the average carrier velocity, $\vec{v} = 0$. In an applied electric field, the carrier motion is described by the rate equation

$$m\frac{d\vec{v}(t)}{dt} = -m\frac{\vec{v}}{\tau} - e\vec{E}(t) \tag{5.1}$$

with a current density given as $\vec{J} = -ne\vec{v}$, where n is the density of carriers, -e is the electronic charge and m is the carrier mass. In a steady-state (dc) field, $d\vec{v}/dt = 0$, giving

$$\sigma_{dc} = \frac{\vec{J}}{\vec{E}} = \frac{ne^2\tau}{m} = \omega_p^2\epsilon_0\tau \tag{5.2}$$

where the plasma frequency is defined as $\omega_p^2 = ne^2/\epsilon_0 m$. This also defines another important dc transport parameter, namely the mobility, μ, which is ratio of the average drift velocity of the carrier distribution to the field given by

$$\mu \equiv \frac{\vec{v}}{\vec{E}} = \frac{e\tau}{m} \tag{5.3}$$

so that $\sigma_{dc} = ne\mu$.

In an applied ac field of frequency ω, $\vec{E}(t) = Re\{\vec{E}(\omega)e^{-i\omega t}\}$, the desired solution to Eq. 5.1 is of the form $\vec{v}(t) = Re\{\vec{v}(\omega)e^{-i\omega t}\}$. Substituting $\vec{v}(t)$ into Eq. 5.1 gives

$$(-i\omega)\vec{v}(\omega) = -\frac{\vec{v}(\omega)}{\tau} - e\vec{E}(\omega) \tag{5.4}$$

After grouping terms and using $\vec{J} = -ne\vec{v}$ and $\tilde{\sigma}(\omega) = \vec{J}/\vec{E}$, we arrive at the final form

$$\tilde{\sigma}(\omega) = \sigma_1(\omega) + i\sigma_2(\omega) = \frac{\sigma_{dc}}{1 - i\omega\tau} \tag{5.5}$$

We can see the shape of the conductivity spectra depends entirely on the product $\omega\tau$. Separating real and imaginary parts

$$\sigma_1(\omega) = \sigma_{dc}\frac{1}{1 + (\omega\tau)^2} \tag{5.6}$$

$$\sigma_2(\omega) = \sigma_{dc}\frac{\omega\tau}{1 + (\omega\tau)^2} \tag{5.7}$$

Figure 5.1 shows these two equations plotted against the product of the probing frequency and the scattering time, $\omega\tau$. The inset shows the case of $\omega\tau \ll 1$, where σ_1 is roughly frequency independent and is well approximated by σ_{dc}. Typically in

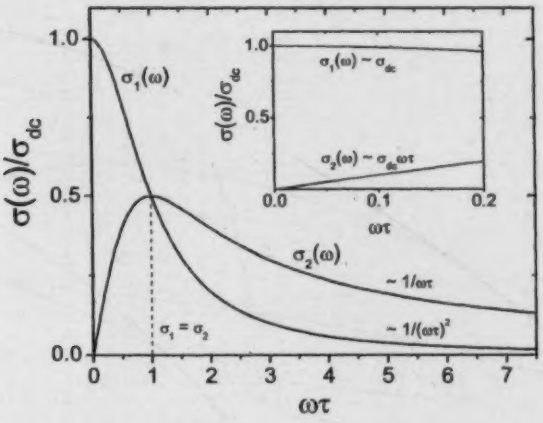

Figure 5.1: Complex conductivity according to the Drude model. Inset is a plot of the Drude conductivity in the $\omega\tau \ll 1$ limit.

semiconductors, τ is on the order of 10 - 100 fs, so that the characteristic frequency range $\omega\tau \sim 1$ in the THz region of the spectra. Preferably, one would like to be in this regime when measuring the conductivity because of the distinct features such as $\sigma_2 = \sigma_1$ at $\omega = 1/\tau$, which allows for accurate determination of both τ and ω_p.

Fig. 5.2 shows the expected conductivity features in a THz-TDS experiment for various materials assuming a Drude conductivity and for room temperature scattering times given in Table 5.1. The THz pulse bandwidth is assumed to be 0.2 - 3 THz. For doped semiconductors such as Si and GaAs, the conductivity features are within this THz region and thus the transport parameters can be very accurately determined. Metals such as Au, Cu and especially Pb have a rather small τ, typically less than 30 fs (See Table 5.1, adapted from Ref. [1]), and so the conductivity features in the THz bandwidth lie in the region where $\sigma_1 \sim \sigma_{dc}$ and $\sigma_2 \simeq 0$. This makes accurate determination of the conductivity parameters difficult without very precise measurements. In a TRTS experiment, the conductivity of the photoexcited film is derived from the complex transmission function, $\tilde{T}(\omega)$. The THz electric field transmitted through the conducting film is given by

Sample	τ (fs)
Pb	1.4
Polypyrrole	12.6
$Ba_{0.8}K_{0.4}BiO_3$ (Tc = 31 K)	15
Cu	27
Au	30
Al_2O_3	95
n-GaAs (n = 7.8×10^{15} cm^{-3}) ($\mu \sim 4300 cm^2/Vs$)	165
Graphite	200
n-Si (n = 4×10^{14} cm^{-3}) ($\mu \sim 2000 cm^2/Vs$)	295

Table 5.1: Drude scattering time for various materials (adapted from [1]).

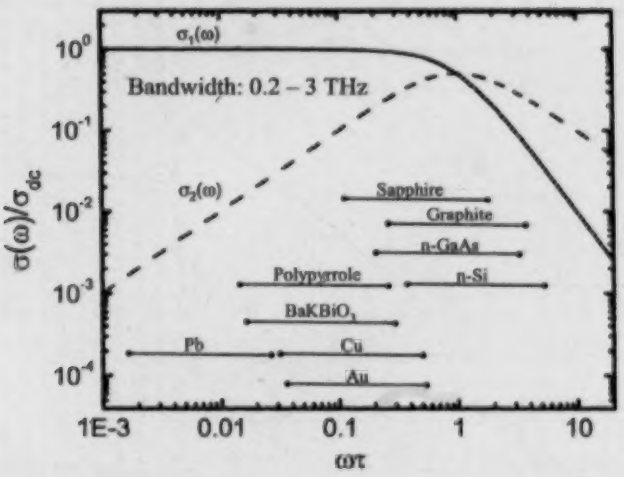

Figure 5.2: Spectral features expected for various materials based on the Drude model and literature scattering times given in Table 5.1, probed in the TRTS bandwidth of 0.2 - 3 THz.

$$E_{pump}(t) = Re\left[\int_0^\infty \tilde{T}(\omega)\tilde{E}_{ref}(\omega)e^{i\omega t}d\omega\right] \tag{5.8}$$

Through this equation it is possible to model the changes in the THz pulse transmission in the time domain, given a form for the film conductivity, the thickness of the excited film and the index of refraction of the substrate. Fig. 5.3 demonstrates the conductivity of a Drude material, in the (a) $\omega\tau \ll 1$ and (c) $\omega\tau \sim 1$ limits. The corresponding changes in THz transmission are given in Fig. 5.3(b) and (d), respectively. In the $\omega\tau \ll 1$ limit, the response is solely absorptive with no phase change in E_{pump} with respect to E_{ref}. It is in this regime that the one dimensional scans outlined in the previous chapter wholly describe the conductivity response by simply monitoring the peak THz transmission, because the conductivity is essentially purely real.

Fig. 5.3(d) shows the changes in THz transmission through a film with conductivity given in (c), in the $\omega\tau \sim 1$ regime with $\tau = 250$ fs. In addition to an absorptive response there is a sizable phase change, with the peak of the trans-

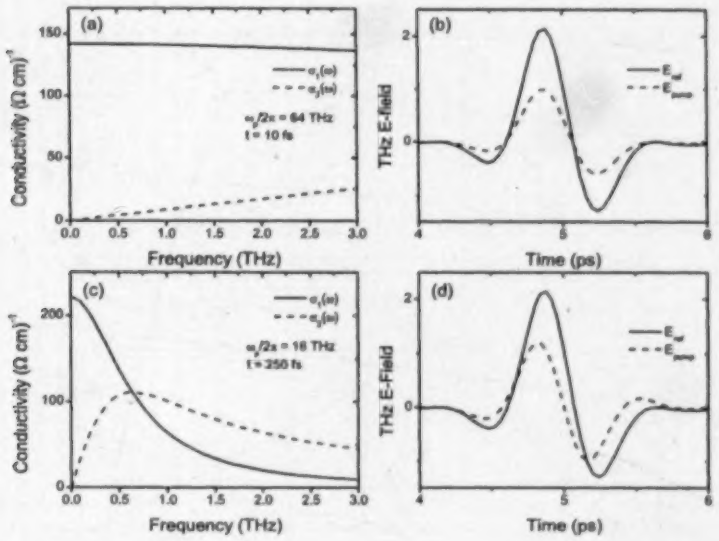

Figure 5.3: Conductivity of a thin film on a GaAs insulating substrate in (a) the $\omega\tau \ll 1$ limit and (c) the $\omega\tau \sim 1$ regime. The calculated change in THz pulse transmission is given in (b) and (d) for the film conductivity in (a) and (c), respectively.

mitted pulse arriving 40 fs *before* the reference pulse. This is not related to any super-luminal propagation, but rather to the large frequency-dependent phase shift at the conductive surface layer [67].

5.2 Localized carrier response - Lorentz model

The polarization response of bound charges to an applied electric field is well described by the Lorentz model. A single damped harmonic oscillator with force constant k and driven by an electric field of the form $\vec{E}(t) = E(\omega)e^{-i\omega t}$ is described by the equation of motion

$$m\frac{d^2\vec{x}(t)}{dt^2} + \frac{m}{\tau}\frac{d\vec{x}(t)}{dt} + k\vec{x}(t) = -eE(t) \tag{5.9}$$

We seek a solution of the form $\vec{x}(t) = \vec{x}(\omega)e^{-i\omega t}$. Substituting into Eq. 5.9 gives

$$\vec{x}(\omega) = -\frac{e}{m}\frac{1}{(\omega_0^2 - \omega^2) - i\omega/\tau}\vec{E}(\omega) \tag{5.10}$$

with the definition $\omega_0^2 \equiv k/m$, the resonant frequency of the oscillator. The dipole moment per unit volume is given by $\vec{P} = -Ne\vec{x}$ and is related to the electric susceptibility by $\vec{P} = \epsilon_0\chi\vec{E}$. The dielectric function $\epsilon(\omega)$ is in turn related to χ by $\epsilon = \epsilon_0(1+\chi)$ giving

$$\frac{\tilde{\epsilon}(\omega)}{\epsilon_0} = 1 + \frac{\omega_p^2}{(\omega_0^2 - \omega^2) - i\omega/\tau} \tag{5.11}$$

or in the language of conductivity

$$\tilde{\sigma}(\omega) = \frac{\omega_p^2\epsilon_0\omega}{\omega/\tau + i(\omega_0^2 + \omega^2)} \tag{5.12}$$

Finally, the real and imaginary parts of the optical conductivity are given as

$$\sigma_1(\omega) = \frac{\epsilon_0\omega_p^2\omega^2(1/\tau)}{(\omega_0^2 + \omega^2)^2 + (\omega/\tau)^2} \tag{5.13}$$

$$\sigma_2(\omega) = -\frac{\epsilon_0\omega_p^2\omega(\omega_0^2 - \omega^2)}{(\omega_0^2 + \omega^2)^2 + (\omega/\tau)^2} \tag{5.14}$$

Note that for $\omega_0 = 0$, we recover the Drude result.

The Lorentz σ_1 and σ_2 are plotted in Fig. 5.4 for the (a) under and (c) over-damped scenarios, with an oscillator frequency of 3 THz and damping constant of 150 and 15 fs, respectively. The degree of damping is more obvious when looking at the current impulse response in the time domain, shown in the insets of Fig. 5.4. For frequencies well below the resonant frequency, the real part of the conductivity is zero reflecting the pure polarization response of bound charges in a dielectric where the index of refraction is purely real and there is little or no absorption.

The time domain transmission response for a THz pulse through a thin film of the Lorentz conductivity shown in Fig.5.4(a) and (c) is given in Fig.5.4(b) and (d),

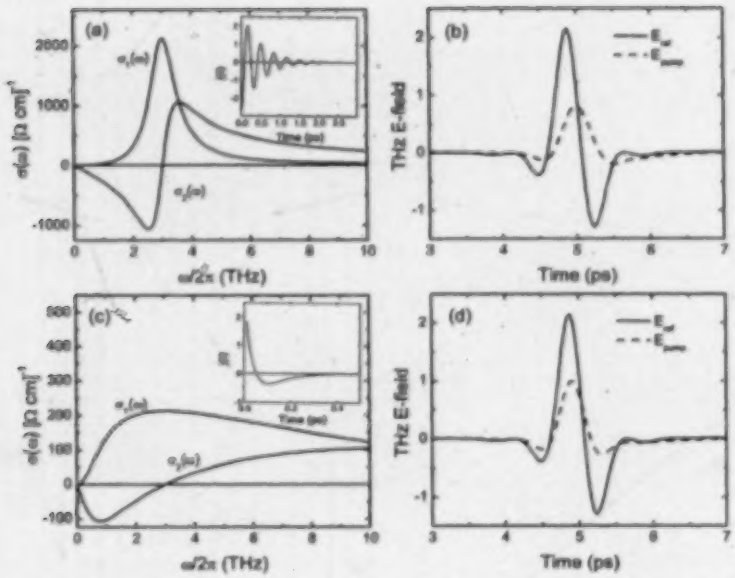

Figure 5.4: Lorentz conductivity of a thin film on a GaAs insulating substrate in (a) the underdamped ($\omega_0/2\pi = 3$ THz, $\tau = 150$ fs) and (c) the overdamped ($\omega_0/2\pi = 3$ THz, $\tau = 15$ fs) regime. The insets show the current response function, demonstrating the degree of dampening. The calculated change in THz pulse transmission using Eq. 5.8 is given in (b) and (d) for the film conductivity in (a) and (c), respectively.

respectively. The substrate index of refraction was 3.0. The conductivity induced phase shift is in the opposite direction as the Drude model, shifting the peak of the THz pulse to later times.

5.3 Carrier backscattering - Drude-Smith model

In the derivation for the Drude model, one of the main assumptions is elastic isotropic scattering resulting in complete momentum randomization. In other words, after each scattering event there is no memory of the carrier's previous momentum. This allows the decay of current to an impulse field to be described by a single exponential decay with a characteristic time of τ. The resulting Drude conductivity has a maximum σ_1 at the dc value and rolls off at higher frequency. The imaginary σ_2 rises to a peak at a frequency corresponding to the scattering rate. However, despite the success of the Drude model in describing ordered systems such as metals and photoexcited semiconductors, there exist systems which show strong deviations from the simple Drude model or its variants. Disordered systems such as quasicrystals [91] and percolative systems [92] show a suppression in the low frequency σ_1, rising to a peak at non-zero frequency. Accompanied by this suppression, although rarely treated in the literature due to the coherence required to obtain it, is a negative σ_2 that represents a capacitive, rather than a Drude-like inductive response.

There are few microscopic theories of conductivity in disordered media which treat both real and imaginary parts of the conductivity. A relatively new classical theory was formulated by Smith, with the goal of reproducing the typically observed conductivity features mentioned above, based on carrier backscattering [93]. By incorporating a memory effect into the scattering event, he found a simple, albeit phenomenological, form of the optical conductivity which can accurately describe many disordered systems (quasicrystals, liquid Te and Hg), close to the metal insulator transition. To do so, he employed the impulse response formalism where the optical conductivity is simply the Fourier transform of the current response function. He used Poisson statistics to describe the current response

function as

$$j(t)/j(0) = e^{-t/\tau}\left[1 + \sum_{n=1}^{\infty} c_n (t/\tau)^n/n!\right] \tag{5.15}$$

where c_n is the fraction of the carrier velocity retained after the n^{th} collision. The Fourier transform of this expression leads to the so-called Drude-Smith model for the optical conductivity,

$$\tilde{\sigma}(\omega) = \frac{\omega_p^2 \epsilon_0 \tau}{1 - i\omega\tau}\left[1 + \sum_{n=1}^{\infty} \frac{c_n}{(1 - i\omega\tau)^n}\right] \tag{5.16}$$

Normally, only the first order term is taken into account. This has the meaning that, in addition to the Drude leading term, there is only one other scattering event that deviates from regular isotropic Drude scattering since all the other c_n's are zero. Mayou has given a possible rationale behind this assumption in his work on the optical conductivity of quasicrystals, where the first collision is ballistic and subsequent collisions are diffusive [94]. Thus memory of previous momentum is retained after only one collision, and only one term is necessary in the sum. With this assumption and labeling c_1 as c, the real and imaginary parts of the conductivity can be written as

$$\sigma_1(\omega) = \frac{\omega_p^2 \epsilon_0 \tau}{[1 + (\omega\tau)^2]^2}[1 + (\omega\tau)^2 + c(1 - \omega^2\tau^2)] \tag{5.17}$$

$$\sigma_2(\omega) = \frac{\omega_p^2 \epsilon_0 \tau^2 \omega}{[1 + (\omega\tau)^2]^2}[1 + (\omega\tau)^2 + 2c] \tag{5.18}$$

Figure 5.5(a-d) shows the real and imaginary parts of the Drude-Smith conductivity given in Eqns. 5.17 and 5.18, for $\omega_p = 4 \times 10^{14}$ s^{-1}, $\tau = 10$ fs and various values of c ranging from 0 to -1. Fig. 5.5(a) shows the c=0 response, identical to Drude conductivity and corresponding to complete momentum randomization. Making c negative, as in (c-d), one can see a dip in the low frequency conductivity developing and the conductivity rising to a non-zero frequency peak. For values of $c < -1/3$, a minimum is established at zero frequency, with σ_1 rising to a peak at $\omega = \sqrt{(3c+1)/\tau^2(c-1)}$. For $c < -1/2$, σ_2 goes negative at low frequencies, consistent with the capacitive response mentioned above. At higher frequencies,

the response merges into the $\sigma_1(\omega) \sim 1/(\omega\tau)^2$ and $\sigma_2(\omega) \sim 1/\omega\tau$ Drude behaviour.

Figure 5.5(e-h) shows the changes in the THz transmission predicted for a thin Drude-Smith conducting film on glass, for the conductivities given in (a-d), respectively. One can see that while the peak of E_{pump} remains in the same position as the peak of E_{ref} for up to c = -0.8, there is a significant deviation from Drude conductivity. Thus, while the absence of a phase shift in the THz pulse means the response is primarily resistive, one must have further justification in applying a simple Drude model. This also serves as a cautionary note that small changes in the time domain data can lead to huge changes in the frequency domain, and one should always perform complete complex analysis before drawing any conclusions. One conceptual way to view localization in the Drude-Smith model is provided by examining the velocity response function, or in the words of the Kubo formalism, the velocity autocorrelation function $< v(t) >$ [95]. In the Drude-Smith model, $< v(t) >$ is given to first order as

$$< v(t) >= v_0 e^{-t/\tau}(1 + c\frac{t}{\tau}) \tag{5.19}$$

The first term is simply the Drude response function, followed by a linear deviation characterized by the backscattering parameter c. Integration of Eq. 5.19, we obtain the position autocorrelation function, $< x(t) >$, a measure of how far a carrier can travel after an impulse electric field, plotted for three c values in Fig. 5.6. In the c=0 case, $< x(t) >$ rises within a few τ's to a steady state value of $v_0\tau$, reflecting the regular diffusion length. For c = -0.5, $< x(t) >$ rises to a peak distance and then for longer times returns to a steady state value of $v_0\tau/2$, so the diffusion length is cut in half. Finally at c = -1, after rising to a peak at $t = \tau$ and then returning to zero, its original position, after undergoing complete backscattering. Since the total distance traveled by the carrier is zero after several τ's, there can be no contribution to a DC current and thus the DC conductivity is zero. The material is then described as an insulator.

Finally, an alternative derivation of the Drude-Smith model is provided by the Kubo formalism. In the derivation for the Drude conductivity, the velocity autocorrelation function is assumed to be $< v(t) > = e^{-\frac{t}{\tau}}$, or in other words any correlations in the momentum decay exponentially with a characteristic time scale

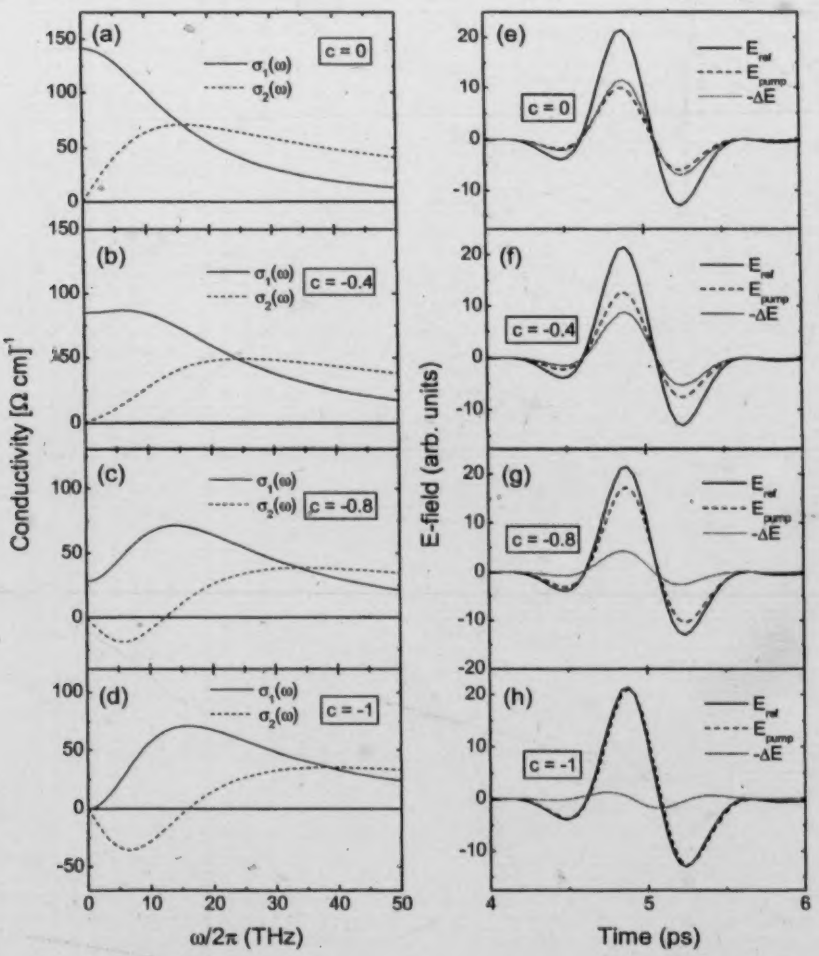

Figure 5.5: (a-d) Drude-Smith conductivity for plasma frequency $\omega_p = 4 \times 10^{14}$ s^{-1}, scattering time $\tau = 10$ fs and backscattering parameter ranging from 0 to -1 using Eq.'s 5.17 and 5.18. (e-h) Predicted changes in THz transmission through a 1 micron thick film on glass substrate, with the film conductivity corresponding to the plots in (a-d), using the complex transmission function calculated from the conductivities and Eq. 5.8.

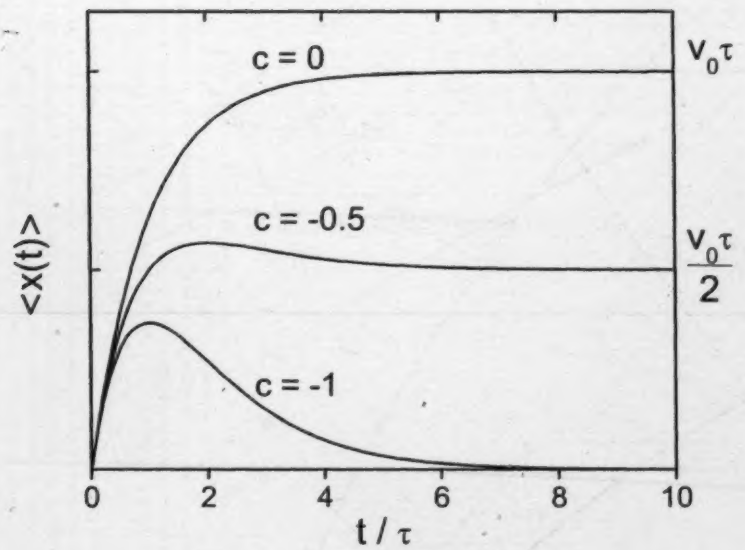

Figure 5.6: Position autocorrelation function for the Drude-Smith model, derived by integrating Eq. 5.19 for three values of the backscattering parameter c.

τ. Instead, we assume $< v(t) > = f(t)e^{-\frac{t}{\tau}}$ where f(t) is some normalized function that describes the deviation from exponential decay. The ac conductivity is given by the integral

$$\tilde{\sigma}(\omega) = \int_0^\infty f(t)e^{-\frac{t}{\tau}}e^{i\frac{\omega_d}{d}t} \tag{5.20}$$

Taking a Taylor expansion of $f(t) = 1 + \frac{df(0)}{dt}t + \frac{1}{2!}\frac{d^2f(0)}{dt^2} + \ldots$ returns the same form as Eq. 5.15. Integration of this response gives Eq. 5.16, with the c parameters being nothing more than the derivatives of the unknown function f(t) evaluated at t = 0 from the Taylor series expansion.

5.4 Sources of carrier scattering

As a charge carrier moves through a semiconductor in response to an applied field, it undergoes collisions with other entities with which it exchanges energy and momentum and scatters into another state. The important sources of scattering in a semiconductor can be classified into three categories: 1) defects, 2) carriers, and 3) phonons. We will look at each of these briefly to get a flavour for how each affects the transport properties of a semiconductor. Each mechanism has its respective scattering rate, which contributes to the overall scattering rate $\frac{1}{\tau(E,k)}$ via Matthiessen's rule.

5.4.1 Defect scattering

In a perfect lattice, charge carriers are described by Bloch waves and move unimpeded through the lattice. In other words, there is no intrinsic scattering of a carrier in a perfect crystal. However, such a perfect crystal does not exist, and there will always be some interruption in the periodicity of the lattice. These defects perturb the Bloch states, and thus are an important scattering mechanism in semiconductors. One of the most important forms of defect scattering are neutral and ionized impurity scattering. As the name suggests, neutral or ionized impurities refer to either intentionally or intrinsic impurities in the crystal whose charge species is electrically neutral or charged, respectively. Of the two, ionized impurity scattering is dominant due to the interaction of a charge carrier with the

electric field of the impurity. For typical charge carrier densities on the order of 10^{17-18} cm^{-3}, however, mobile carriers are attracted by the impurity which screen the electric potential exponentially on a length scale given by the Debye length, $L_D = \sqrt{\frac{\epsilon k_B T}{e^2 n}}$. Furthermore, when carriers have more kinetic energy, as they do for higher field strengths or at higher temperature (> 100 K), these stationary scatters have less effect on the initial momentum of the carrier because it spends less time within L_D of the impurity. The effect can be parameterized by writing $\tau(k) = \tau_0 \left(E/k_B T \right)^s$ where s is the characteristic exponent for ionized impurity scattering. When the screening is weak or moderate, s = 3/2, however, when screening is strong, as it typically is for carrier densities used in this thesis, s = -1/2 [96]. Thus ionized impurity scattering will work to lower the carrier mobility at low temperature.

Another form of defect scattering which is important in semiconductor alloys (as presented in Chapter 7) is alloy scattering. Here, local variation of alloy composition results in a local change in band gap energy. This change in potential results in a source of scattering similar to impurity scattering.

5.4.2 Carrier-carrier scattering

There are two types of carrier-carrier scattering: binary, such as electron-electron, hole-hole or electron-hole scattering, and collective where an electron or hole scatters from plasmons. In electron-electron or hole-hole scattering, the total energy or momentum of the distribution can not be changed by self-scattering. As such, the mobility is only effected through higher moments of the distribution [97]. For electron-hole scattering, however, in the center-of-mass frame of reference the event looks exactly like impurity scattering and it can contribute to a relaxation of current [98]. The scattering rate was calculated in a classical regime (non-degenerate case) to be $\frac{1}{\tau} \sim n|ln(n)|$, approximately linear with excitation density [97].

5.4.3 Phonon scattering

For carrier densities below the dominating regime of carrier-carrier scattering, the most important scattering mechanism at room temperature is due to carrier-phonon scattering, provided carriers have thermalized to the lattice. As the lattice

moves it causes a change in the lattice constant, which in turn causes a change in the band structure of the semiconductor. This perturbation leads to scattering of a charge carrier moving through the lattice. There are both acoustic and optical deformation potentials, which act through the strain and displacement of the lattice, respectively. In polar semiconductors, such as GaAs, the local variations in lattice spacing leads to a temporary change in the dipole moment set up between the positively charged arsenic atom and the negatively charged gallium atom. This sets up an electric field that can scatter charge carriers very efficiently, either through polar acoustic (piezoelectric scattering) or polar optical phonons. In GaAs the mobility is almost entirely determined by the scattering induced by polar optical scattering for temperatures above 80 K. Again, the scattering time temperature dependence can be parameterized as $\tau = \tau_0\left(E/k_BT\right)^s$ with s = 2.3 [96].

Part III

Experimental Results and Discussion

Chapter 6

Gallium arsenide - A case study

In this section, we will explore a prototypical semiconducting system which has been extensively studied by THz-TDS and TRTS, and thus has become an excellent reference material to benchmark the THz spectroscopy setup. Gallium arsenide (GaAs) is a cubic, direct bandgap semiconductor with an energy gap located at the Γ point in the Brillouin zone. The room temperature bandgap energy is 1.424 eV and increases slightly to 1.52 eV towards 0 K. The band structure of GaAs is given in Fig. 6.1, showing important satellite valleys at the X and L points, located 1.71 eV and 1.9 eV above the valence band maximum at the Γ point. When investigating the electronic properties of a semiconductor, knowledge of the band structure is important since it determines the effective mass of a charge carrier, $m^* = \hbar^2 \left[\frac{d^2E}{dk^2}\right]^{-1}$ as well as indicates whether a carrier has sufficient energy to scatter into a typically lower-mobility satellite valley.

6.1 GaAs - Insulating state

Non-photoexcited semi-insulating GaAs (SI GaAs) is essentially an insulator at room temperature, with a resistivity on the order of 10^7 Ω cm. With virtually no carriers populating the conduction or valence bands, the contribution to the dielectric response in the THz range from free charge carriers is insignificant. The response is thus dominated by bound oscillators in the THz range, and for GaAs the main contribution is from optically active phonons. To experimentally show this, a

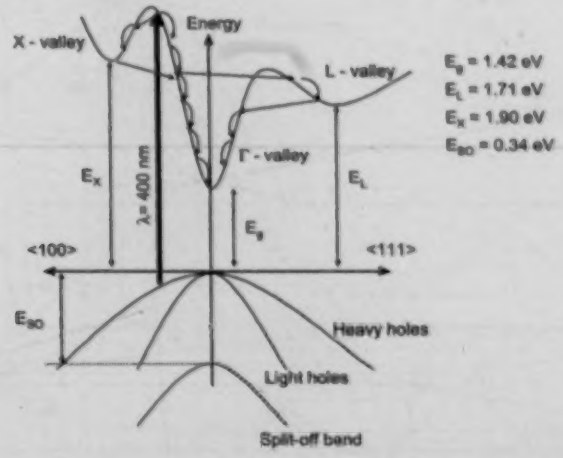

Figure 6.1: Schematic of the band structure of GaAs, with energy gaps and satellite valleys indicated, as well as inter-band and intra-band transitions. Adapted from Ref. [2].

1.83 mm thick SI GaAs slab was investigated with THz-TDS to extract the complex index of refraction using the method outlined in Chapter 3. Fig. 6.2 shows the time domain THz waveforms recorded with and without the sample. Immediately there is a shift in the arrival time of the THz pulse by 15.85 ps, and neglecting absorption one can make a quick estimate of the index of refraction using $\Delta t = \frac{L}{c}(N-1)$ with L = 1.83 mm to get N = 3.59. Performing the complete complex analysis, first by taking the Fourier transforms of the reference and sample waveforms, giving the amplitude and phase of the two scans shown in Fig. 6.3. Taking the ratio of the amplitudes to give the magnitude of the complex transmission function, $|T(\omega)| = \frac{|E_{samp}(\omega)|}{|E_{ref}(\omega)|}$ and the phase, $\Phi(\omega) = \phi_{sample}(\omega) - \phi_{ref}(\omega)$ in radians, shown in Fig. 6.4, one has all the information one needs to extract the complex dielectric function of the unexcited GaAs slab. Using the Maple program in Appendix A.6 to numerically invert the appropriate Fresnel equations given in Eqns 3.8 and 3.9, we obtain the index of refraction N, roughly dispersionless at a value of 3.6, and the extinction coefficient κ, that is approximately zero. To better understand the slight dispersion observed in the index of refraction, we can transform the data

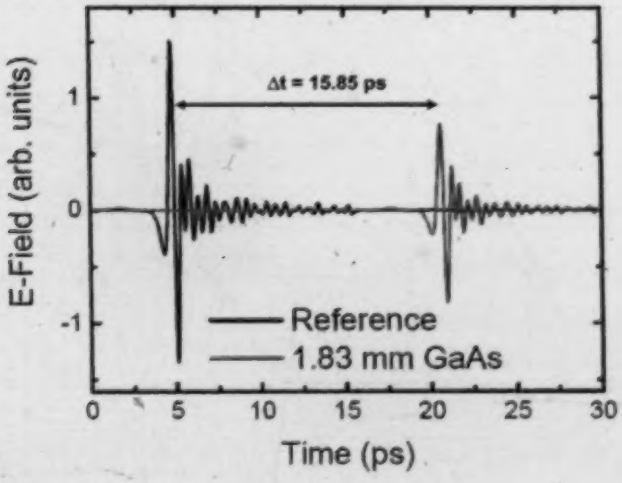

Figure 6.2: THz-TDS reference (no sample) and sample (1.83 mm thick GaAs slab) scans.

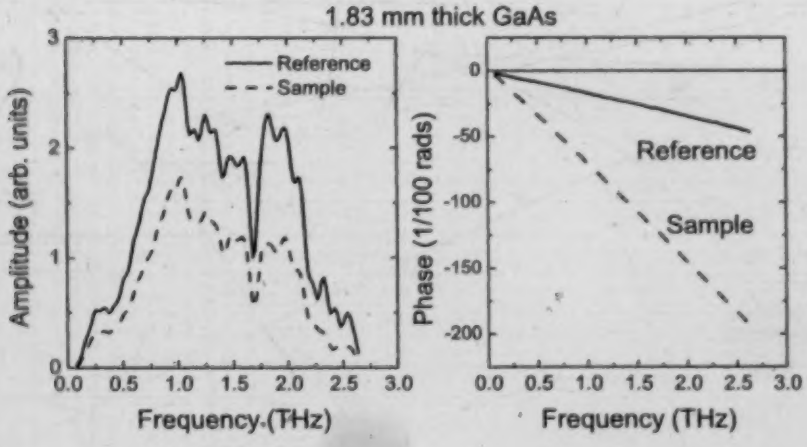

Figure 6.3: Amplitude and phase data from the Fourier transform of the waveforms in Fig. 6.2

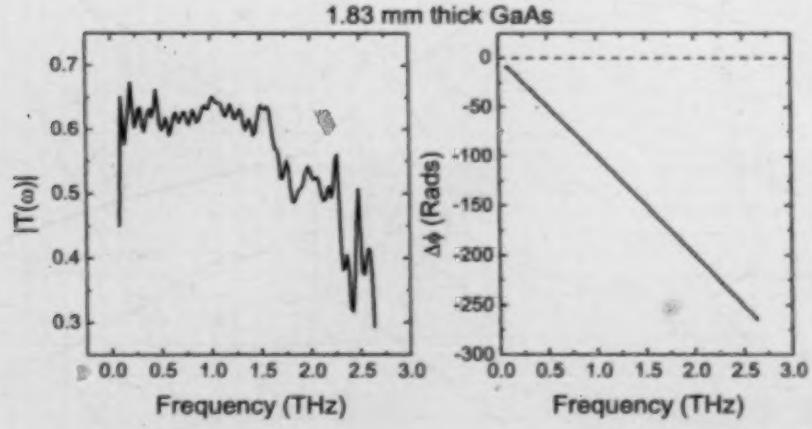

Figure 6.4: Transmission coefficient and phase difference for the waveforms given in Fig. 6.2

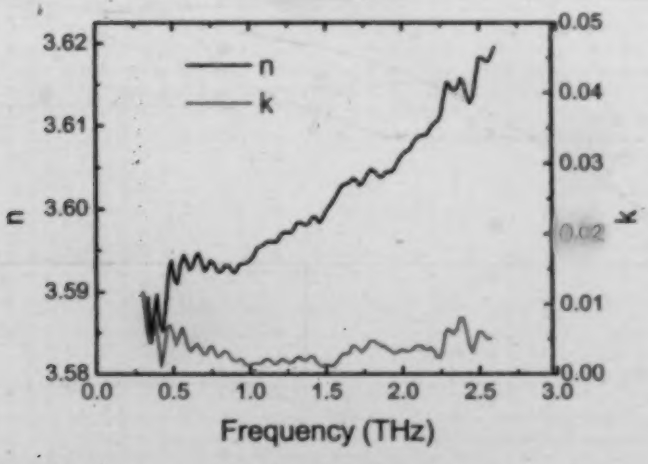

Figure 6.5: Extracted real (n) and imaginary (k) parts of the complex index of refraction for a 1.83 mm-thick SI GaAs using THz-TDS.

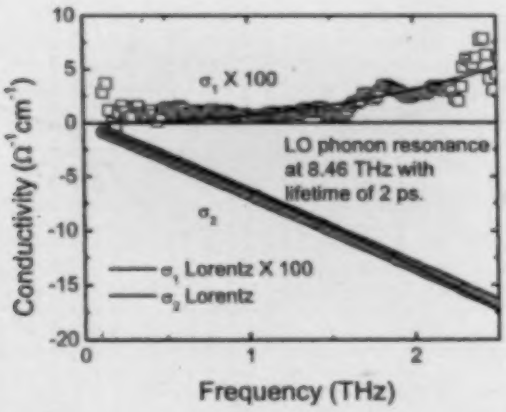

Figure 6.6: Extracted complex conductivity for a 1.83 mm-thick SI GaAs using THz-TDS. Lines are fits to the real and imaginary parts of the Lorentz model, with oscillator frequency $\omega_0 = 8.4 \pm 0.1$ THz and lifetime $\tau = 2$ ps.

given in Fig. 6.5 into complex conductivity using the relations in Table A.1. The resulting conductivity is given in Fig. 6.6. One can see that there is negligible real conductivity, reflecting the fact that SI GaAs is effectively an insulator, and a negative imaginary conductivity characteristic of an insulating response as we saw earlier in the Lorentz model. Fitting the conductivity data with a Lorentz oscillator model, the data is described reasonably well using an oscillator frequency at 8.4±0.1 THz, in between a transverse optical (TO) phonon at 8.02 THz and longitudinal optical (LO) phonon at 8.55 THz [99]. The lifetime of the oscillator is estimated at 2 ps, which is comparable with literature values of the LO phonon lifetime of $\sim$ 3.5 ps [100]. Our value of 2 ps might be slightly shorter (wider oscillator peak) because we are sensitive to the TO phonon as well. However, we note that the confidence in these numbers are still low because the oscillator is so far out of the bandwidth of the THz pulse, such that no identifiable features of the Lorentz oscillator are visible in this range.

6.2 GaAs - Photoconductive state

The electronic bandstructure of GaAs is given in Fig. 6.1. Because the optical band gap energy for GaAs is ~ 1.42 eV, an optical excitation with wavelengths lower than 874 nm will introduce electrons and holes into the conduction and valence bands, respectively. Once carriers are injected, they can relax through several stages that occur over different time scales. For the first few 100 fs, a coherent regime exists where scattering mechanisms have not destroyed the phase relationship between the excitations and the electromagnetic fields that created them. This is outside the scope of this thesis, since TRTS can only accurately probe the conductive state with a time resolution of roughly 500 fs after photoexcitation, limited by the THz pulse width. For times ≤ 2 ps, a non-thermal regime exists where the carrier distribution function cannot be described by a single temperature [7]. This is the realm of electron-hole scattering, electron-optical phonon scattering and intervalley scattering. Following this regime, from $\sim 1 - 100$ ps the carriers thermalize to a temperature which is still not in equilibrium with the lattice, and the carrier distribution exchanges energy with the lattice via emission of optical phonons until, for times > 100 ps, carriers and the lattice, as well as excitons, are described by the same temperature. At this time, carriers can undergo recombination, which returns the system back into the equilibrium state it was in before photoexcitation. Recombination can be classified as radiative or non-radiative, defined by whether or not a photon is emitted.

We now turn our attention to the conductivity dynamics and frequency response of these injected charge carriers, measured on ps time scales by TRTS. Absorption of a photon with energy greater than the bandgap will lead to a vertical interband transition (since the momentum of the photon is negligible) from the valence band to the conduction band, leaving a mobile hole in the valence band and a mobile electron in the conduction band. If the energy of the photon exceeds the bandgap energy considerably, as is the case in Fig. 6.1, the injected electron can have sufficient kinetic energy to scatter to satellite X and L valleys, where the effective mass is significantly larger than in the central Γ valley [11, 101]. Within a band, optical phonon scattering is the main source of intraband relaxation, again shown in Fig. 6.1. Eventually, carriers can scatter back into the high-mobility Γ

valley by phonon scattering, which occurs within 2-6 ps of excitation, depending on the excess energy [101].

The transient complex conductivity of photoexcited GaAs can be well described by a simple Drude model [67], although some authors have used variations of the Drude form to describe their data [11]. Terahertz spectroscopy is an excellent probe of the nonequilibrium conductivity for GaAs, because typical scattering times are on the order of 100 - 500 fs, so the identifiable crossover point where $\sigma_1 = \sigma_2$ at a frequency $\frac{1}{2\pi\tau}$ is on the order of 0.3 - 1.5 THz, well within the bandwidth of TRTS. In Fig. 6.7, the time-domain TRTS data and the derived transient complex conductivity of 400 nm pumped semi-insulating GaAs (SI GaAs) is given for three pump fluences, (a,b) 0.25, (c,d) 1.0 and (e,f) 2.0 μJ/cm^2, taken at 10 K. The pump beam spot was spread over a 1.5 mm aperture that supported the sample. Because the photoinduced changes in the THz pulse are small for the smallest pump fluences, we have also plotted the negative change in THz transmission, -$\Delta E(t)$. The first thing to note is in the time domain data, where the peak of the E_{pump} waveform shifts to earlier times with respect to the reference pulse, as was shown in the previous section and connected with a phase shift occurring at the boundary of the photoexcited layer [67]. Examining the conductivity data we see that for the lowest excitation, corresponding to a carrier density of 7.8×10^{17} cm^{-3}, the peak of σ_2 overlaps with σ_1 curve at 0.29 THz, at the low frequency limit of the pulse bandwidth. This frequency corresponds to $\tau = 545$ fs and an electron mobility of 14300 cm^2/Vs, which is in good agreement with literature values at 10 K [102]. With increasing excitation, the mobility is observed to decrease, roughly linearly with carrier density in agreement with predictions of electron-hole scattering [98], which can act to lower the carrier mobility at photoexcited densities higher than 8×10^{16} cm^{-3} [103].

Equivalent to the complex conductivity, one can also think in terms of the dielectric function or index of refraction, as these are related through the equations given in Table A.1. Fig. 6.8 demonstrates this conversion, showing that the dielectric function also shows spectral features which allow easy determination of the carrier scattering time, namely the crossover point where $-\epsilon_1 = \epsilon_2 - \epsilon_b \approx \epsilon_2$. The complex index of refraction, however, has only a broad kink in the frequency dependence of n and k at the scattering frequency, which makes it more difficult to

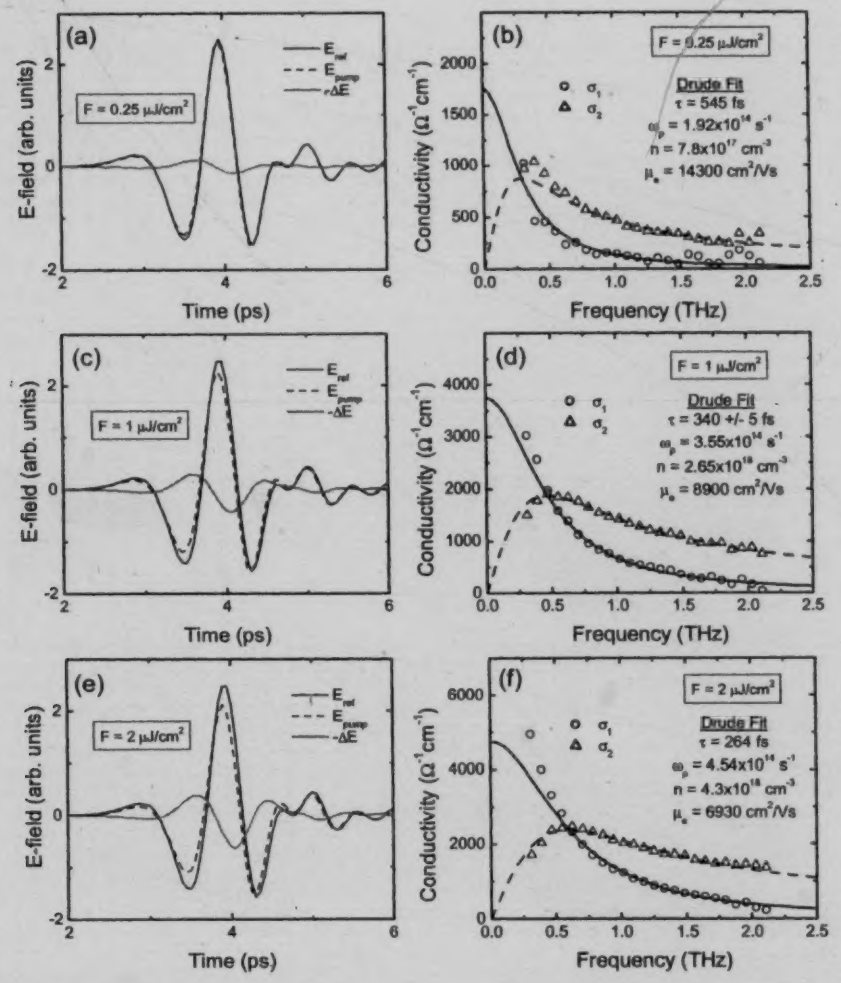

Figure 6.7: TRTS time domain data for a SI GaAs sample, 20 ps after 400 nm photoexcitation at 10 K, with extracted complex conductivity. Pump fluence is (a,b) 0.25, (c,d) 1.0 and (e,f) 2.0 μJ/cm^2. The lines over the conductivity data are simultaneous Drude fits to σ_1 and σ_2 with parameters given in the figures, assuming an electron effective mass of 0.067 m_e.

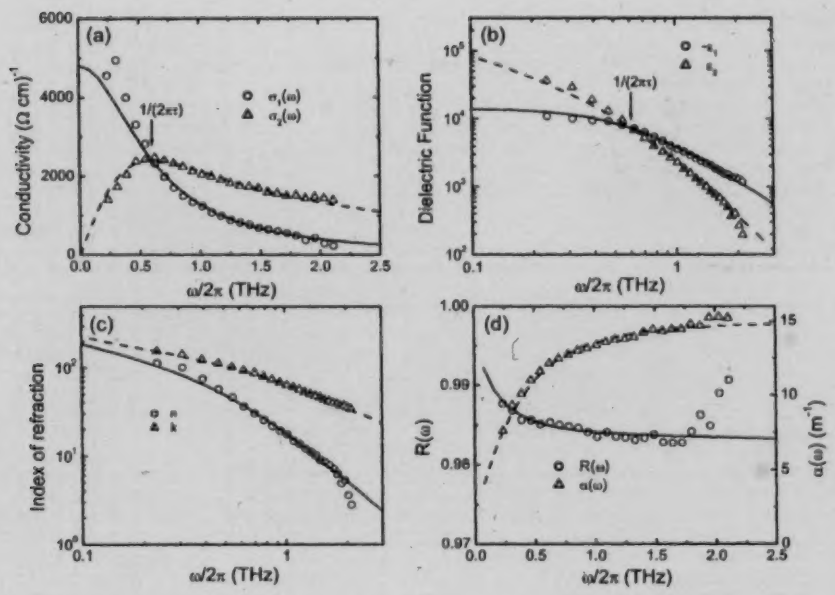

Figure 6.8: Optical parameters extracted for GaAs photoexcited with 2.0 $\mu J/cm^2$ of 400 nm light, 20 ps after excitation, at 10 K. Shown is the a) optical conductivity, b) dielectric function, c) complex index of refraction and d) reflection and absorption coefficient, calculated using the relations given in Table A.1 in Appendix A.7. The solid and dashed lines are Drude fits to the real and imaginary parts of the optical parameters with plasma frequency $\omega_p/2\pi = 72.6$ THz and a scattering time $\tau = 264$ fs.

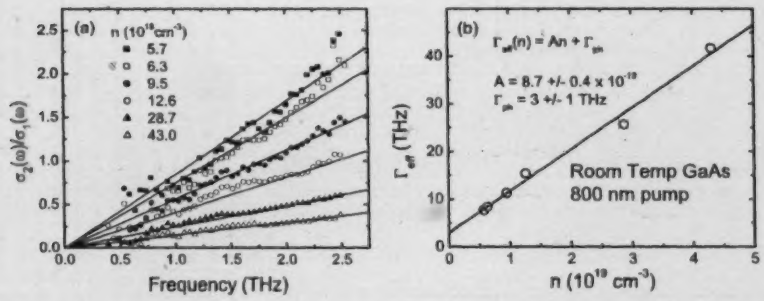

Figure 6.9: a) Ratio of imaginary to real part of the complex conductivity for 800 nm photoexcited GaAs at room temperature. Carrier densities are indicated and the lines are least squares linear fits to the data. b) Extracted scattering rates for the various carrier densities, and a linear least squares fit to the data showing the increase in carrier-carrier scattering, roughly linear with excitation, and the intercept phonon scattering rate of 3 ± 1 THz

assign a definitive scattering time. Throughout this thesis, the optical conductivity will be used to describe the response of the system, however Fig. 6.8 shows that the dielectric function could also easily be used. The field reflection and absorption coefficients are plotted in Fig. 6.8(d) for completeness, showing the characteristic upturn of $r(\omega)$ as $\omega \rightarrow 0$ in the Hagens-Rubens regime.

Since carrier densities are often above 1×10^{17} cm^{-3} in TRTS experiments, a room temperature investigation into this effect on GaAs was conducted to determine to what extent e-h scattering is dominant when phonon scattering is also present. Fig. 6.9(a) shows the ratio of $\sigma_2/\sigma_1 = \omega\tau$ for various excitations, taken at room temperature with a 800 nm pump. One can see with increasing excitation the slope of the ratio decreases, corresponding to a decrease in scattering time. Fig. 6.9(b) shows the effective scattering rate derived from the slopes in (a), as a function of carrier density. The scattering rate proceeds linearly with n [103], with a slope of $8.7 \pm 0.4 \times 10^{-19}$ and an intercept of 3 ± 1 THz, corresponding

to the bare phonon scattering rate. This gives an estimate of the highest room temperature mobility of 9000±2000 cm^2/Vs, in good agreement with the literature value of 8000 cm^2/Vs [104].

The dynamics of the photoconductive state are determined by the presence of mobile charge carriers in the material and the mechanisms which deplete either the charge density (carrier recombination) or the mobility (trapping into an immobile localized state). In a high quality, bulk semiconductor sample such as a slab of SI GaAs, the main source of localized states which can trap carriers are located at the surface, where the lattice periodicity abruptly ends. Obviously, the penetration depth of the initial excitation determines how much these states influence the photoconductive decay. For an 800 nm excitation, where the penetration depth is on the order of 1 μm [89], carriers are injected far into the bulk away from the surface and thus the recombination is determined by bulk recombination. To quantify this effect, one must look at the time evolution of the spatial distribution of carriers within the sample after initial injection. In the absence of an external DC electric field, the equation which describes the evolution of the carrier distribution n(x,t) in a semi-infinite semiconductor after injection by a pump pulse with absorption coefficient α is

$$\frac{\partial n(x,t)}{\partial t} = D\frac{\partial^2 n(x,t)}{\partial x^2} - \frac{n(x,t)}{\tau_b} + n_0\delta(t)exp(-\alpha x) \tag{6.1}$$

where D is the diffusion coefficient given by $D = \sqrt{\frac{\mu_{ab}k_BT}{e}}$, μ_{ab} is the ambipolar mobility ($\mu_{ab} = \frac{\mu_e\mu_h}{\mu_e+\mu_h}$) and τ_b is the radiative recombination time. The surface recombination is incorporated through the boundary condition $n(0,t) = \frac{D}{s}\frac{\partial n(x,t)}{\partial t}\Big|_{x=0}$, n(l,t) = 0 and n(x,0) = 0, where s is the surface recombination velocity and l is an arbitrarily large distance. It is necessary to use the ambipolar mobility since we are exciting an equal population of electrons as holes which are oppositely charged, and so one distribution can not leave the other behind as it moves. The solution to Eq. 6.1 is somewhat lengthy, but can be found in Ref. [11].

Fig. 6.10(a) shows the normalized one-dimensional differential THz transmission of 400 nm and 800 nm photoexcited SI GaAs for a pump fluence of 20 $\mu J/cm^2$. The 400 nm excitation produces a much faster photoconductive decay than the 800

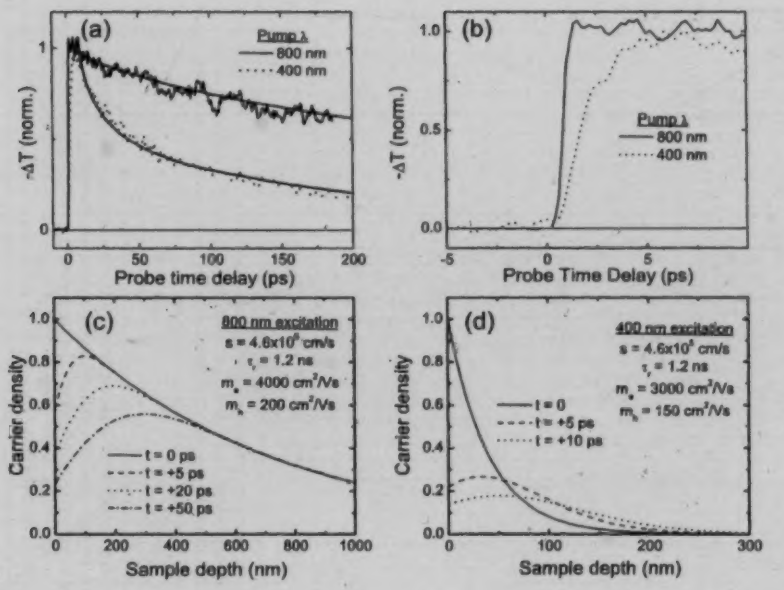

Figure 6.10: (a) Normalized negative differential THz transmission after 800 nm and 400 nm excitation at room temperature under similar pump powers. The solid lines are fits to the spatially integrated solution to Eq. 6.1 with parameters given in (c) and (d). (b) Rise times of the scans shown in (a). The solution for the diffusion equation given in Eq. 6.1 is plotted for (c) 800 and (d) 400 nm excitation, respectively, with parameters given in the plot.

nm excitation because carriers are injected within tens of nm from the surface under 400 nm excitation (d = 14.7 nm) while for 800 nm excitation they are injected over 700 - 1000 nm. The decay can be well described by the integrated solution of Eq. 6.1, $n(t) = \int_0^\infty n(x,t)dx$, shown as solid lines in Fig. 6.10(a) assuming a common surface recombination velocity of 4.6×10^5 cm/s and carrier recombination time of 1.2 ns, but penetration depths $\delta_{800nm} = 700$ nm and $\delta_{400nm} = 40$ nm. We note that 40 nm is slightly higher than the 15 nm literature value, but the diffusion equation could not be numerically solved in a sufficient range of pump-probe delay times.

The spatial distribution of carriers is plotted in Fig. 6.10(c) and (d) for the same parameters used to fit the $-\Delta T(t)$ scans in Fig. 6.10(a), for several indicated pump-probe time delays. One can see the effect of surface recombination is to deplete carriers immediately at the surface, which is more efficient for 400 nm excitation than 800 nm excitation, because the initial 400 nm excitation distribution is closer to the surface.

There is also a noticeable difference between the two excitation wavelengths in the photoconductive rise time, seen in Fig. 6.10(b). After 800 nm excitation, there is an immediate (resolution limited, < 0.5 ps) rise to a maximum photoconductive signal, followed by the long lived decay. For the 400 nm excitation, the rise of photoconductivity is comparatively gradual, taking approximately 6 ps to reach a maximum. The delay in reaching a maximum photoconductivity is due to intervalley scattering to the lower-mobility satellite X and L valleys, since carriers are given sufficient energy to reach these bands [101, 11]. It then takes a few picoseconds for carriers to scatter back into the high mobility Γ valley, producing a delayed photoconductivity maximum.

Chapter 7

Isovalently doped gallium arsenide alloys

7.1 Introduction to isovalent III-V alloys

There is currently a worldwide search for a semiconducting material that has a direct bandgap energy (E_g) of $\sim$ 1.0 eV that can be lattice-matched to GaAs for device integration. There are very few direct bandgap semiconductors with E_g in the technologically important spectral window of 1.3 - 1.5 μm, where telecommunications devices normally operate because of the transmission windows in this wavelength range in typical fiber optic cables. Finding a suitable material that has this reduction in E_g while maintaining the direct bandgap nature is crucial for many optoelectronic applications. One such application is improving the efficiency of long wavelength vertical cavity surface emitting lasers [105]. This has obvious implications in the telecommunications industry where researchers are constantly looking for more efficient and faster switching lasers. Also, next generation multi-layered solar cells require a material in the 1.0 eV range for efficient conversion of a significant portion of the sun's luminosity. The multi-layered aspect of these devices impose a stringent requirement that the material be lattice-matched to GaAs, which rules out materials such as InGaAs with a $\sim$ 5% lattice mis-match at E_g = 1.0 eV. A third application is in future heterojunction bipolar transistors (HBTs), where a reduced bandgap base layer leads to a lower turn-on voltage

[22]. HBTs are of primary use in microwave amplifier circuits in cellular phone technology.

When a material is doped with an element of the same chemical valency as the host material, it is called isoelectronic doping because this does not change the charge state of the material. In conventional isoelectronically doped materials, such as $In_xGa_{1-x}As$ and $Al_xGa_{1-x}As$ where In and Al substitute the Ga, the material properties change smoothly between GaAs to InAs or AlAs as $x = 0 \rightarrow 1$. One such property is the bandgap energy, which, for constituents A and B of the alloy A_xB_{1-x}, E_g, behaves as

$$E_g^{A_xB_{1-x}} = xE_g^A + (1-x)E_g^B - bx(1-x) \tag{7.1}$$

Similar relations also exist for lattice parameters and mixing enthalpy. For conventional isoelectronic doping, the linear term dominates and b, the bowing coefficient, is small (1 eV) and composition independent.

7.1.1 GaN_xAs_{1-x}

In some cases, however, the impurity atom is sufficiently different from the host that it significantly perturbs the electronic structure of the material. This is of incredible technological interest because of the tunable optical and electrical properties of these alloys with very small (a few %) impurity concentrations. In these materials, the dopant atom is similar in valence and electron affinity to the host atom, but has underlying differences such as size and nuclear potential which interact with the host matrix to drastically influence the properties such as the radiative emission properties in GaP:N and, of particular interest, the recently discovered giant E_g reduction in GaN_xAs_{1-x}. With very dilute N alloying ($x < 4\%$), researchers predicted [106] and experimentally confirmed [107, 20] a large bandgap reduction leading to a direct bandgap with $E_g \sim 1$ eV. The measured bowing coefficient in dilute GaNAs was approximately 16 - 20 eV for 1% N, although b decreases to about 5 eV at 2% N. Furthermore, co-alloying with the larger In allows lattice matching to GaAs, making it very attractive for device applications, offering a way around material limitations to make advances in technologically important devices. Much research has been conducted to try and integrate III-V nitrides into lasers [108],

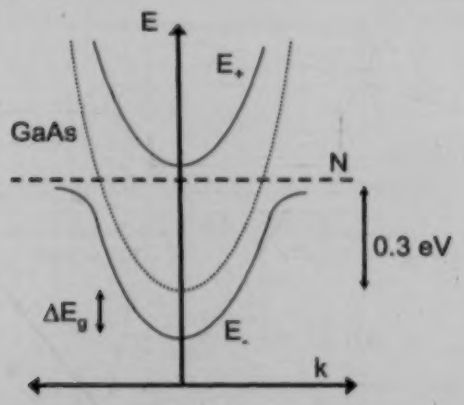

Figure 7.1: Schematic of GaAsN band structure, showing the resonant N level with the conduction band, and the resultant splitting into upper (E_+) and lower (E_-) bands.

> 40% efficiency multi-layered solar cells [21], and optoelectronic devices [109].

A caveat of this bandgap reduction soon became evident in the efforts to integrate III-V nitrides into devices. The electron mobility of GaAsN was found to be severely degraded compared to GaAs, detracting from the initial potential for technological breakthroughs [110, 111, 23]. It was discovered that the same mechanism which was responsible for the bandgap reduction in these materials was also responsible for the significant degradation of the electrical transport properties, namely the formation of an impurity band within the conduction band leading to localized electronic states [106, 112]. This is thought to be due to a N dopant state lying approximately 0.3 eV above the conduction band minimum. For $x > 0.8\%$, a resonant interaction with the conduction band of GaAs causes a splitting of the conduction band into an upper and lower band [113, 114], schematically shown in Fig. 7.1, with the upper band moving to higher energies with increasing N concentration, and the lower moving down in energy producing the observed reduction in the optical bandgap energy. The upper band is thought to be localized, and the bottom extended, but the situations are reversed under application of pressure greater than 4.5 GPa [113].

The degradation of electron mobility is related to the resonant interaction with

the conduction band, creating bound states localized to the N impurities. There has been some controversy as to whether the impurity states hybridize to form an impurity band [112], or remain as isolated cluster states [115], however it is generally agreed upon that the potential fluctuations larger than 30 meV introduced by the N clusters are responsible for a reduced electron mobility [24, 116, 117, 23]. So even though the N resonant states induce the favorable reduction in energy gap, it has been found that this must coincide with a reduction of electron mobility due to N impurity scattering [24, 117, 116]. To date, there have been no experimental studies of the ultrafast THz conductivity of GaAsN, although the limit of x = 1 has been explored in doped GaN free-standing films finding an excellent fit to a simple Drude model [118].

7.1.2 A new alloy: $GaAs_{1-x}Bi_x$

An anomalously large reduction in the bandgap, or giant bandgap bowing, was also observed for GaAs where host As atoms are replaced by dilute amounts of isovalent Bi [107]. The bowing coefficient in GaAsBi is concentration independent, and the bandgap is reduced at a linearized rate of 88 meV/% in an unstrained film and 83 meV/% in the strained film on a GaAs substrate, in the 0-3.6 % Bi concentration range [25]. As stated above, in dilute nitride alloys the bandgap reduction is due to the resonant interaction of a nitrogen state with the conduction band [106, 113, 114]. Similarly for the Bi alloy the bandgap reduction is believed to be due to a resonant interaction with the top of the valence band [119]. The dilute nitride alloys show strong impurity scattering for electrons [120, 24, 117, 116] and carrier localization effects consistent with a strong interaction between N and the states at the bottom of the conduction band [115]. The effect of dilute Bi alloying on the transport properties of GaAs has been unexplored to date, and is the subject of this work. GaAsBi is a promising material for spintronic applications, due to a recently observed large spin-orbit correction to the split-off band for Bi concentrations in the range of 0 - 1.8% [121]. There are also applications for GaAsBi in THz optoelectronic applications, where GaAsBi, with its reduced bandgap, can be used in photoconductive switches using lasers of longer wavelength, like fiber lasers, than the typical 800 nm output from Ti:sapphire mode-locked sources [122].

7.2 TRTS study of dilute GaAs nitrides and bismides

We use time-resolved terahertz (THz) spectroscopy (TRTS) to monitor the transient photoconductive (PC) decay of GaNAs, GaAsBi and GaNAsBi samples after optical injection of carriers with 400 nm, femtosecond light pulses [84]. The transient complex ac conductivity of GaAsBi is found to be well described by a simple Drude model, revealing a carrier mobility that is relatively unaffected by dilute Bi doping compared to a bulk GaAs reference. GaNAs and GaNAsBi, however, show signs of carrier localization in a suppressed real part of the complex conductivity at low frequency, consistent with localized states in the conduction band associated with N clustering [23, 115]. In this study three $GaAs_{1-y}Bi_y$ films (y = 0.84%, 1%, 1.4%, thicknesses of 260, 200 and 260 nm, respectively), one 225 nm thick GaN_xAs_{1-x} film (x = 0.84%) and one 170 nm thick $GaN_xAs_{1-x-y}Bi_y$ (x=0.85%, y=1.4%) film were compared to a reference sample consisting of a 200 nm thick GaAs buffer layer. The films were grown by solid-source molecular beam epitaxy (MBE) on (001) GaAs substrates following thermal deoxidation and growth of 200 nm thick GaAs buffer layers at 580°C. The growth was done by Tom Tiedje's group in the Department of Physics at the University of British Columbia. Activated N was provided by a low-pressure RF plasma source and conventional effusion cells were used for Ga, Al and Bi, and a two-zone cracker source for As_2. The GaNAs film was grown at a substrate temperature of 440 °C, while the GaAsBi and GaNAsBi samples were grown at lower temperatures (340-400 °C) and reduced Ga/As flux ratios (~1) in order to achieve Bi incorporation. The GaAs buffer layer was grown at 550 °C. Film compositions were determined by simulation of high-resolution x-ray diffraction rocking curve measurements [123].

For the extraction of the complex conductivity, a pump wavelength of 400 nm was chosen so the excitation was confined to the film, with a penetration depth of 15 nm for bulk GaAs [89]. We note that for the lower bandgap energies in these GaAsBi films, δ would only get smaller. The pump fluence was set to 3.7 $\mu J/cm^2$, dispersed over a spot size of 1.5 mm diameter on the sample, which was mounted on a 1.5 mm diameter anodized aluminum aperture. All measurements were taken at room temperature in a nitrogen-purged environment to minimize the effects of

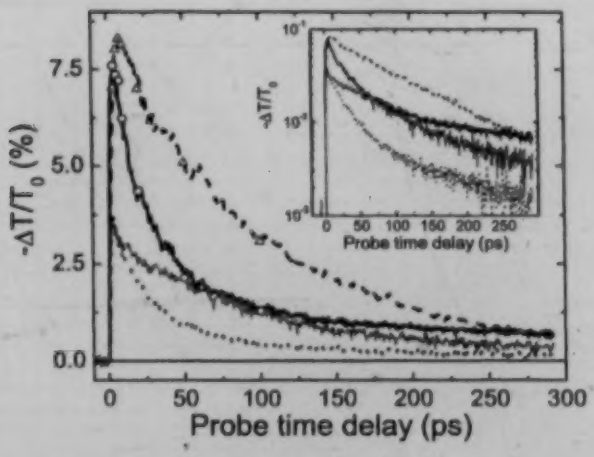

Figure 7.2: Negative differential THz transmission ($-\Delta T/T_0$) for the GaAs buffer layer (solid black), GaAsBi (0.84 % Bi) (dashed), GaNAs (0.84 % N) (dotted) and GaNAsBi (0.85% N, 1.4% Bi) (grey) samples, at a pump fluence of 3.7 $\mu J/cm^2$. The open symbols are carrier densities normalized to the peak $-\Delta T/T_0$, derived from the Drude fits to the complex conductivity for the GaAs buffer (○), and GaAsBi (△) samples. Inset is the same data on a semi-log plot.

water absorption on the spectroscopy (see Appendix A.1).

Figure 7.2 shows the $-\Delta T/T_0$ transients for the GaAsBi (0.84% Bi), GaNAs (0.84% N), GaNAsBi (0.85% N, 1.4% Bi) and the reference GaAs buffer layer. As mentioned previously, the peak $-\Delta T/T_0$ is a measure of the electron mobility given the same excitation density. The significantly lower GaNAs and GaNAsBi signals compared to the buffer and bismide samples are a strong initial indication that N severely reduces carrier mobility while Bi does not. The photoconductive decay for the GaAs (GaNAs) samples is well described by a biexponential decay with fast and slow time constants of 22 (23) and 260 (170) ps, respectively. This fast decay is likely due to surface recombination, which is efficient since the majority of carriers are injected within 20 nm of the surface. The GaAsBi film however, showed a clear single exponential decay of 101±1 ps, as seen in the inset of Fig. 7.2. This

indicates a single, fast, free-carrier depletion mechanism which is not likely due to surface recombination, since this would lead to a different non-exponential decay [11]. A more likely explanation is due to a distribution of trap centers distributed throughout the film. The GaNAsBi film showed a primarily single exponential decay with a time constant of 86 ps, with a small (10% of signal), longer-lived component not resolved by the length of our scan. That the bismide films did not show the typical photoconductive decay characteristic of surface recombination may be due to a reduction in hole mobility, which would reduce the ambipolar mobility and limit diffusion back towards the sample surface.

Figure 7.3 presents the frequency resolved complex conductivity for the samples shown in Fig. 7.2, 10 ps after photoexcitation. At 400 nm excitation, excited carriers have sufficient energy to scatter into satellite valleys in bulk GaAs. After ~6 ps, carriers have relaxed into the high mobility Γ-valley and an accurate, low-field mobility value can be obtained [11] (see also Section 6.2). For the GaAs buffer layer, both $\sigma_1(\omega)$ and $\sigma_2(\omega)$ are well described by a simple Drude model, as shown in Fig. 7.3(a). Using a bulk GaAs electron effective mass, $m^*_{GaAs} = 0.067m_e$, the simultaneous fitting of $\sigma_1(\omega)$ and $\sigma_2(\omega)$ to this data gives a carrier density $n = 1.8 \times 10^{18}$ cm^{-3} and mobility $\mu_e = 4100$ cm^2/Vs, in good agreement with the maximum density of 2.6×10^{18} cm^{-3} calculated from the pump fluence and with literature μ_e values [124]. We note that it is necessary to quote the mobility along with the carrier density as e-h scattering can play a role in limiting the mobility at these levels of excitation.

Examining the extracted conductivity data for the GaAsBi sample in Fig. 7.3(b), we see again that the complex conductivity is well described by a free-carrier Drude model with $\mu_e = 3020\ cm^2/Vs$ at $n = 2.7 \times 10^{18}\ cm^{-3}$ assuming $m^* = m^*_{GaAs}$. At a comparable carrier density of $2.2 \times 10^{18}\ cm^{-3}$, the GaAs buffer layer showed $\mu_e = 3300\ cm^2/Vs$, only slightly higher than the bismide. This shows that the carrier mobility in GaAsBi films is relatively unaffected by dilute Bi incorporation. As seen in Fig. 7.3(c), the GaNAs conductivity shows a strong suppression in σ_1 at low frequencies that smoothly returns to Drude behavior above 1.56 THz. Such a reduction is consistent with the picture of localized cluster states within the conduction band, where long range transport (low frequency) is hindered by the cluster potential but transport over short distances (high frequency) is

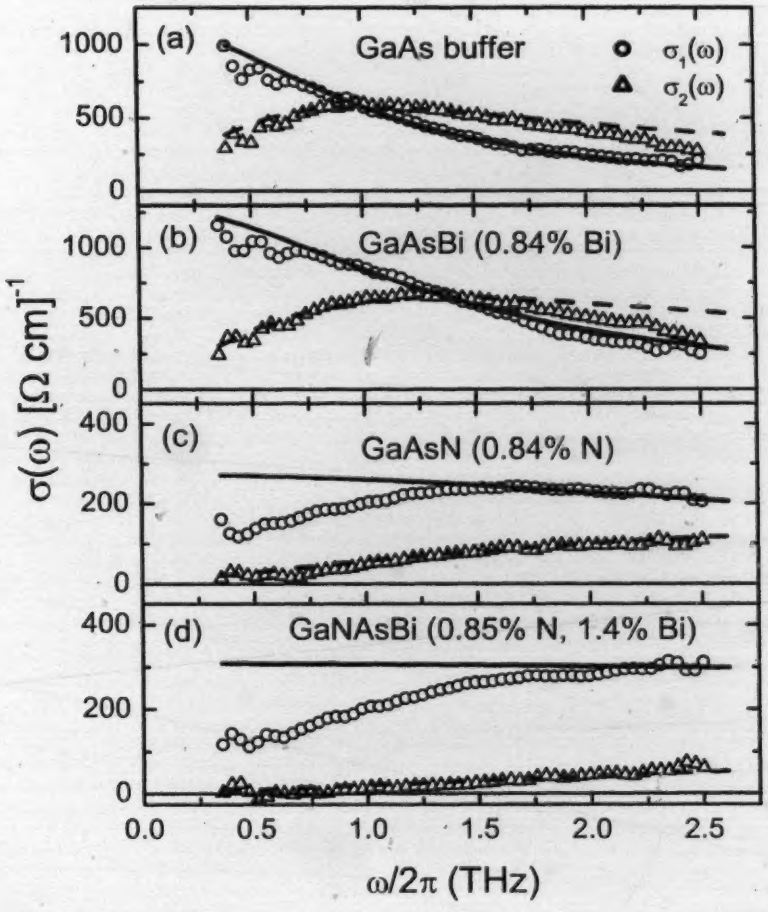

Figure 7.3: Extracted complex conductivity for a) GaAs buffer layer, b) GaAsBi (0.84% Bi) c) GaNAs (0.84% N) and d) GaNAsBi (0.85% N, 1.4% Bi) 10 ps after 400 nm excitation at a fluence of 3.7 $\mu J/cm^2$. The solid and dashed lines are fits to the real and imaginary Drude conductivity with a)$\omega_p/2\pi = 46 \pm 1$ THz , $\tau = 157 \pm 7$ fs, b) $\omega_p/2\pi = 57 \pm 1$ THz, $\tau = 115 \pm 4$ fs, c) $\omega_p/2\pi = 48 \pm 2$ THz, $\tau = 35 \pm 3$ fs, d) $\omega_p/2\pi = 86 \pm 2$ THz, $\tau = 12 \pm 1$ fs.

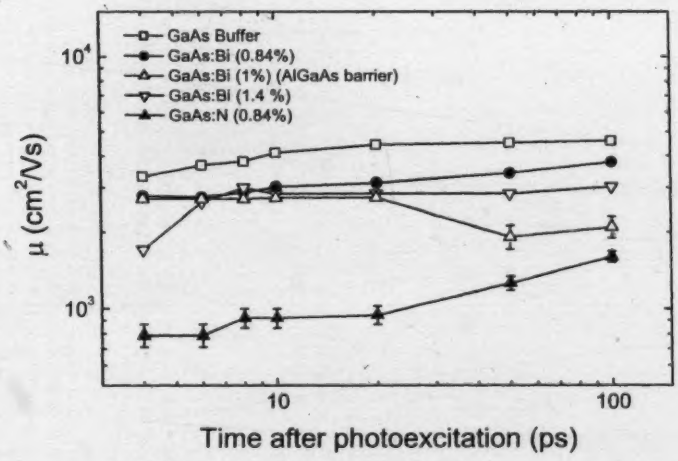

Figure 7.4: The time evolution of carrier mobilities extracted from Drude fits to complex conductivity data after 400 nm, 3.7 μJ/cm^2 excitation. The electron effective mass is assumed to be that of bulk GaAs, m*=0.067 me.

band-like. From the high frequency Drude fits assuming $m^* = m^*_{GaAs}$, the mobility is 920 cm^2/Vs at $n = 1.9 \times 10^{18}$ cm^{-3}, which is in good agreement with the intrinsic limitation on the electron mobility imposed by alloy scattering in GaN_xAs_{1-x} for x $\cong$ 0.01 and $m^* = m^*_{GaAs}$ [24].

It has been proposed that the incorporation of Bi might improve the electronic properties of GaNAs by relieving the GaAs lattice mis-match stress caused by the small N atom with the larger Bi atom [125, 126]. The appropriate concentration ratio of Bi to N to achieve lattice matching with GaAs has been reported to be 1.7 [125]. Fig. 7.3(d) shows the conductivity results for the $GaN_xAs_{1-x-y}Bi_y$ sample with y$\approx$1.7x. Like the GaNAs sample, $\sigma_1(\omega)$ is highly suppressed at lower frequencies and merges with Drude behavior at higher ω. Drude fits to the high portion of the spectra, assuming $m^* = m^*_{GaAs}$, gives a mobility of 320 cm^2/Vs, reduced from the GaNAs mobility and indicating the electronic properties are not improved by co-doping with Bi. We should note that our measurements show a

Sample	μ_e (cm^2/Vs)
GaAs buffer layer	3300±100
GaAs1 − yBi$_y$ (y = 0.84%)	2800±100
GaAs$_{1-y}$Bi$_y$ (y = 1.0%) (AlGaAs barrier)	2800±100
GaAs$_{1-y}$Bi$_y$ (y = 1.4%)	2700±100
GaNxAs$_{1-x}$ (x = 0.84%)	920±80
GaN$_x$As$_{1-x-y}$Bi$_y$ (x = 0.85%, y = 1.4%)	320±30

Table 7.1: The extracted electron mobility from Drude fits to the complex conductivity in various samples for early t = 10 ps, with a 400 nm pump fluence of 3.7 $\mu J/cm^2$. ($n \sim 2-3\times10^{18}$ cm^{-3}) †Derived from high frequency fits to the Drude model.

dc measurement ($\omega = 0$) of the mobility will be smaller than these high frequency estimates.

A possible complication in these measurements is the diffusion of carriers into the underlying high μ buffer layer. GaAsBi may have little conduction band offset with GaAs, whereas GaNAs has a significant offset which acts as a barrier to diffusion of electrons into the buffer layer. To ensure the high mobility observed in the GaAsBi was not due to electron transfer to the buffer layer, a similar film was grown on a 1.4 μm thick $Al_{0.27}Ga_{0.63}As$ barrier layer to confine carriers to the GaAsBi film. In addition to confining the electrons to the bismide film, the AlGaAs barrier layer also has a low mobility, so that any diffusion into the underlying barrier layer would be noticed by a decrease in mobility. Without the AlGaAs barrier, the extracted GaAsBi μ_e values are constant at ~2800 cm^2/Vs for $\Delta t < 10$ ps, and then slowly rise due to diffusion into the buffer region. With the AlGaAs barrier, μ_e is constant at 2800 cm^2/Vs for $\Delta t = 50$ ps, reflecting the 300 meV conduction band offset limiting diffusion into the buffer layer. This indicates the mobility values are representative of the film mobility for t < 10 ps. Finally, the higher concentration Bi sample showed the same carrier mobility as the 0.84% sample at early times, indicating that the mobility is not significantly altered by increasing Bi concentration up to 1.4 %. Table 7.1 summarizes these early time ($\Delta t = 10$ ps) mobility results for all samples investigated.

The conclusion that carriers are within the film for t < 10 ps for the GaAsBi film is further supported by calculations of the carrier distribution by solving the

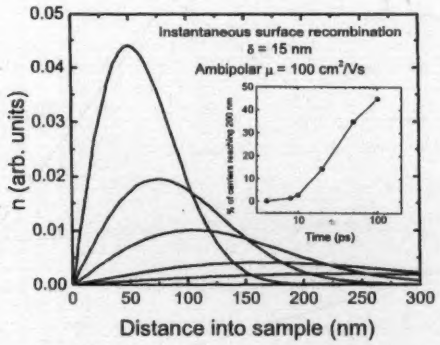

Figure 7.5: Calculated carrier density profiles 4, 10, 20, 50 and 100 ps after 400 nm pump excitation, assuming an infinite surface recombination velocity, a pump penetration depth of 15 nm and an ambipolar mobility of 100 cm^2/Vs. Inset is the percentage of carriers reaching a distance of 200 nm, i.e. to the substrate, obtained by taking the ratio of the integrated density profiles beyond 200 nm to the integration to infinity.

diffusion equation, Eq. 6.1, with infinite surface recombination, provided the *ambipolar* mobility is a realistic value of 100 cm^2/Vs, shown in Fig. 7.5, for times 4, 10, 20, 50 and 100 ps after excitation. The inset is the percentage of carriers reaching the 200 nm depth into the film, corresponding to the beginning of the substrate in our samples. This percentage is calculated by taking the ratio of the numerically integrated carrier distribution from 200 nm to infinity over the entire carrier distribution. Before 10 ps, very few carriers are present in the substrate, but by 100 ps roughly half the total population has reached the substrate.

7.3 Conclusions

In summary, we have used TRTS to characterize the carrier transport mechanisms in dilute GaAs nitride and bismide alloys. We find that the electron mobility is significantly reduced in GaNAs, with non-Drude behavior at low frequencies due to the presence of localized states in the conduction band. In GaAsBi, however,

we find Drude behavior with $\mu_e = 2800\ cm^2/Vs$ at n = $2.7 \times 10^{18}\ cm^{-3}$, which is relatively unchanged relative to GaAs with $\mu_e = 3300\ cm^2/Vs$ at $n = 2.2 \times 10^{18}$ cm^{-3}. We find no further mobility reduction for Bi concentrations up to 1.4 %, showing that the bandgap of GaAs can be reduced without significantly degrading the electron transport properties by dilute Bi alloying. Finally, the electronic properties of the quaternary alloy GaNAsBi with optimal N and Bi concentrations for GaAs lattice matching were found to be further degraded over GaNAs by incorporation of Bi, again showing strong deviation from Drude conductivity with low frequency $\sigma_1(\omega)$ suppression.

While initial findings are of significant importance to the optoelectronic community, there is much work left to be done in both the nitrides and bismides. An oustanding issue is the form of ac conductivity observed in the nitrides does not conform to any model known to us. Such a reduction in the low frequency σ_1 in the nitrides should be accompanied with a σ_2 which is negative to be Kramers-Kronig compatible. A more detailed investigation of the nitrogen concentration dependence of the conductivity, from the ultradilute (x < 0.1%) to the dilute limit explored here would be very informative. The formation of N-clusters in the GaAsN alloy has been identified as the cause of the deterioration of electronics and optical properties. Recently it has been found that a Bi wetting layer applied to the GaAs buffer layer prior to GaAsN deposition reduces the N clustering and restores the photoluminescent properties of GaAs. It would be interesting to see if this restoration of the optical properties is accompanied by an improvement in the electron mobility.

A slightly more advanced project involves the integration of a high pressure cell to apply a hydrostatic pressure of $\approx$ 10 GPa to a GaAsN sample, while monitoring the electron mobility after optical injection of electrons into both the upper and lower split conduction band. A transition from localized to extended behaviour is expected for the lower band, and vice versa for the upper band [113]. The THz pulse would be sensitive to this transition, if it exists.

Thermally activated transport has been reported in GaAsN, where electrons are thermally excited out of the localized traps into the extended states. The authors claim to see a percolative transition from hopping transport to band-like transport with increasing carrier density [127]. These results have been called into question

by a recent study reporting passivation of N clusters by Si in GaAsN, where the optical bandgap of GaAsN is restored by the addition of Si [128] because of a binding that occurs to the N clusters [128, 129]. Most of the transport studies have used donor impurities such as Si_{Ga} to n-dope their GaAsN samples. They have assumed the carrier density was equal to the donor concentration, and that the impurities were otherwise relatively inert. This mutual passivation of donor and impurity does not exist for optical injection of carriers, and a fluence dependence should be performed on the nitrides at early times to determine if this transition from hopping transport to band transport really does occur with higher carrier concentrations, or if it is merely a side-effect of the mutual passivation. We should note that a study of the carrier density effects on the electrical properties of GaAsN was performed using modulation doping, which avoids any possibility of forming Si-N complexes [116]. The authors of this study found that the electron mobility was limited by N scattering even at room temperature to ≈ 300 cm^2/Vs at 0.4% N, in fair agreement with the reduced mobilities observed in this study.

Chapter 8

Electrodynamics of nanostructures

8.1 Characteristic transport length scales

There are several characteristic length scales of a system which one must consider when investigating its electronic properties. For instance, in Mott's theory of minimum metallic conductivity, he states that for metallic behaviour to be observed, the electron's mean free path must be larger than its wavelength [130]. Percolation theories define a different characteristic length scale, one which is not constant but diverges as one approaches the metal insulator transition according to so-called universal exponents [131]. Underlying these conceptual length scales are the physical length scales of the system, such as the average particle size and interparticle spacing in an array of nanoparticles. An important question in exploring the conducting properties of nanostructured semiconductors is what is the length which one is probing and how does this relate to the defining length scales of the system.

In a dc conductivity measurement, one is probing the macroscopic electrical connectivity of the system. In a random metal-insulator composite, this connectivity depends on the volume fraction of the metallic component. There is a critical value where a conducting pathway forms spanning the sample dimensions, and so there is an accompanying large increase in the dc conductivity, referred to as the percolative transition. Tunneling or hopping conduction between localized states

can also lead to a dc conductivity, as shown recently in doped CdSe nanoparticles [132]. In an ac conductivity measurement, however, the probing length scale can be varied by changing the frequency, ω, and is given by $L_\omega = \sqrt{D/\omega}$ where D is the diffusion constant [92]. This can be thought of as the distance that a charge carrier moves within the period of one oscillation of the electric field. The assumption of diffusive motion is applicable provided mean free times are much smaller than the half period of the applied field. If the mean free time exceeds the half period of the applied field, carrier motion is ballistic. However, the distance a carrier travels through ballistic motion will still be dependent on the applied frequency of the field. A broadband ac conductivity measurement is therefore a direct probe of the characteristic length scale of a system, with lower and upper bound of probed lengths defined by the upper and lower frequency cutoffs. For a THz pulse with frequency components stretching from 0.1 - 3 THz and a typical D ~ 1 cm^2/s, charge carriers scan a distance from 2.3 - 12.6 nm. Thus if one wants to probe the effects of nanoscale size effects in typical semiconductors, the frequency regime of interest is in the THz region.

Much of the work presented here hinges on this argument, that there is a length scale over which the THz pulse can probe carrier motion. If the carrier is confined within that length scale, it cannot respond as much to the applied electric field and thus will not be strongly absorbed. For typical InGaAs mobilities of 10000 cm^2/Vs, using the Einstein relation $D = \frac{\mu k_B T}{e}$ at room temperature and for frequencies within the THz bandwidth, this range is 40 - 200 nm. If carriers are confined within this length scale, their mobility will be greatly reduced. At lower temperatures, D is larger because of the typical rate of increase of μ, and so carriers are still confined.

Below the confinement length, the current response cannot be in phase with the electric field because it observes a barrier within the time it takes for the field to oscillate. This implies a conductivity response which is dominated by its imaginary component, since the phase of the current response is $\theta_J = arctan\left(\frac{\sigma_2}{\sigma_1}\right) + \theta_E$. Since $\sigma_2 \to 0$ as $\omega \to 0$, this implies $\sigma_1 \to 0$ as well in order for the response to be out of phase with the applied field. This is a hand-waving argument as to why the real part of the conductivity must be suppressed at low frequencies if a carrier is confined, but this suppression is routinely observed in literature (for example,

see Refs. [133, 134, 135, 92]) and, as we shall see, is observed in nanocrystalline semiconductors on ultrafast time scales [74, 75, 83].

Chapter 9

Quantum wire heterostructures

In recent years there has been considerable interest in carrier capture dynamics in semiconducting quantum wire (QWR) heterostructures, aimed at understanding and improving the performance of optoelectronic and photonic devices based on these novel systems [136, 5, 137]. Much of this has been driven by considerable advances in QWR growth, including the use of high index substrates acting as ideal templates for laterally-ordered and densely packed QWR structures [138, 139]. In devices based on these structures, it is often the case that carriers are optically or electrically injected into barrier or wetting layer regions, and must then be efficiently captured into the wires. This capture process is therefore intimately tied to device performance. Many studies have been done to try to understand the relevant time scales and mechanisms, requiring sophisticated time-resolved techniques. Time-resolved photoluminescence (PL) [140], time-resolved near-field optical spectroscopy [141], and non-degenerate pump-probe [142] experiments have been used to study the capture mechanism, and have shown the capture process occurs over sub-picosecond to picosecond time scales in various quantum wire structures [142, 143, 144, 145]. PL techniques, however, are sensitive to the population of radiative QWR excitonic states and thus exciton formation and relaxation [146] may be convoluted with the bare carrier capture time. For non-resonant excitation conditions, intersubband relaxation can also be a complication for non-degenerate pump-probe experiments. Ideally, a time-resolved technique that is sensitive to low energy intra-band transitions would be preferred since it would allow for a direct observation of the capture event.

In this work we use THz probe pulses to directly monitor the picosecond capture dynamics into the wires by sensing only mobile charge carriers. We show the transfer of carriers from the barrier and wetting layer regions to the QWRs occurs within 15 - 30 ps of photoinjection in strain-induced laterally-ordered InGaAs/GaAs QWRs. The lateral confinement of carriers within the wires is responsible for a large anisotropy in the absorption of the THz probe pulse when the polarization is aligned parallel or perpendicular to the wire direction. The efficiency of the transfer process is temperature dependent, with thermal emission out of the QWRs becoming important at T > 100 K. Below 100 K, carriers are efficiently confined to the wires and only contribute to the photoconductivity along the wire direction, persisting for several hundred ps.

THz pulses are sensitive to the induced photoconductivity of a material. By monitoring the changes in THz transmission, one is effectively measuring changes in the product of the carrier density and mobility. Mobile charge carriers are able to respond to an applied THz electric field, and thus contribute to the attenuation of the THz pulse. Capture into a localized state greatly reduces the carrier mobility in the confinement direction, and therefore these carriers no longer contribute to the transient THz signal. By aligning the THz polarization parallel ($\parallel$) and perpendicular ($\perp$) to the wire direction, one can de-couple the photoconductive response of the one dimensional (1-D) wires from the two dimensional (2-D) barriers. This makes it an ideal technique for monitoring carrier capture in quantum wire semiconductor heterostructures. Time-resolved THz pulse spectroscopy has been successfully applied to measure carrier capture dynamics in microcrystalline silicon [147], InAs [77, 76], InGaAs [81], and ErAs [78] quantum dot structures. We now extend the capability of TRTS to study the capture process in semiconductor QWR structures. We further show that by subtraction of the $\parallel$ and $\perp$ response we can directly observe the bare capture process, providing new insight into carrier capture into quantum wires.

9.1 Samples

Two structures were grown by molecular beam epitaxy on GaAs(311)A substrates for this study by Greg Salamo's group at the Department of Physics, University of

Arkansas. A 500 nm GaAs buffer layer was first deposited at 600°C. The substrate temperature was then reduced to 540°C for deposition of (In,Ga)As at a constant As beam equivalent pressure of 1×10^{-5} torr. The surface reconstruction of the lattice mismatched InGaAs that then takes place depends upon the In content and the thickness of the layer. 2-D growth occurs for thicknesses up to 4 monolayers (MLs), followed by the formation of 1-D wires growing along the $[2\bar{3}\bar{3}]$ up to 10 ML, after which quantum dots form on a corrugated wetting layer [139, 148]. A 10 nm GaAs capping layer was deposited to protect the InGaAs structures.

TEM analysis was performed using a JEOL JEM-2000FX microscope operated at 200 kV. Standard mechanical and ion-milling techniques were used to prepare TEM specimens done by Matthew Johnson at the Department of Physics, University of Oklahoma. Fig. 9.1 shows TEM images of the two single layer structures used in this study, a 4 ML $In_{0.4}Ga_{0.6}As$ QW in Fig 9.1(a-c) and a 6 ML $In_{0.4}Ga_{0.6}As$ QWR structure in Fig. 9.1(d-e). The plan-view TEM image of Fig. 9.1(a) demonstrates a regular InGaAs/GaAs (311)A QW with some surface corrugation along $[2\bar{3}\bar{3}]$, about 5 nm wide and 0.4 nm high. The cross-sectional TEM (X-TEM) image in Fig. 9.1(b) and (c) shows the single quantum well (QW) layer capped by a 10 nm GaAs layer. The TEM plan-view image in Fig. 9.1(d) shows the 6 ML QWR growth along the $[2\bar{3}\bar{3}]$ direction, with an average continuous wire length of 1 μm. The average center-to-center wire separation is 35 nm. The FFT inset demonstrates the wires are primarily aligned along the $[2\bar{3}\bar{3}]$ direction. The X-TEM images in Fig. 9.1(e,f) clearly show wires of 23 nm average width and 2 nm average height. Fig. 9.2 schematically shows the sample dimensions.

9.2 Anisotropic photoconductivity

Pump-probe measurements were performed with THz polarization $\parallel$ and $\perp$ to the $[2\bar{3}\bar{3}]$ wire growth direction. Fig. 9.3 shows the normalized differential transmission $\parallel$ ($\Delta T_{\parallel}$) and $\perp$ ($\Delta T_{\perp}$) to $[2\bar{3}\bar{3}]$, for the QW and QWR samples at a pump fluence of 1 $\mu J/cm^2$ at 50 K. There is very little difference in decay dynamics for the QW, seen in Fig. 9.3(a), reflecting the 2-D character of the InGaAs QW. Captured carriers from the barriers into the QW are free to move equally in both directions. For the QWR sample, however, there is a significant change in decay dynamics

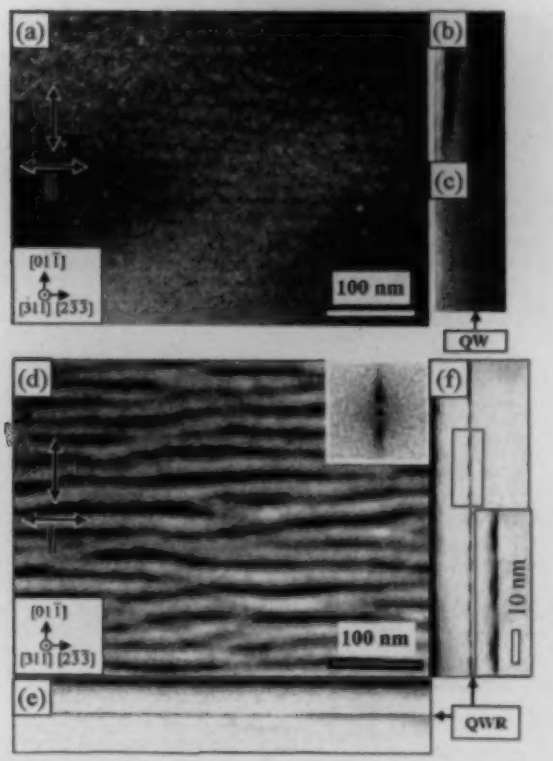

Figure 9.1: TEM images of a 4 ML InGaAs quantum well (a-c) and 6 ML quantum wire (d-f) samples. (a) Plan-view TEM ($0\bar{2}2$ dark field (DF) condition: image contrasts are strain sensitive). (b) X-TEM from the $[2\bar{3}\bar{3}]$ direction ($0\bar{2}2$ bright field (BF) condition: strain sensitive). (c) X-TEM from the $[2\bar{3}\bar{3}]$ direction ($0\bar{2}2$ quasi-kinematical BF condition: chemical sensitive). (d) Plan-view TEM (022 DF condition: strain sensitive), FFT spectrum inset. (e) X-TEM from the $[01\bar{1}]$ direction (002 BF condition: chemical sensitive). (f) X-TEM from the $[2\bar{3}\bar{3}]$ direction (622 DF condition: chemical sensitive), and enlarged image inset.

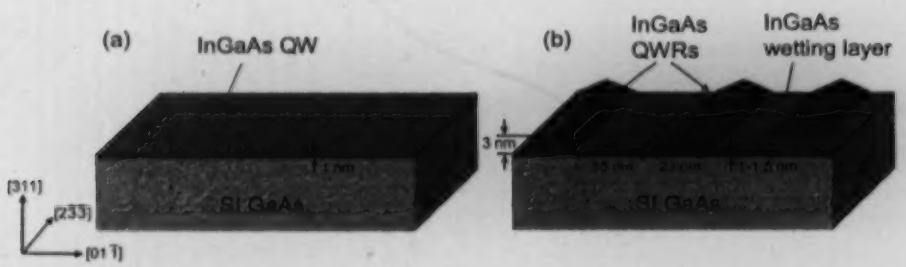

Figure 9.2: Schematic of the 4 ML quantum well (QW) and 6 ML (QWR) InGaAs structures. The capping layer has been removed for clarity.

when the wires are oriented $\perp$ or $\parallel$ to the THz polarization. Fig. 9.3(b) shows that for the same experimental conditions as the QW reference in Fig. 9.3(a), there is a photoconductive anisotropy that develops after the initial fast decay at low temperature. This anisotropy is due to carrier capture into the InGaAs QWRs where charge carriers are mobile only along the wire direction and immobile perpendicularly, contributing to $\Delta T_{\parallel}$ but not $\Delta T_{\perp}$.

9.3 Temperature dependence

Previous studies of carrier capture in QWR structures demonstrated a strong temperature dependence of the capture efficiency [140, 145, 141]. Once carriers are captured, they may be thermally excited back into the barrier regions, reducing the efficiency of devices that rely on a significant population of QWR states. To investigate the effects of thermal re-emission on the carrier capture dynamics, a temperature dependence was performed from 275 K to 10 K at pump fluences of 0.6 and 1.0 μJ/cm^2. Figure 9.4 presents the normalized -ΔT decays for both $\parallel$ and $\perp$ orientations, for temperatures from 275 - 10 K, at a pump fluence of 1.0 $\mu J/cm^2$. At high temperatures, the anisotropy is small due to captured carriers being thermally re-emitted from the QWRs into the wetting layer or barrier regions. As the temperature is lowered thermal re-emission becomes less likely and the photoconductive anisotropy increases until it is complete at $\sim$100 K. All decays

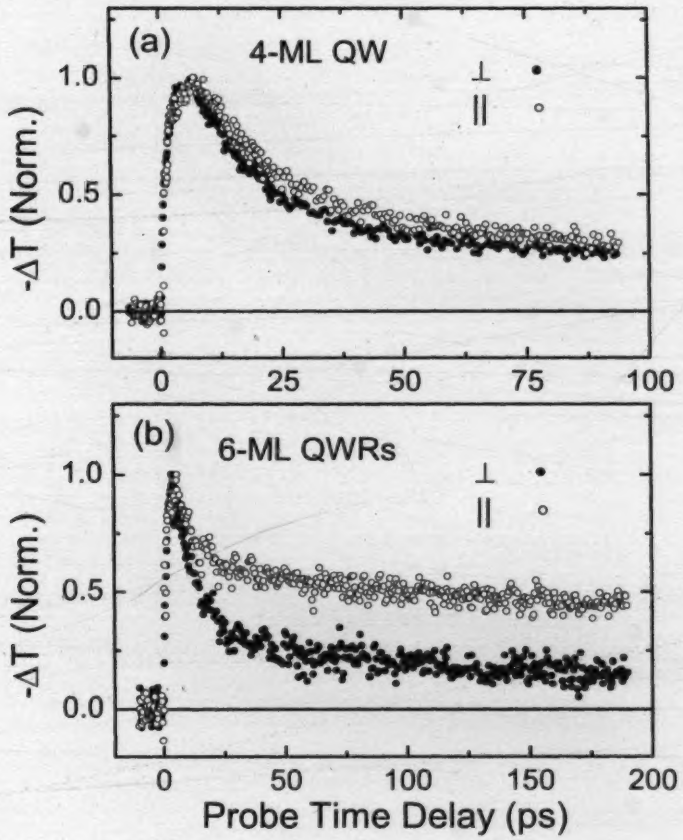

Figure 9.3: Normalized differential THz transmission for the (a) 4 ML quantum well (QW) sample and (b) the 6 ML quantum wire (QWR) sample, with THz polarization $\perp$ (•) and $\parallel$ (○) to the wire growth direction. The sample temperature was 50 K and the 400 nm pump fluence was 1.0 μJ/cm^2.

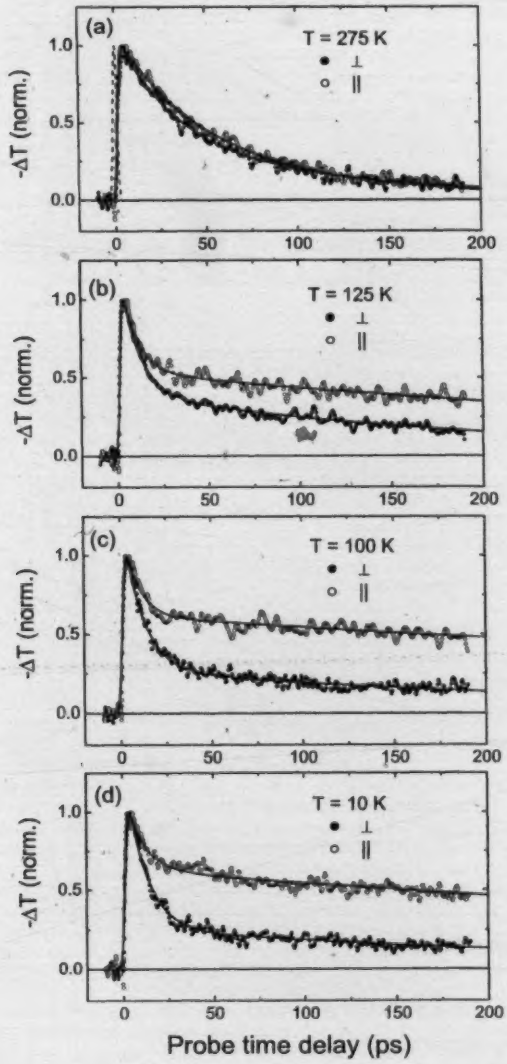

Figure 9.4: Temperature dependence of the normalized differential THz transmission -ΔT for the THz polarization $\parallel$ ($\circ$) and $\perp$ ($\bullet$) to the QWR growth direction. 400 nm pump fluence was 1.0 μJ/cm^2. Solid lines are fits to a bi-exponential decays convoluted with a Gaussian response function shown as a dotted line in (a).

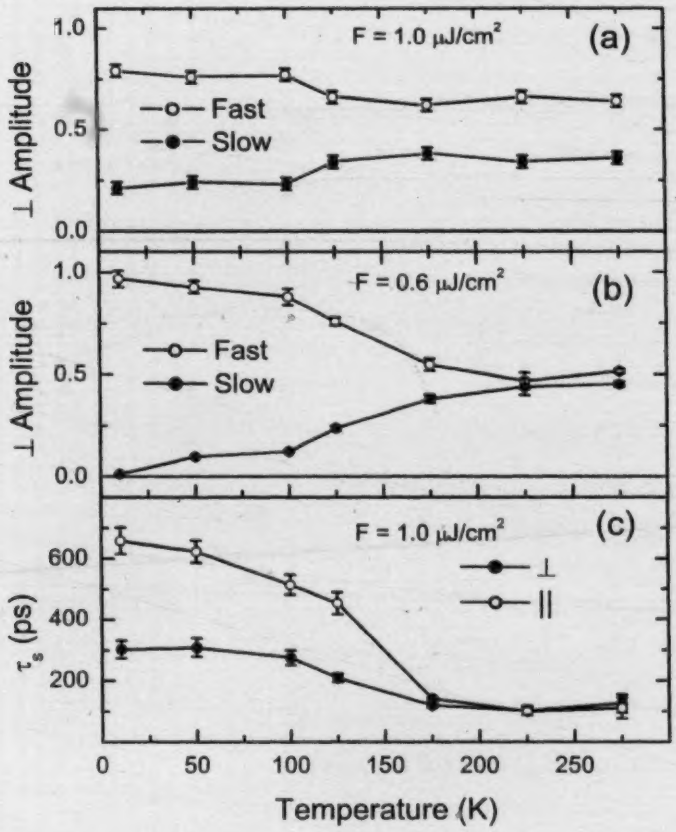

Figure 9.5: Amplitude of the fast (○) and slow (●) $\perp$ component, $A^{\perp}$, from bi-exponential fits to $-\Delta T^{\perp}$ at a pump fluence of (a) 1.0 and (b) 0.6 μJ/cm^2. (c) Temperature dependence of the slow time constant, τ_S, for both $\parallel$ (○) and $\perp$ (●) orientations at a pump fluence of 1.0 μJ/cm^2.

can be well described by a convolution of a Gaussian response function G(t) and a bi-exponential decay of the form

$$-\Delta T = G(t) \otimes \left[A_F exp\left(-\frac{t}{\tau_F}\right) + A_S exp\left(-\frac{t}{\tau_S}\right) \right] \tag{9.1}$$

where the subscripts F and S denote the fast and slow components, respectively. The amplitude of the slow component in the perpendicular direction, $A_S^{\perp}$, is proportional to the 2-D carrier density remaining within the barrier regions after the fast carrier capture and is shown in Fig. 9.5(a,b). It should be noted that $A_S^{\perp}$ does not vanish even at the lowest temperature in Fig. 9.5(a) at a pump fluence of 1.0 $\mu J/cm^2$, due to state filling in the QWRs that prevent the capture. This is similar to that seen in the capture into 1-D wetting layers in laterally aligned quantum dot-chain structures [81]. When the same temperature dependence is run at a 0.6 $\mu J/cm^2$ pump fluence, $A_S^{\perp}$ vanishes at 10K as seen in Fig. 9.5(b), indicating all the carriers are captured into the wires.

An anisotropy was also observed in the $\parallel$ and $\perp$ slow time constant, $\tau_S^{\parallel}$ and $\tau_S^{\perp}$, respectively. Figure 9.5(c) shows $\tau_S^{\parallel}$ is more than twice $\tau_S^{\perp}$ below 150 K at a pump fluence of 1.0 $\mu J/cm^2$. The decreasing trend in relaxation time with increasing temperature is an indication that the origin of the slow component is non-radiative recombination, as opposed to radiative recombination where a square root dependence with temperature is expected [149]. Below 100 K, τ_S decreases relatively slowly with increasing temperature and then rapidly but smoothly decreases above 100 K. This onset of non-radiative recombination at 100 K is consistent with radiative to non-radiative recombination crossovers observed in InAs/InP and GaAs/AlGaAs QWRs. This further strengthens the argument for a thermal escape mechanism of captured carriers, with the source of the relaxation time anisotropy being the constant replenishing of 1-D carriers (n_{1D}) from the 2-D carriers (n_{2D}) in the barriers that could not previously be captured due to state filling. This replenishing leads to a QWR photoconductivity that lasts for several hundred ps longer than the wetting layer or barrier regions.

A direct observation of the capture process can be made by subtracting out the two dimensional carrier response. With $-\Delta T^{\parallel} \propto n_{1D} + n_{2D}$ and $-\Delta T^{\perp} \propto n_{2D}$, the subtraction $-\Delta T^{\parallel} - \Delta T^{\perp} \propto n_{1D}$, allows direct observation of the capture process

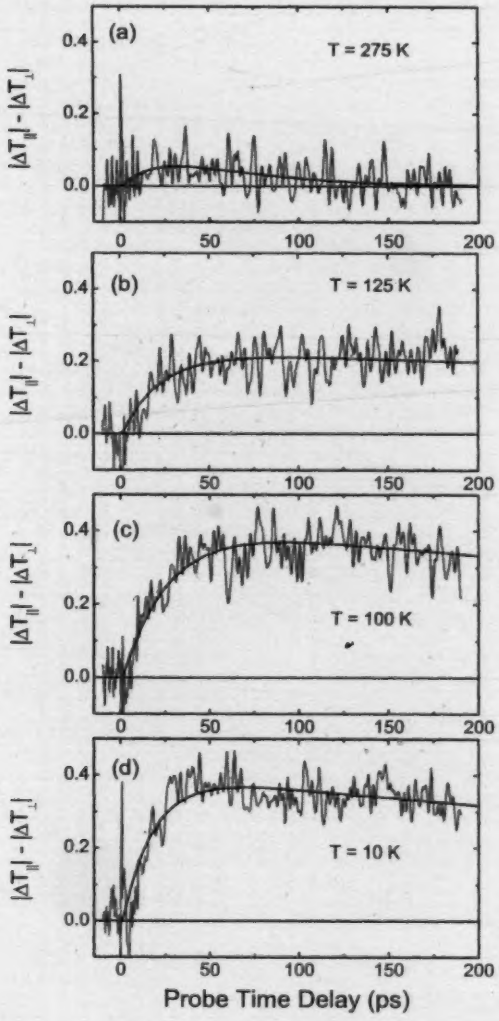

Figure 9.6: Subtraction of the parallel and perpendicular THz differential transmission decays for temperatures from 275 - 10 K (a-f) after 1.0 μJ/cm^2, 400 nm excitation. Smooth, dark lines are fits to the data using the two-level model described in the text.

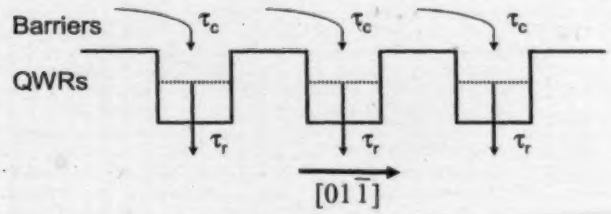

Figure 9.7: Schematic of the simple model of carrier capture described in the text.

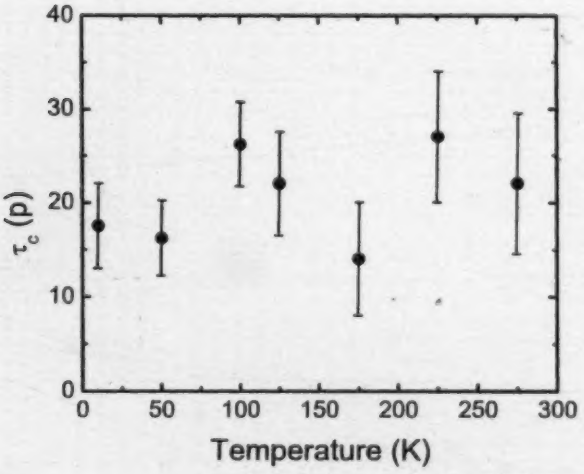

Figure 9.8: Temperature dependence of the extracted capture times, τ_c, from the fits in Fig. 9.6.

into the quantum wires. Fig. 9.6 shows the subtraction of the data sets in Fig. 9.4, demonstrating the capture process becoming more efficient with decreasing temperature from 275 down to 10 K. To understand this data quantitatively, we choose the simplest rate equation model for carrier capture, schematically shown in Fig. 9.7, where carriers are captured into the wires with a time constant,τ_c, and then recombine or become trapped with a time constant τ_r. Here we have neglected the recombination of carriers in the barriers to simplify the model, because it is on the order of 2 ns [11], much longer than the decay times observed here. The rate equations

$$\frac{dn_{2D}(t)}{dt} = \frac{-n_{2D}(t)}{\tau_c} \tag{9.2}$$

$$\frac{dn_{1D}(t)}{dt} = \frac{n_{2D}(t)}{\tau_c} - \frac{n_{1D}(t)}{\tau_r} \tag{9.3}$$

were solved, convoluted with a Gaussian response function, and fit to the data using a least squares algorithm. The resultant fits, shown as solid lines in Fig. 9.6 describe the capture event quite well considering the simplicity of the model, with relatively constant capture times from 15 - 25 ps, plotted in Fig. 9.8. This is in good agreement with previous studies reporting on carrier capture into QWRs using several different techniques [143, 144, 150, 145, 142].

9.4 Conclusions

In summary, we have shown that TRTS can be a powerful technique for monitoring carrier capture dynamics in QWR structures. Transfer of injected carriers from the GaAs barriers to the InGaAs QWRs was found to occur on the 15 - 25 ps time scale. The efficiency of the capture process was found to be temperature dependent, with thermal re-emission of carriers back into the barriers vanishing at 100 K. State filling effects in the QWRs block the capture process, where 2-D carriers constantly replenish decaying 1-D carriers on the 100 ps time scale until depleted.

Chapter 10

Quantum dot-chain heterostructures

10.1 Introduction

Carrier capture and relaxation processes in self-assembled quantum dots (QDs) have been an extremely active area of research in recent years, in part due to the potential applications for tunable, efficient QD laser structures [6] and photodetectors [26]. Often, carriers are injected into the barrier or wetting layers (WLs) and must be captured into the QD active region. Once a carrier is captured into a QD excited state, it relaxes to the ground state through a discrete set of quantized levels. The question is whether it is the capture process or the relaxation process which dominates the population of the emitting excited state after carrier injection. In 1990, it was predicted that the intersubband relaxation rate in zero dimensional QD systems would be heavily reduced because the discretization of the QD energy and momentum states lead to strict requirements for phonon emission that satisfy energy and momentum conservation [151, 152]. If two states were separated by a defined energy $E_2 - E_1 = \Delta E$ then there would only be a significant contribution to the electron-phonon scattering rate provided that the energy of the LO phonon, $\hbar\omega_{ph} = \Delta E$ [151]. This greatly reduces the probability of relaxation through a cascade of optical phonon emission. For acoustic phonons, where the wavevector $q \propto \Delta E$, the transition matrix element vanishes for q smaller than $2\pi/L_z$, so that

lower energy phonon emission is inhibited [152]. Thus the relaxation times were supposed to stretch into the nanosecond regime, longer than it takes for many non-radiative processes to occur, and so the luminescence (and the efficiency of the QD laser) should vanish. However, early ultrafast optical measurements of QD systems did not show any bottleneck. In fact, intersubband relaxation seemed to occur on a 1-10 ps time scale [153, 154, 155, 156, 157, 158]. Auger-type processes [159] and multi-phonon emission [160] have been suggested as the mechanism of this ultrafast relaxation at high and low excitation densities, respectively. It was not until 2001 before the phonon bottleneck was observed [161], and only in dots which were occupied by an electron and not a hole, otherwise the electron-hole scattering would result in a fast relaxation. In a high excitation regime where geminate injection of both an electron and a hole occurs, no such bottleneck is ever observed. To our knowledge, no other experimental work has observed a similar bottleneck, and the consensus seems to be that the bottleneck scenario is circumvented by other scattering processes. Because the intradot relaxation time to the ground state is so short, carrier capture, which also occurs over a 1-10 ps time scale, becomes just as important a parameter in influencing the operating parameters of QD devices and is of high interest to the optoelectronic community.

With the inherent sensitivity of TRTS to mobile charge carriers in semiconductor systems, it is an ideal tool with which to examine carrier capture dynamics in QD systems. Once a mobile charge carrier, injected into a barrier or wetting layer, becomes captured into a bound state within the QD, its mobility is greatly reduced and the THz pulse is no longer absorbed. Combined with the non-contact, pump-probe nature, sub-picosecond time resolution, and insensitivity to the intradot relaxation processes, TRTS is a powerful tool to unambiguously examine the carrier capture times and mechanisms. Previous studies investigating carrier capture in InAs QD systems have shown it to be very sensitive to the capture process [77, 76]. In this study, we extend this work to show that in addition to measuring bare capture times, the polarization of the THz pulse can also be used to examine any anisotropy in the system. We show in this work that a large photoconductive anisotropy exists in a novel linearly-aligned system of InGaAs/GaAs Stranski-Krastanow grown QDs, which arises from a difference in carrier capture dynamics into a two or a one-dimensional wetting layer.

10.2 Sample

Recently, a high degree of linear ordering of QDs was achieved in an $In_{0.36}Ga_{0.64}As$ /GaAs superlattice by controlling strain in the Stranski-Krastanow growth process [162, 163, 164, 165]. Researchers were able to fabricate aligned chains of QDs with an average length of 0.9 μm, as shown in Fig. 10.1(a), with dot densities of $\sim$1.8x10^{10} cm^{-2} per layer. This structure leads to very different potential profiles parallel ($\parallel$) and perpendicular ($\perp$) to the dot chains. The sample was grown on a semi-insulating (SI) GaAs [001] substrate with a 150 nm GaAs buffer layer deposited by molecular beam epitaxy at 580°C. A 15 layer structure of $In_{0.36}Ga_{0.64}As$/GaAs was then grown at 540°C, each layer containing densely packed chains of QDs with an average diameter and height of 45 nm and 5 nm, respectively. No capping layer was added. The transmission electron microscopy (TEM) plan-view image of Fig. 10.1(a) shows the dot chains running in the [$\bar{1}$10] direction. TEM images also reveal the existence of a one-dimensional (1-D WL) with an estimated height of 1.5 - 2 nm directly underneath each dot chain, all sitting on top of a 0.7 nm thick two-dimensional (2-D WL) [164, 165]. A schematic of this structure is shown in Fig. 10.1(b), and further details on growth and characterization of this sample can be found in Refs. [162, 163, 165].

10.3 Anisotropic photoconductivity

The aim of these experiments was to investigate the carrier capture process in this novel InGaAs/GaAs QD structure, where there is a strong structural and energetic anisotropy. The THz polarization is used to probe the photoconductivity along and across the dot chains by aligning the electric field vector $\parallel$ and $\perp$ to the [$\bar{1}$10] direction, respectively. Carriers were injected by 400 nm excitation from second harmonic generation of the 800 nm fundamental in a BBO crystal. This was so carriers were injected only into the QD superlattice and not into the underlying GaAs buffer layer and substrate. Note that the superlattice thickness was 287 nm, much greater than the penetration depth at λ = 400 nm, δ_{400nm} = 15 nm [89]. The sample was mounted on a 1 mm aperture inside an Oxford sample-in-vapour liquid He cryostat with fused silica front windows and polypropylene windows at

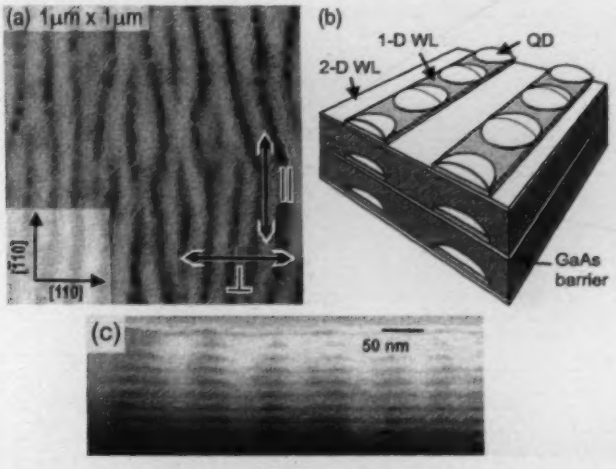

Figure 10.1: (a) TEM image of QD sample surface morphology. THz polarization parallel (‖) and perpendicular (⊥) to the dot chains is indicated. (b) Schematic diagram of the sample (not to scale) showing arrangement of QDs on 1D WLs. (c) Cross-sectional TEM image of the sample showing the vertical ordering of the dots.

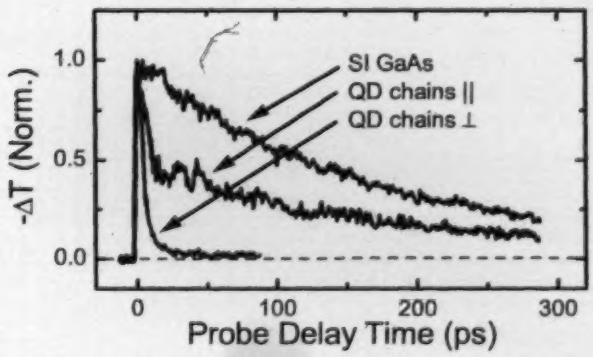

Figure 10.2: Normalized differential THz transmission, -$\Delta T(t)$, at 10 K for the THz polarization ⊥ and ‖ to the dot chains. The sample was excited with 400 m pump pulses with a fluence of 1.2 $\mu J/cm^2$. The transient response from SI GaAs is shown for comparison.

the exit port, to facilitate THz transmission. The pump beam was focused to a 1.5 mm diameter spot at the sample, illuminating the entire aperture uniformly. No phase shift was observed in the THz pulse lasting longer than 3 ps after initial excitation, which allows for the carrier decay dynamics to be described by the peak differential THz transmission, $-\Delta T/T_0$.

Being a pump-probe technique, an optical pump pulse excites carriers within the sample. By comparing the pump penetration depth (15 nm) to the dot chain layer separation (20 nm), it is clear that the carriers are injected primarily into the first few GaAs barriers. The subsequent carrier capture dynamics into the 2D WL, 1D WL, and QD states depend on temperature and excitation fluence. The advantage of the TRTS technique is that the THz-pulse polarization couples into these states differently [79, 166]. When the polarization is $\perp$ to the dot chains, THz absorption is due only to mobile carriers in the barriers and 2D WLs, but not carriers confined to the 1D WLs or QDs. In the $\parallel$ configuration, absorption is due to mobile carriers in the barriers, 2D WL and 1D WL, but not from carriers localized in the QDs. In this way, TRTS allows one to separate carrier dynamics occurring in different levels of confinement.

Figure 10.2 shows the results for THz polarization $\perp$ and $\parallel$ to the dot chains, taken at 10 K. The fluence and excitation density are 1.2 $\mu J/cm^2$ and 1.3x10^{12} cm^{-2}, respectively, so the dot states are expected to be saturated. Very different decay dynamics are apparent in the fast decaying dot sample compared to the slower bulk GaAs sample, indicating fast carrier capture into the QDs [77, 76]. Furthermore, a remarkable difference in the decay dynamics is apparent between the $\perp$ and $\parallel$ orientations. We attribute this anisotropy to rapid and efficient carrier capture occurring from the barriers or 2-D WLs to the dot chains into the dots and 1-D WLs, resulting in a fast ($\sim$5 ps) single exponential decay. The $\parallel$ scan shows a two-component decay with a fast decay comparable to that in the $\perp$ scan and a slower component with a decay of about 170 ps. The fast $\parallel$ decay is likely connected with the 1-D WL to QD capture process, while the slower decay is attributed to recombination in the 1-D WL from carriers which cannot scatter into the dots due to state filling. This fast QD capture [77, 76] and slow WL recombination [77] is similar to what is seen in other TRTS experiments of QD samples. Furthermore, another study investigating linear arrays of InAs QDs grown on [001] GaAs also

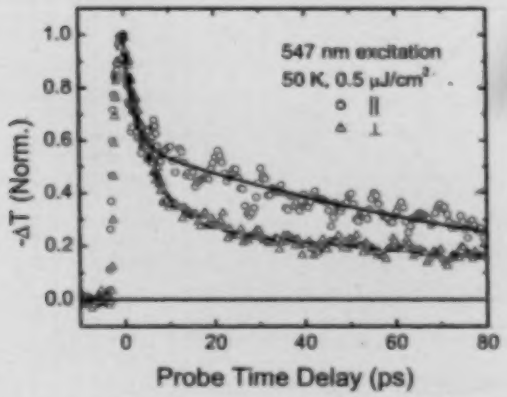

Figure 10.3: Negative differential THz transmission $-\Delta T/T_0$ scans of the QD chain sample with the THz pulse polarization aligned $\parallel$ and $\perp$ to the wire direction, taken at 50 K. The pump wavelength was 547 nm at a fluence of 0.5 $\mu J/cm^2$.

revealed a mobility and transport lifetime anisotropy between the $[\bar{1}10]$ growth direction and the $\perp$ [110] direction [167].

To ensure that the fast photoconductive decay and anisotropy was not due to any surface recombination effects, the experiments were repeated with 547 nm excitation wavelength from the sum frequency output of a travelling wave optical parameteric amplifier system (TOPAS). The penetration depth of 547 nm light in GaAs is deeper into the superlattice ($\delta = 134$ nm [89]), and farther away from the sample surface. Figure 10.3 shows an example of the $-\Delta T/T_0$ data, taken at a pump fluence of $\approx 0.5\ \mu J/cm^2$ and a temperature of 50 K. Again a fast photoconductive decay was observed, as well as an anistropy in the decay dynamics between the two $\parallel$ and $\perp$ orientations. We therefore conclude that surface recombination effects were not significant. It should however be noted that the slow component did not disappear even at the lowest temperature (10 K), and we interpret this as diffusion into the underlying GaAs buffer and substrate.

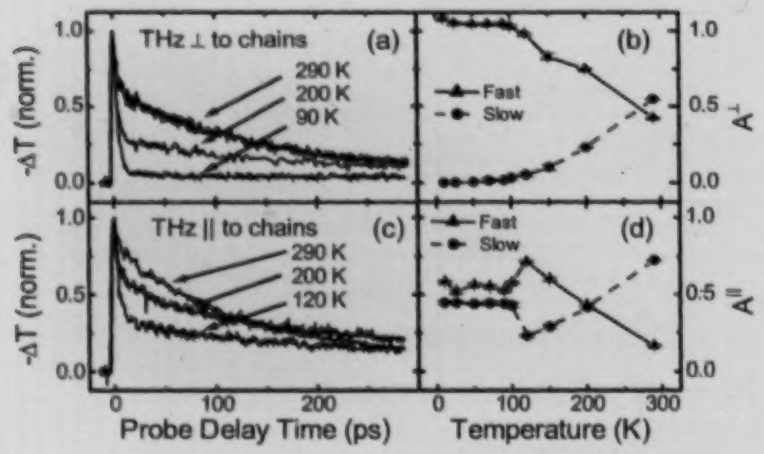

Figure 10.4: (a) Normalized -Δ T for the THz polarization ⊥ to the dot chains at three different temperatures, and (b) amplitudes of the fast and slow components. (c) Normalized -Δ T for the || orientation at three temperatures, and (d) corresponding component amplitudes. The pump fluence was held at 1.2 μ J/cm^2 for all temperatures.

10.4 Temperature dependence

We examine this anisotropic photoconductive response as a function of temperature to investigate the role of thermionic emission out of the localized states. The incident 400 nm pump fluence was held fixed at 1.2 $\mu J/cm^2$ while the temperature was lowered from 290 to 10 K. The temperature dependence of the -ΔT scans for the ⊥ geometry is given in Fig. 10.4(a), normalized to unity. The ⊥ orientation has a two-component decay for T > 90 K, but the slow component vanishes for T < 90 K. This indicates that thermionic emission out of the 1-D WL and dots to the 2 D WL is negligible for T < 90 K, in agreement with previous studies of thermal carrier escape out of other QD systems [162, 168, 169, 170, 171].

Biexponential fits of the form $-\Delta T = A_F exp(-t/\tau_F) + A_S exp(-t/\tau_S) + A_{DC}$ were found to describe the data quite well for all temperatures and fluences, where

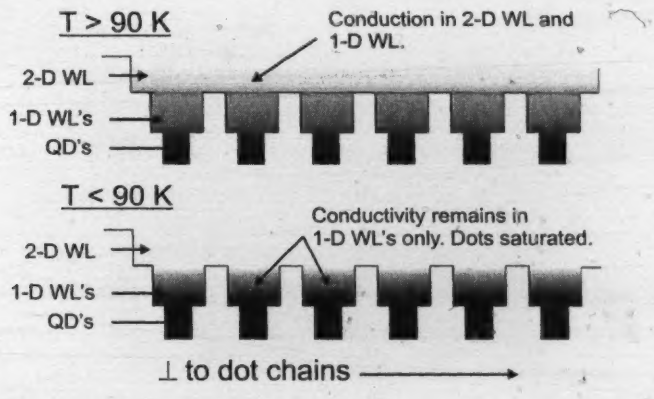

Figure 10.5: Schematic of the thermal re-emission process with shading representing the carrier population.

the subscripts F and S denote fast and slow components, respectively. A small static component, A_{DC}, was included to account for recombination effects occurring over long time scales, such as bulk recombination in the GaAs barriers. The result from the fits for $A_S^{\perp}$ and $A_F^{\perp}$ are shown in Fig. 3(b). Lowering the temperature, $A_S^{\perp}$ makes a smooth transition to zero as thermionic emission decreases and carriers are permanently captured into the 1-D WL and dots, while $A_F^{\perp}$ rises to dominate below 90 K. The rise of this fast component is very much like the rise of integrated photoluminescence intensity with decreasing temperature, linking the fast amplitude to the carriers captured by the dots, which then recombine radiatively.

The temperature dependence of the $\parallel$ scans is given in Fig. 10.4(c) for T$\geq$ 120 K. Lowering the temperature from 290 K, $A_S^{\parallel}$ initially decreases as thermal emission out of the QDs into the 1-D and 2-D WLs decreases. For T $<$ 120 K, however, $A_S^{\parallel}$ does not vanish like $A_S^{\perp}$. Instead, it increases to a constant value which is temperature independent, as shown in the fitting results of Fig. 10.4(d). At $\sim$ 100 K, carrier capture from the 2-D WL into the 1-D WL and dots for carriers traveling $\perp$ to the chains becomes efficient as thermionic emission is negligible. This increases the carrier density in the 1-D WL, resulting in an increase of the

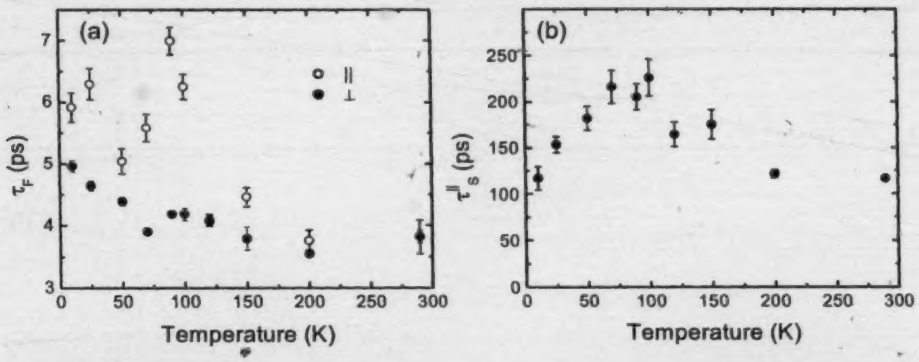

Figure 10.6: (a) Temperature dependence of τ_F, the fast exponential decay time from biexponential fits to the -$\Delta T/T_0$ in both orientations to the QD chains. (b) Temperature dependence of the τ_S, the slow exponential decay time. The pump fluence was $1.2 \mu J/cm^2$.

slow $\parallel$ component. As the dot states are filled and thermal escape to the 2-D WL is no longer possible, the density of carriers in the 1-D WL is temperature independent for T < 90 K. A schematic of this thermal reemission process and how it affects 1 and 2-D conduction is given in Fig. 10.5.

Fig. 10.6 shows the (a) fast (τ_F) and (b) slow (τ_S) time constants from the biexponential fits to the -ΔT scans from 300 - 10 K. Both the $\perp$ and $\parallel$ fast capture times into the dots and 1-D WLs shown in Fig. 10.6(a) show an increasing trend with decreasing temperature, indicating that phonon scattering may play a role in the capture process. Also, the $\parallel$ capture time is greater than the $\perp$ τ_F at lower temperature, in agreement with the model of capture into the 1-D WL followed by capture into the QDs. The slow time constant (τ_S) in Fig. 10.6 showed a broad peak at $\approx$ 70 K, that could be related to diffusion to non-radiative recombination centers. As the temperature is lowered, initially the diffusion constant increases because of an increasing carrier mobility. However, once the mobility has reached its maximum when optical phonon scattering has vanished, it decreases or remains constant, and so the diffusion constant decreases.

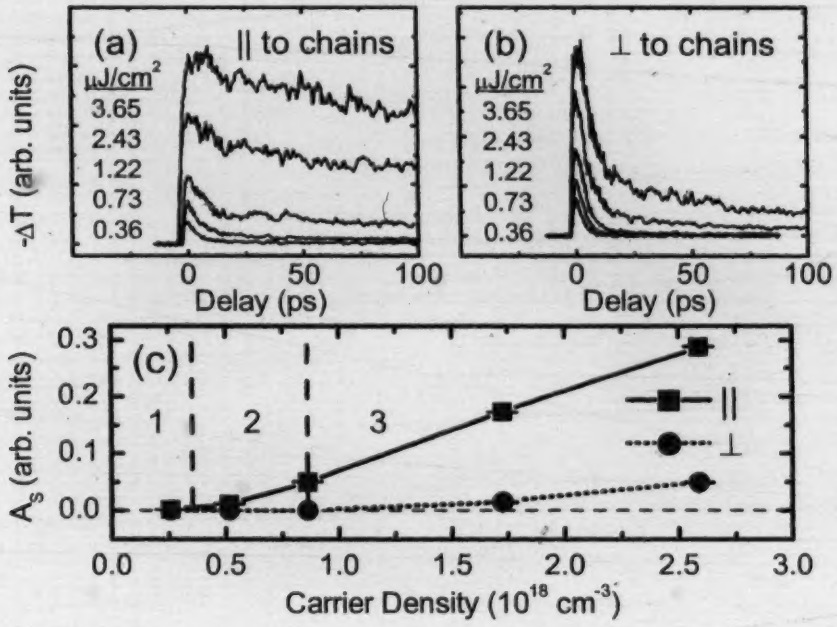

Figure 10.7: -ΔT scans for the (a) || and (b) ⊥ orientations at 10 K for the fluences listed. (c) Dependence of the amplitude of the slow component with photoexcited carrier density for each polarization orientation at 10 K.

10.5 Fluence dependence

Finally, to explore the effects of state filling, a fluence dependence was performed at 10 K to minimize thermal escape mechanisms. Turning first to the || data in Fig. 10.7(a), we see that the lowest fluence wave form decays as a single exponential due to the reduction of state filling in the dots. Increasing the excitation density drives the slower component up as the dot states are filled and the 1-D WL states become occupied. At the highest excitation fluence, the 2-D WLs and barriers become populated and the slow component dominates. However, the ⊥ orientation requires a higher fluence to observe the onset of a slow component compared to the

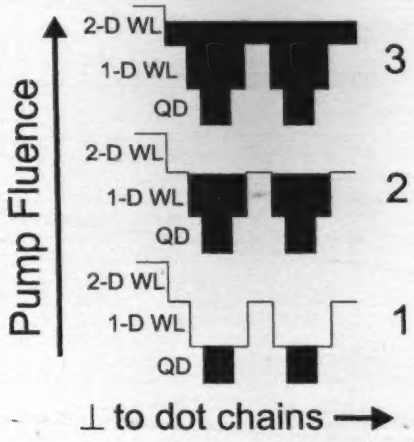

Figure 10.8: Schematic explaining the occupancy of the QDs, 1-D WLs and 2-D WLs with increasing fluence labeled with corresponding regions in Fig. 10.7(c).

$\parallel$ orientation, as shown in the -ΔT scans of Fig. 10.7(b) and the fitted A_S values in Fig. 10.7(c). This is to be expected as only the dot states must be saturated for the THz to sense a $\parallel$ slow component, whereas the $\perp$ slow component will appear only when both the dot and the 1-D WL states have been filled and the 2-D WL becomes populated. Furthermore, 15 layers of dots, with dot density of 1.8×10^{10} cm^{-2} per layer, corresponds to an effective QD state density of 2.7×10^{11} cm^{-2}, assuming one state per dot. The slow $\parallel$ amplitude vanishes at a carrier density of $\approx 2.5 \times 10^{17}$ cm^{-3}, corresponding to a sheet carrier density of 3.7×10^{11} cm^{-2}, in fair agreement with the effective state density. This supports our conclusion that state filling prevents capture into the QDs from the 1-D WLs.

10.6 Conclusions

In summary, it has been demonstrated that the polarization of the THz probe pulse in TRTS experiments can be used to investigate direction-dependent carrier dynamics in linearly organized QD structures. A large photoconductive anisotropy was seen $\parallel$ and $\perp$ to a densely packed dot chain sample, where the dots and 1D

WL serve as fast and efficient carrier traps in the $\perp$ transport direction. Thermal emission out of the dots and 1D WL to the 2D WL was found to dominate the photoconductivity for T > 90 K, while state filling effects dominated below 90 K. Future directions for this research are to selectively excite carriers into dot and wire states, and observe the reverse capture process where carriers are excited back into the barrier states. Also, because these experiments were performed in a regime where the QD states were saturated, they were only sensitive to the population of the 1-D WL. Below the saturation threshold, where THz absorption is being pushed towards detection limits, the sensitivity of the THz pulse to the capture process could in principle make significant contributions to the knowledge of carrier capture mechanisms (such as Auger, multi-phonon, etc.) in QDs.

Chapter 11

Silicon nanocrystals embedded in SiO_2

11.1 Introduction

Silicon nanocrystals (Si-NCs) have been extensively studied over the past decade, motivated primarily by the possibility of integrating their tunable luminescent properties into future photonic devices [28, 172, 173]. Despite this intense research effort, relatively few studies have explored carrier dynamics in silicon nanocrystals on picosecond time scales immediately following optical injection [174, 36, 175]. The behaviour of charge carriers in semiconductor nanocrystal thin films depends strongly on the structural details. Characteristic length scales such as the crystal size and interparticle spacing determine the transport properties. Transport over macroscopic length scales is dependent on percolation paths spanning the sample dimensions, which may occur provided the nanocrystals are in electrical contact or in close proximity to one another, opening the possibility of hopping or tunneling between localized states. Steady-state (low-frequency) conductivity measurements probe this macroscopic connectivity, and recent temperature and field-dependent studies have reported variable range hopping to be important in doped CdSe nanoparticle arrays [132]. High-frequency measurements, however, can probe conductivity over shorter length scales given by $L_\omega = \sqrt{D/\omega}$, where D is the diffusion coefficient and ω is the probing frequency [92]. Heuristically,

this can be thought of as the distance a carrier diffuses before the field reverses direction. In the nanometer length-scale range (L_ω= 2 - 10 nm) and for typical diffusion coefficients (D~1 cm^2/s), the corresponding frequency is in the terahertz (THz) region (0.2 - 4 THz). Thus, by examining the response of an electromagnetic field in the THz frequency range, one can directly observe the influence of nm-scale disorder on carrier motion.

Whereas Drude-like behaviour is typically seen for the THz conductivity of photoexcited carriers in bulk single crystal samples [11, 70, 9], non-Drude behaviour and carrier localization resulting in a suppression of the real conductivity at lower frequencies have been reported in InP and TiO_2 nanocrystals [75, 74], which was shown to be consistent with the Drude-Smith model [93], presented in Section 5.3. In another study of ion-implanted Si-NCs (3 - 4 nm) in SiO_2, the THz conductivity of the photoexcited carriers was modeled as Lorentz oscillators in a background dielectric [36]. However, no dynamics were reported, the nanocluster size dependence or separation was not explored, and the S/N was limited by low pump powers from the laser source. Furthermore, the authors chose an effective medium theory with both Drude and Lorentz terms, giving a total of six floating variables in the fitting procedure. More recently, a plasmon resonance model (similar to the Lorentz model) was used to describe the THz conductivity in photoexcited micron-sized silicon particles embedded in a polymer matrix [176].

In this study, we report both the ultrafast dynamics and frequency-dependent complex THz conductivity of photoexcited silicon films with varying degrees of structural disorder ranging from bulk-Si to Si-NCs in glass. We observe a clear transition in the transient THz conductivity from a Drude-like, free-carrier response in bulk Si to non-Drude, localized behaviour in the Si-NC samples, and we find that this transition from free to localized behaviour can be described quite well within the framework of the Drude-Smith model. In particular, the real component of the THz conductivity for the Si-NCs is suppressed at low frequencies due to carrier localization, but is non-zero as $\omega \rightarrow 0$ (DC), indicative of long-range transport between nanocrystals. Finally, we find that the ultrafast carrier relaxation dynamics for times greater than 1 ps are dominated by Si/SiO_2 interface trap states and depend on the size of the nanoclusters.

We further study SiO_x films with varying x, from poly-nc silicon at x = 0

to x = 1.2, where the Si content is below the predicted percolative transition, and at annealing temperatures below, at, and above the reported crystallization temperature. The inter-grain connectivity is reflected in the THz electrodynamics by a sharp reduction in peak photoconductivity at x=1.0. The transient complex conductivity is still very well described by the Drude-Smith model at all points through this transition. The lifetime of the photoconductivity is very dependent upon the anneal temperature, and therefore the size and crystallinity of the Si nanoclusters, but relatively independent of the Si content of the films. This is an excellent indication that the THz electrodynamics are dominated by length scales much smaller than the macroscopic scale of inter-grain connectivity.

11.2 SiO_x (x = 1) Samples

The first set of Si-NC samples were formed by annealing of SiO_x films with x = 1. This system offers easily tunable crystallite size and density simply by changing the anneal temperature [172, 173, 177, 178]. For this work, a 1 μm-thick SiO film was deposited by thermal evaporation on a 1-mm-thick fused silica substrate. All SiO_x samples were grown by Dr. Al Meldrum's group at the Department of Physics, University of Alberta. The wafer was then divided and annealed for 1 hour under ~1 atm of 5% H_2 + 95% N_2 at anneal temperatures (T_a) from 500 - 1100°C. Annealing results in a phase segregation process according to the equation $2SiO \rightarrow Si + SiO_2$, producing densely packed Si nanoclusters embedded in an insulating SiO_2 matrix [177, 178]. The size and crystallinity of these particles are dependent on T_a, with evidence of amorphous clusters present at lower T_a in the range from 500 to 800°C and crystalline clusters for $T_a \geq 900$°C [178]. This phase segregation process was verified with energy filtered transmission electron microscopy (EFTEM) by the group of Quan Li at the Department of Physics, Chinese University of Hong Kong, as shown in Figs. 11.1(a)-(c), and high resolution TEM (HRTEM), as seen in Figs. 11.1(d)-(f), for T_a = 900, 1000, and 1100°C. A ripening process occurs with increasing T_a, showing nanocrystals with diameters of ~3 nm at 900°C, ~4 nm at 1000°C, and ~7 nm at 1100°C. Assuming complete phase segregation [179], nanoparticle densities are estimated as 21.0, 9.1 and 1.7 ($\times 10^{18}$) cm^{-3} for the T_a = 900, 1000 and 1100°C films, respectively. This gives an

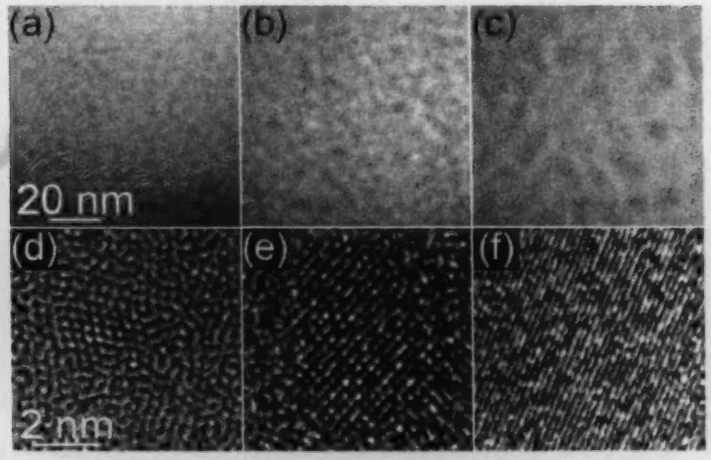

Figure 11.1: EFTEM (a-c) and HRTEM (d-f) images of the T_a=900°C (a,d), 1000°C (b,e) and 1100°C (d,f) silicon nanocrystal samples.

interparticle (surface-to-surface) spacing that increases with T_a of 0.7, 0.9 and 1.4 nm for the T_a = 900, 1000 and 1100°C films, respectively. A 200-nm-thick Si film was also grown on a 1.0-mm-thick fused silica substrate by e-beam evaporation and annealed under the same conditions at 900°C, forming a poly-nanocrystalline silicon (poly-nc-Si) film with 15 - 25 nm domain sizes, seen in the bright-field TEM image in Fig. 11.2. Finally, a bulk-like, 200-nm-thick epitaxial silicon film on a sapphire substrate (silicon-on-sapphire, or SOS) was also studied for comparison to the nanocrystalline silicon samples.

11.3 Pump absorption

In order to determine the extent of excitation, static absorption studies were performed on the 1 μm thick T_a = 900, 1000 and 1100°C using a broadband deuterium, fiber-coupled source and an Ocean Optics spectrometer with a detector range from 350 - 1100 nm. A reference 1.0 mm thick fused silica substrate with no film was used to establish a transmitted light baseline. Both reference and samples were

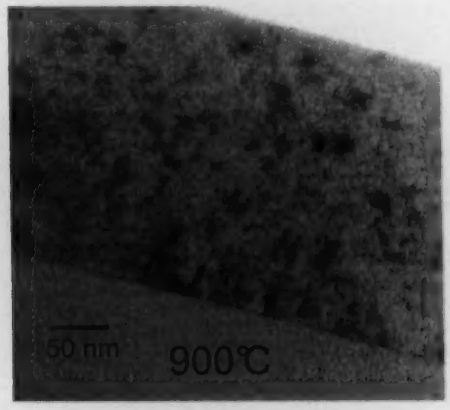

Figure 11.2: Bright-field TEM image of the 200 nm thick poly-nc-Si film. The dark spots correspond to the silicon grain boundaries that have a crystalline axes aligned to diffract into the image plane.

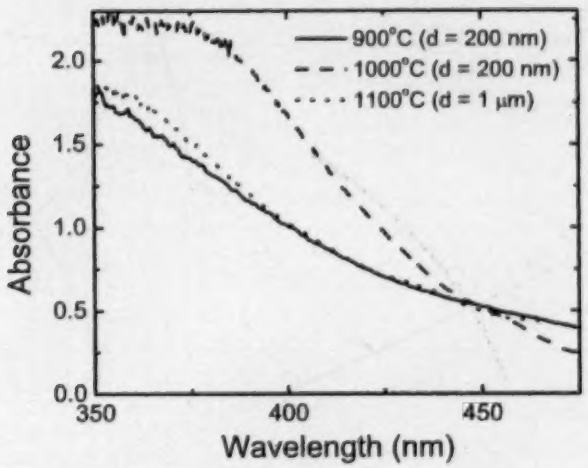

Figure 11.3: Measured absorbance of Si-NC films annealed at three temperatures. The 900 and 1000°C films were 200 nm thick and the 1100°C film was 1 μm thick.

placed on a thin microscope glass slide, at normal incidence to the lamp source fiber and the fiber-coupled detector, with the film side facing the lamp source fiber. This allowed easy and repeatable exchange of the reference and samples. The absorption spectra were accumulated and averaged over 20 minutes for each reference/sample pair. Because the films used in this study were so thick, the absorbance of the 900 and 1000°C films were beyond the sensitivity of the spectrometer. Only the 1100°C film absorbance could be accurately determined to be 1.03, corresponding to a 400 nm pump penetration depth $\delta_{400nm} = 420$ nm. To estimate δ_{400nm} for the 900 and 1000°C films, it was necessary to use 200 nm thick films grown under the same conditions as the 1 micron thick samples. The penetration depths were 87 and 185 nm for the 900 and 1000°C films, respectively, and were in good agreement with quick transmission measurements of the 400 nm pump pulse. These values were used to estimate the thickness of the photoexcited film layers when extracting the complex conductivity using Eq. 4.8.

11.4 Carrier dynamics

11.4.1 Dispersive transport

In systems where there is an inherent disorder, either structurally or in the electronic states, there is often an observed deviation from typical diffusive transport. This deviation is a manifestation of scale invariance, introduced by disorder. By scale invariance, we mean a problem which has no characteristic scale. In diffusive transport, say in a time-of-flight experiment where the carrier distribution is produced near one electrode, the spatial distribution of carriers between the electrodes can be well approximated by a Gaussian distribution. As the distribution responds to the applied field between the electrodes, moving from one side to the other, it maintains a Gaussian profile with a defined mean value, but a time-varying width. If, however, there is a trapping event between the electrodes that holds a carrier in place for some extended period of time before releasing it again, the distribution smears (or disperses) across the gap, and no longer has a defined mean. It is systems that have this behaviour, where there is a finite probability for a transport event to take a very long time to occur, that exhibit scale invariance [180].

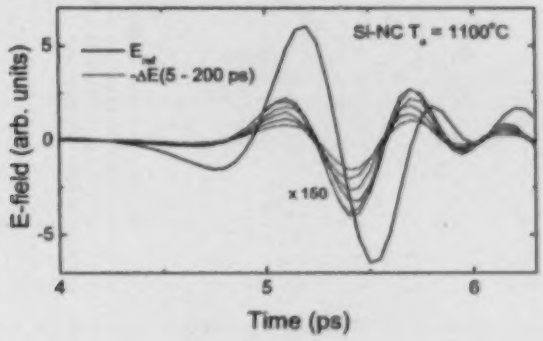

Figure 11.4: Pump-induced change in THz pulse transmission for several pump-probe delay times between 5 and 200 ps, demonstrating that although there was a considerable phase shift, this shift was constant for all delay times measured.

When examining the photoconductive decay of a system, the question of interest is often: "What is the characteristic time?". In a disordered system, there may not be such a well-defined number, and in these systems the transport is called *dispersive*. Dispersive transport has been observed in many disordered systems, including hydrogenated amorphous silicon [181], CdSe quantum dots [182], and organic systems such as polyvinylcarbazole [183], polyacetylene [184], C_{60} thin films [185], and PPV [186]. Power law ($\sim t^{\alpha}$) and stretched exponential ($\sim exp[-(t/\tau)^{\beta}]$) decay functions are signatures of dispersive transport. There are many models ranging from hopping on a geometrically disordered lattice [187], activated hopping at a mobility edge (energy which separates localized from extended band states) [181, 188], and random walks on a fractal lattice [189] that predict dispersive transport.

11.4.2 Photoconductive decay

The pump-induced change in the THz pulse was found to have a significant phase shift, as seen in Fig.11.4. However, this phase shift was constant with respect to pump-probe delay times between 5 and 200 ps. Because the change in the THz

pulse does not undergo any radical shifts in time, monitoring one time delay is representative of the transient absorption signal, and thus is a good indication of carrier decay dynamics. We note also that the phase shift is in the opposite direction as one would expect from a Drude conducting material (see Fig. 4.4). This will have important consequences later. Figure 11.5 shows the negative differential transmission ($-\Delta T/T_0$) of the THz probe pulse in the Si-NC films annealed from 500 - 1100°C and the SOS sample. A significant increase in the photoconductive lifetime is observed with increasing anneal temperature in the Si-NC samples, ranging from a resolution-limited response for $T_a < 700$°C to a few hundred ps at 1100°C, which is still shorter than the decay time seen in the bulk-like SOS film. The SOS film showed a bi-exponential decay with fast and slow time constants of 20 and 380 ps, respectively.

Fig. 11.6 shows this same data for longer times, on a log-log plot. We see a transition from a power-law decay of $t^{-\alpha}$ with $\alpha = 0.48 \pm 0.02$ for the $T_a = 800$°C Si-NC sample to a stretched exponential decay at anneal temperatures of 1000 and 1100°C of the form $-\Delta T/T_0 \propto exp[-(\Delta t/\tau_K)^{\beta}]$ with a small constant offset, which is always less than 5% of the peak value. The fitting parameters are $\tau_K = 9.2 \pm 0.7$ ps (217 ± 6 ps) and $\beta = 0.35 \pm 0.01$ (0.53 ± 0.02) for the 1000°C (1100°C) films. For the 900°C Si-NC film, a small signal-to-noise ratio prohibits definitive analysis of the decay dynamics and so both forms are shown in Fig. 11.6 for comparison. It is likely that the change in dynamics from power-law to stretched exponential at this anneal temperature is related to the amorphous-to-crystalline transition observed in the Si-NC samples for $T_a > 900$°C, as discussed earlier. A stretched exponential decay can arise from a distribution of relaxation times and has been observed in time-resolved photoluminescence studies of Si-NCs over microsecond time scales [190], including our own samples. Fig. 11.7 shows the form of decay is unambiguously a stretched exponential, with the $T_a = 1000$ °C $-\Delta T(t)$ data plotted on a log-lin, a log-log and a log(-Ln(-$\Delta T(t)$))-log(t) plot. The last form is the best graphical way to verify that a decay is a stretched exponential, with the slope of the line equal to the stretching parameter, β. The linear form on Fig. 11.7(c) demonstrates the decay is indeed a stretched exponential with $\beta \approx 1/3$.

The relaxation dynamics were independent of excitation density (pump fluence). This rules out nonlinear recombination processes like Auger recombination,

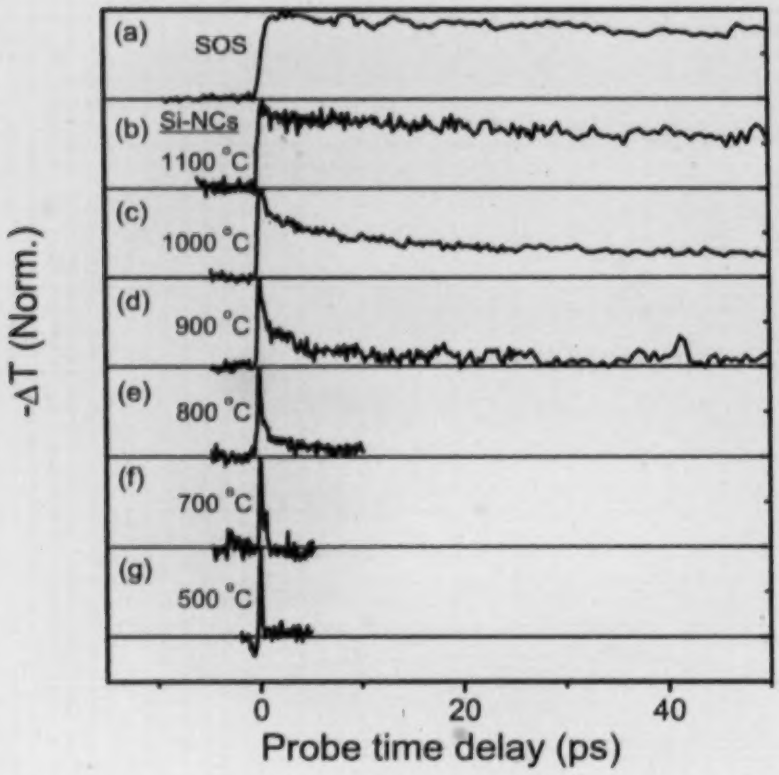

Figure 11.5: Differential THz transmission dynamics, $-\Delta T/T_0$, due to 400 nm excitation for (a) an epitaxial silicon-on-sapphire (SOS) film at a pump fluence of F=30 $\mu J/cm^2$, and (b)(g) Si-NC films (T_a=1100-500°C) at a pump fluence of F=315 $\mu J/cm^2$.

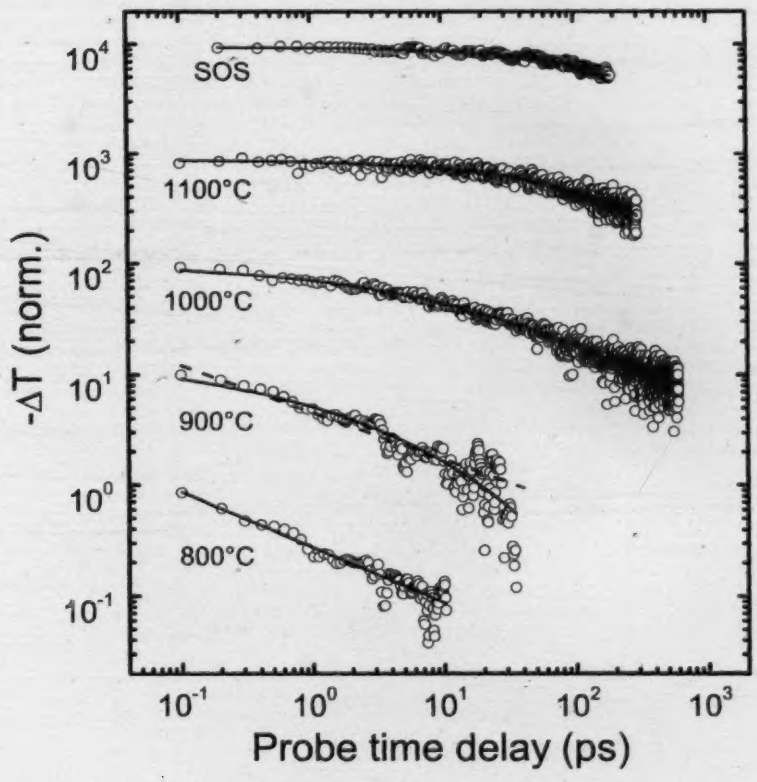

Figure 11.6: Log-log plots of the differential THz signals shown in Fig. 11.5(a)(e) but over longer time scales and scaled for clarity. The solid lines are fits to the decay dynamics: biexponential for SOS, stretched exponential for Si-NCs with T_a=900, 1000, and 1100°C, and power law for Si-NCs with T_a=800 and 900 °C (dashed). Fit parameters are given in the text.

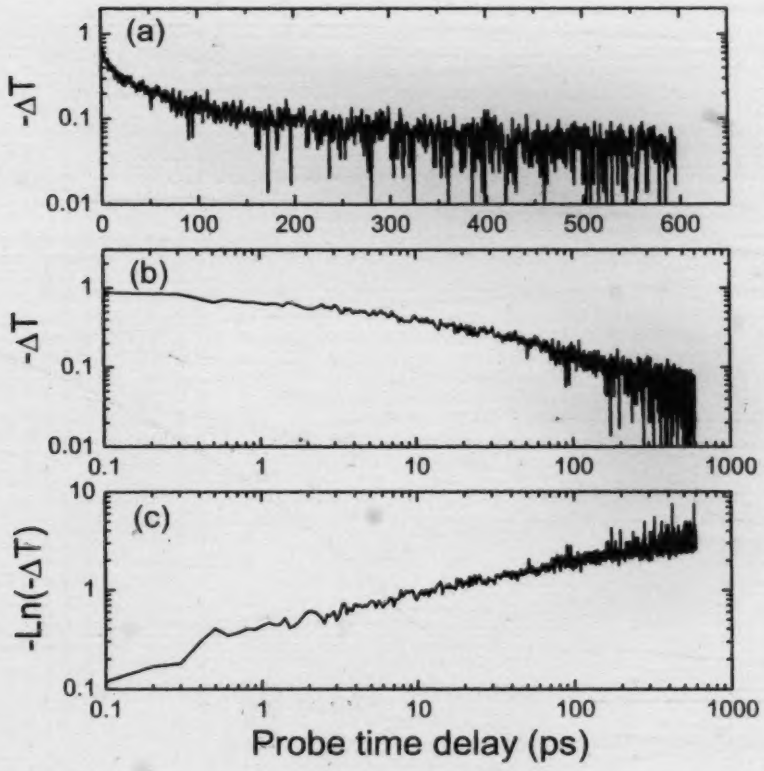

Figure 11.7: Normalized differential THz transmission, -ΔT, of the T_a = 1000 °C Si-NC film plotted on a (a) log-lin, (b) log-log and (c) log(-Ln(-ΔT))-log(t) plot. The linear form in (c) demonstrates the decay is of the stretched exponential form.

consistent with transient absorption studies on ion-implanted Si-NCs by Klimov et al. [174] which concluded that the fast relaxation dynamics were due to trapping at Si/SiO_2 interface states within 10 ps, in fair agreement with the relaxation dynamics reported here. To determine the role of interface states in our Si-NC films, we compared the transient response of two identical Si-NC films, both annealed at 1000°C for 1 hour, but one annealed in N_2 + H_2 and the other only in N_2. When H_2 is included in the annealing process, it is known that it diffuses into the film and passivates dangling bonds (so-called "P_b" centers) at the NC surfaces [191, 192]. This effectively depletes a non-radiative recombination channel and results in an increased PL efficiency at ~900 nm by a factor of ~15 in our specimen. The film annealed without H_2 also showed a stretched exponential decay with $\tau = 2.9 \pm 0.4$ ps, ~3 times faster than the surface-passivated sample as shown in Fig. 11.8. The lower PL efficiency and the shorter carrier lifetime in the sample not annealed in H_2 are consistent with rapid carrier capture at Si/SiO_2 interface states. This is further supported by the transient signals in smaller nanoclusters (formed at lower T_a) decaying much faster due to a higher surface-area-to-volume ratio, also in agreement with previous work [174].

11.5 THz electrodynamics

Figures 11.9 and 11.10 show the complex conductivity spectra for epitaxial SOS, poly-nc-Si, and three Si-NC samples (T_a = 900, 1000, 1100°C). The complex conductivity of the bulk-like SOS sample is well described by a simple Drude model with a plasma frequency $\omega_p/2\pi = 32 \pm 1$ THz ($\omega_p^2 = ne^2/\epsilon_0 m^*$) and a scattering time $\tau = 35 \pm 1$ fs, as shown by the fits (solid lines) to both the real and imaginary components of the conductivity. Assuming an electron effective mass $m^* = 0.26$ m_e [58], these fit parameters correspond to a carrier density $n = 3.3 \times 10^{18}$ cm^{-3} and a carrier mobility $\mu = e\tau/m^* = 240$ cm^2/Vs, in reasonable agreement with an estimate of $n_{max} = 3.1 \times 10^{18}$ cm^{-3} from the experimental pump fluence and an optical penetration depth of $\delta_{400nm} = 82$ nm [193] and literature values for the carrier mobility in SOS of $\mu = 200 - 400$ cm^2/Vs [194]. Examining the poly-nc-Si and Si-NC spectra in Fig. 11.9, two features are evident. The first is a shift of spectral weight in $\sigma_1(\omega)$ away from zero frequency, which becomes more pronounced

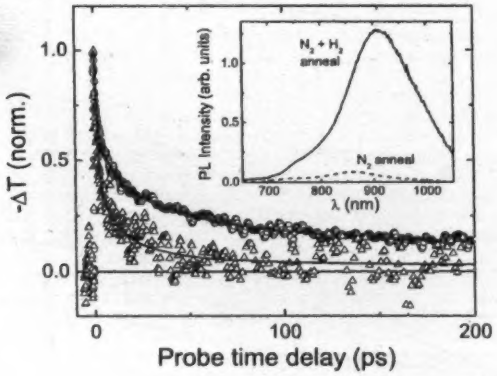

Figure 11.8: Normalized negative differential THz transmission, -ΔT, of Si-NC films annealed at 1000°C in H_2 and N_2 (o) and N_2 only ($\triangle$). The solid lines are stretched exponential fits to the data. The inset compares the room temperature photoluminescence (PL) of the two films, excited with both 325 and 442 nm CW laser lines.

in the Si-NC films, and a negative $\sigma_2(\omega)$. These features are incompatible with a Drude model or its simple derivatives [11, 58], and have been observed in systems exhibiting localization of charge carriers [36, 75, 74, 195].

To describe the THz conductivity data, we have chosen the Drude-Smith model described in Section 5.3. To reiterate, the Drude-Smith model is a relatively simple classical model that was formulated to describe systems in which the real part of the conductivity is suppressed by disorder by incorporating memory effects in the

Sample	τ	c	μ_m
SOS	35±1	-0.007±0.004	240±7
poly-nc Si	26±1	-0.830±0.010	30±3
900°C	16±1	-0.962±0.002	4.2±0.2
1000°C	12.9±0.5	-0.972±0.002	2.4±0.3
1100°C	17.6±0.5	-0.983±0.002	1.7±0.2

Table 11.1: Parameters for the Drude-Smith fits in Figs. 11.9 and 11.10.

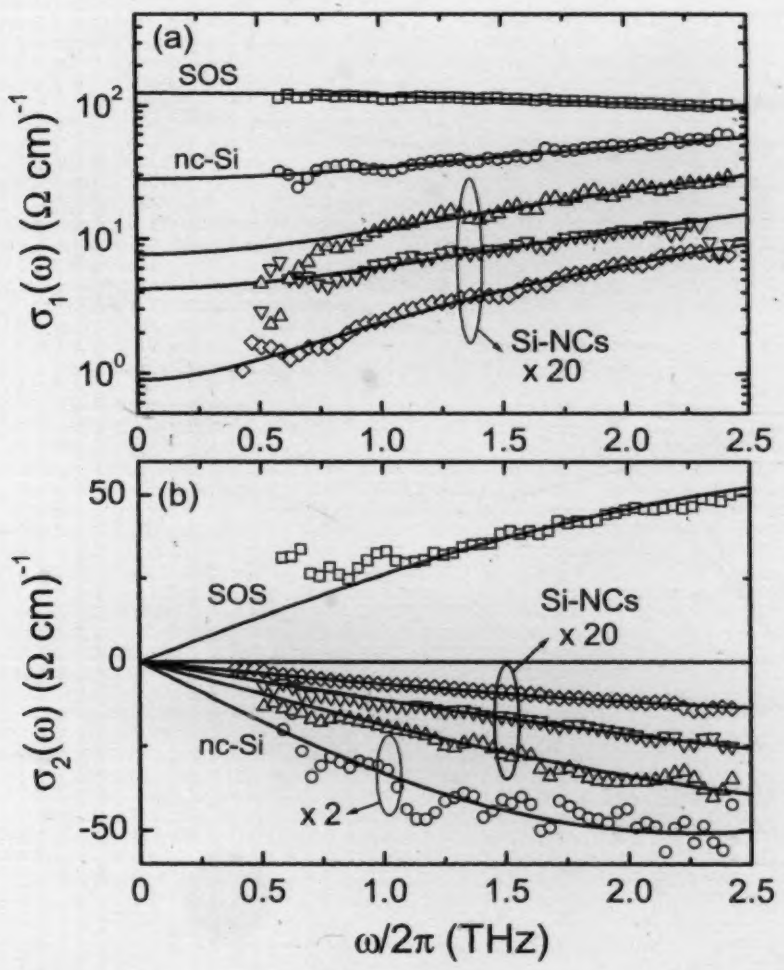

Figure 11.9: Terahertz conductivity spectra showing (a) $\sigma_1(\omega)$ and (b) $\sigma_2(\omega)$ for the SOS film (□) 100 ps after excitation ($30\mu J/cm^2$), poly-nc-Si film (○) 10 ps after excitation ($110\ \mu J/cm^2$), and Si-NC films annealed at 900°C (△), 1000°C (▽), and 1100°C (◇) at probe time delays of 4, 10, and 100 ps, respectively ($550\mu J/cm^2$). Solid lines are fits to the Drude-Smith model with parameters given in Table 11.1.

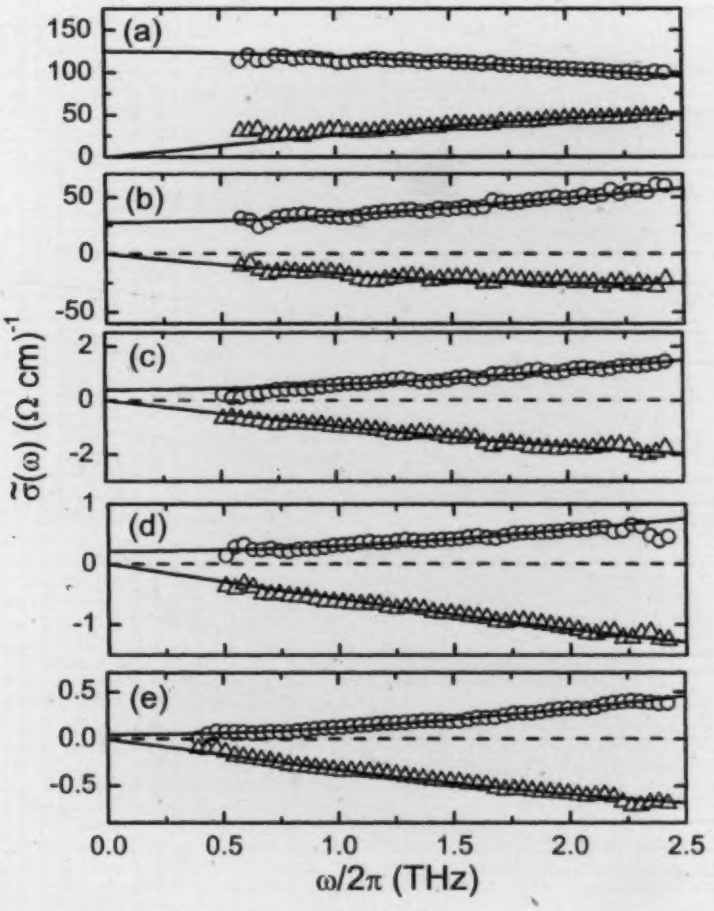

Figure 11.10: Real (open circles) and imaginary (open triangles) parts of the complex conductivity for (a) the SOS film 100 ps after excitation (30 μJ/cm^2), (b) the poly-NC-Si film 10 ps after excitation (110 μJ/cm^2), and (c - e) the Si-NC films annealed at (c) 900 C, (d) 1000 C and (e) 1100 C, 4, 10 and 100 ps after excitation (550 μJ/cm^2), respectively. Solid lines are fits to the Drude-Smith model with parameters given in Table 11.1.

scattering process. The real and imaginary parts of the complex conductivity in the Drude-Smith formalism is given by Eqs. 5.17 and 5.18, respectively. The backscattering parameters, c parameterizes the persistence of velocity after the first scattering event. The backscattering parameter, c, can vary between 0 and -1, corresponding to Drude conductivity for c = 0 and complete carrier backscattering, or localization, for c = -1. This model has been successfully applied to the transient THz conductivity observed in InP and TiO_2 nanocrystals [75, 74], but has been criticized as being unphysical, citing that it requires carriers to scatter only once [176]. However, this need not be true since, as was suggested by Smith [93], the set of c_j for $j > 1$ can all be zero (see Eq. 5.16), corresponding to a transition from ballistic to diffusive propagation where the persistence of velocity occurs only for the first scattering event. Excellent fits to the Drude-Smith model are obtained *simultaneously* for both $\sigma_1(\omega)$ and $\sigma_2(\omega)$, as shown in Fig. 11.9, for a given set of fit parameters ω_p, τ and c, as summarized in Table 11.1.

Long-range transport, which is hindered by disorder, is also parameterized by c in the Drude-Smith model. The macroscropic dc mobility in the Drude-Smith model is given by $\mu_m = \mu(1+c)$, where μ is the carrier mobility in the bulk single-crystal phase. The real component of the THz conductivity for the poly-nc-Si sample in Fig. 11.9(a) shows a dc conductivity which is suppressed ($c = -0.83 \pm 0.01$) but certainly not zero. This reflects the partial carrier localization within the nanocrystalline Si grains with long-range transport between the connected grains. The real conductivity for the Si-NC samples in Fig. 11.9(a) shows a dc conductivity that is highly suppressed with c as high as -0.983 ± 0.001 for the sample annealed at 1100°C. Here, injected carriers are primarily localized to their parent nanocrystals where they remain highly mobile on nanometer-length scales, but their macroscopic mobility is greatly diminished due to the insulating SiO_2 barriers between the nanocrystals hindering long-range motion. That the dc conductivity is not extinguished entirely suggests tunneling or hopping between the silicon nanocrystals. This is further supported by examining how μ_m varies with anneal temperature, as listed in Table 11.1. With increasing T_a the Si-NC particle density decreases so that the spacing between the nanocrystals increases. It is then reasonable to expect that hopping or tunneling between nanocrystals would be suppressed in samples annealed at higher temperatures, resulting in the

observed lowering of the macroscopic mobility μ_m at higher anneals.

To test for the existence of a macroscopic dc mobility for photoinjected carriers in the Si-NC films we performed a steady-state photoconductivity experiment on the $T_a = 1000°C$ Si-NC sample by depositing an interdigitated Cr/Au electrode structure (10 μm finger width and spacing) on top of the Si-NC film and illuminating the active region with a HeCd laser at a wavelength of 442 nm. The resistance was greater than 300 GΩ in the dark state and about 10 GΩ when illuminated with the laser source, verifying the existence of a macroscopic dc photoconductivity in the Si-NC samples consistent with the THz conductivity results as $\omega \rightarrow 0$.

The pump-probe time delay dependence of the complex conductivity was investigated only in the $T_a = 1100°C$ Si-NC sample, since the photoconductive lifetime was long enough to keep the signal strengths high even at several hundred ps after excitation. The transient conductivity response is shown in Fig. 11.11(a) for delay times 10, 30, 100 and 200 ps after photoexcitation. A surprising result is that the real part of the conductivity, σ_1, remains relatively unchanged as the photoconductive signal decays, whereas the capacitive response of σ_2 gets smaller. This is a strange result in some respects because the real and imaginary parts of the conductivity are connected through Kramers-Kronig relations. A change in one is often accompanied by a change in the other, albeit this change may occur in a different frequency range. The Drude-Smith model provides excellent fits to these data, but all three parameters must vary to reproduce the data, as seen in Fig. 11.11(b) and (c). This is an obvious short-coming of the phenomenological model, because, ideally, such a simple variation would be reproduced by changing a single parameter which represented the underlying physics. Nevertheless, the conductivity data is better described with the Drude-Smith model than with any of the tested alternatives.

Many other conductivity models were examined to determine if they were capable of describing the observed transient complex conductivity in these Si-NC films. A Drude-Lorentz model was found to also describe the data equally as well as the Drude-Smith model. The fit, however, required an oscillator with a center frequency of about 9 THz (37 meV) with an unphysically small oscillator damping time of 10 fs ($\sim$ 70 meV) for the $T_a = 1100°C$ Si-NC film. Furthermore, this fit required 5 varying parameters rather than the 3 used in the Drude-Smith fits.

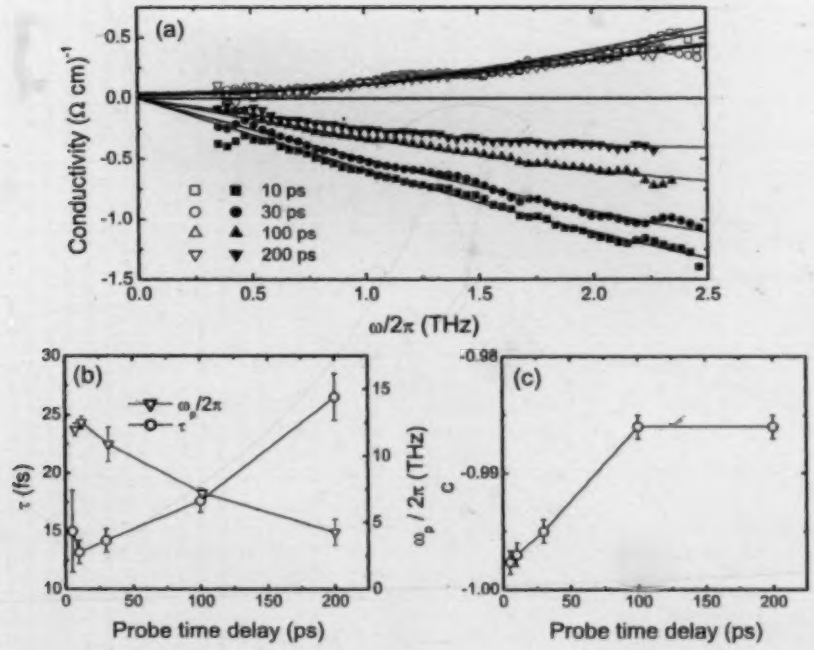

Figure 11.11: Terahertz conductivity spectra for the Si-NC film annealed at 1100°C at probe time delays of 10, 30, 100, and 200 ps after photoexcitation by the 400 nm pump pulse. ($\sigma_1(\omega)$ (open symbols) is positive and $\sigma_2(\omega)$ (filled symbols) is negative.) The solid lines are Drude-Smith fits to the data, with the probe time delay dependence of the corresponding scattering time τ and plasma frequency $\omega_p/2\pi$ shown in (b) and backscatter parameter c shown in (c). The terahertz conductivity spectra at a probe time delay of 5 ps is similar to that at 10 ps and is not shown in (a) for clarity.

Another theoretical framework, effective medium theory, is classical in nature and was formulated to appropriately average the contributions to an effective conductivity of a mixture from its conducting and insulating constituents. In particular the effective medium approximation (EMA) formulated by Brüggeman [196] and later refined by Stroud [197] was examined. Assuming a mixture of conducting metallic spheres and insulating spheres, EMA calculates the effective conductivity of the mixture by the equation

$$\frac{p(\sigma_m - \sigma_{eff})}{\sigma_m + (d-1)\sigma_{eff}} = \frac{(p-1)(\sigma_i - \sigma_{eff})}{\sigma_i + (d-1)\sigma_{eff}} \tag{11.1}$$

where m, i, and eff subscripts denoting metallic, insulating and effective, d is the spatial dimension and p is the volume fraction of metallic inclusions. EMA is an improvement over other effective medium theories such as Maxwell-Garnett (MG) because it contains the possibility of a metal-insulator transition occurring at a p value not equal to 1 or 0, but somewhere in between as experiment and more complicated percolation theories have verified. While EMA predicts a metal-insulator transition for such a mixture, it is known to break down close to the transition and gives an incorrect effective conductivity the closer the system gets to the transition [198]. Previous THz studies of ion-implanted Si nanoparticles used MG theory to explain the observed complex conductivity [36], however this was in the dilute limit where MG is valid. In perfectly phase segregated SiO films where the molar ratio of Si to SiO_2 is 1:1, the p parameter would be 0.306, calculated from the molar volumes of Si (12.06 cm^3/mol) and SiO_2 (27.3 cm^3/mol) putting it far from the dilute limit and making EMA more appropriate. Fig. 11.12 shows the attempted EMA fits to the T_a = 1100°C complex conductivity data taken 100 ps after excitation, shown as dark grey lines. Here we have assumed the conductivity of the insulating component is fixed as $\sigma_2 = -\epsilon_0 \omega n^2_{SiO_2}$, and the conducting component conductivity is described by a Drude model, with the parameters ω_p, τ and p allowed to vary. The dimensionality was taken as d = 3, because of the relatively thick (1μm) films. Eq. 11.1 was solved numerically to obtain the values of complex conductivity. One can see the EMA provides an adequate description of the imaginary part of the conductivity with $\omega_p/2\pi$ = 0.66 THz, τ = 17 fs and p = 0.63, but produces a real part which is sub-linear

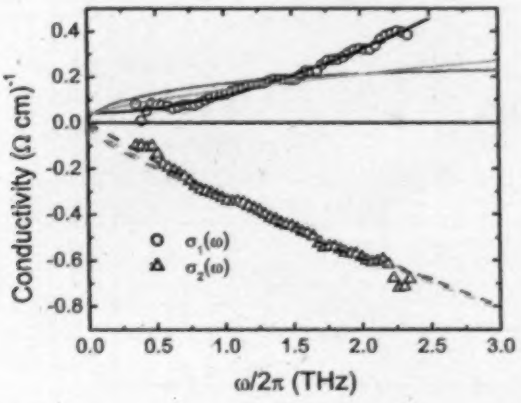

Figure 11.12: Complex conductivity data for the $T_a = 1100°C$ film 100 ps after 400 nm excitation at a fluence of 540 $\mu J/cm^2$. The lines are fits to the Drude-Smith (black), Brüggeman EMA (grey) and nearest neighbor tunneling EMA (light grey) models, with solid and dashed lines being σ_1 and σ_2, respectively.

with frequency as opposed to the clear super-linear behaviour observed in the data. Furthermore, ω_p is extremely small considering the high excitation and the volume fraction, p, is much larger than the maximum Si volume fraction of 0.306, calculated from the stoichiometry. For these reasons, EMA was discarded.

Another version of effective medium theory was examined, describing nearest neighbor tunneling of a dilute system of electrons between states randomly distributed in space [199, 200, 135]. The complex conductivity is given by the solution to the equation

$$\frac{\tilde{\sigma}}{\sigma_{dc}} ln\left(\frac{\tilde{\sigma}}{\sigma_{dc}}\right) = i\frac{\omega}{\omega_0} \tag{11.2}$$

where the frequency is normalized by a characteristic frequency ω_0. Fig. 11.12 shows the results of fits after numerically solving Eq. 11.2, using $\sigma_{dc} = 0.04(\Omega cm)^{-1}$ and $\omega_0/2\pi = 0.18$ THz. Again, σ_2 is well reproduced with these fit parameters but the functional frequency dependence of σ_1 is sub-linear, contrary to the data.

Percolation theories were examined as well, as these have successfully been applied to ultrathin metal films on the order of a few monolayers, where nanoislands

of metal form and the filling of space depends on the thickness of the film [201, 92]. Because of the relatively large film thickness (1 micron) we assumed three dimensional percolation theory was more appropriate. For d = 3, the percolation threshold, where there is an onset of dc conductivity as a macroscopic percolation path, is at a metallic volume fraction of 0.3116 on a cubic lattice and 0.31 for randomly packed spheres. Both values are very close to the estimated volume fraction of Si in $SiO_{x=1}$ films, and it thus assumed that percolation theories close to the threshold are appropriate. The simplest percolation model is the R-C model, where a portion of the bonds on a cubic lattice are filled by resistors, and the remainder by capacitors [202, 131, 203]. The high frequency ($10^{12}-10^{14}$ is typically considered high) ac conductivity for a system close to the percolation threshold, is given by [204]

$$\tilde{\sigma}(\omega) \propto (i\omega)^{t/(s+t)} \tag{11.3}$$

where s and t are universal scaling exponents. In three dimensions, s = 0.73 and t = 1.9 [203], giving $\tilde{\sigma}(\omega) \propto (i\omega)^{0.72}$. Thus σ_1 and σ_2 follow a power law of 0.72, which is not observed in the data. A cluster tunnel junction model for far-infrared absorption by small metal-insulator composites was also explored [205], however despite this model being able to reproduce the absorption data the error on the fitting parameters were 10 - 100 times larger than the actual fitting values and so no conclusions could be drawn. However, it is interesting that this type of model can explain the observed absorption coefficients with reasonable values for particle size and spacing.

11.6 SiO_x (x = 0 to 1.2) samples

We now examine the THz conductivity dynamics and transient complex conductivity of photoexcited SiO_x films with varying oxygen concentration, or equivalently, silicon content, annealed at various temperatures with x varying from 0 to 1.4. A series of samples was grown by simultaneous thermal and electron beam evaporation of Si, SiO and SiO_2 to obtain the various stoichiometries, which were verified by microprobe analysis [206]. The film thickness was 200 nm, deposited on a 1.0 mm thick fused silica substrate. The series was then annealed for 60 minutes in an

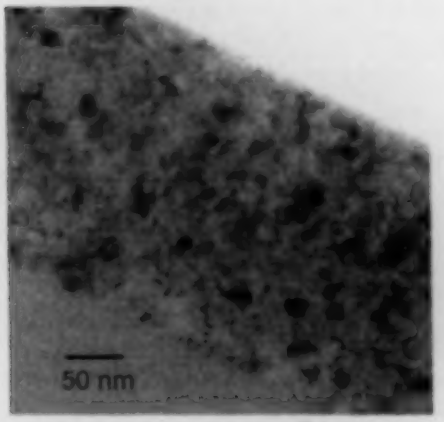

Figure 11.13: Bright field TEM image of SiO_x film with x = 0, annealed at 1000°C. The crystalline grains are visible as dark spots in the image.

approximately 95 % N_2 and 5 % H_2 mixture at a pressure of $\sim$ 1.2 atm, at temperatures from 700 - 1100°C. After annealing, the phase segregation process occurs creating films of variable Si content, progressing from a pure poly-nanocrystalline Si film to a pure glass film. This processing enabled a range of Si content films to be obtained that bridge the annealing temperature at which the Si particles go through an amorphous-to-crystalline transition (at x = 1.0). By investigating the ultrafast conductivity dynamics of these photoexcited films, it was thought that one should be able to view the percolative transition between a photoconducting state (high Si content film) to an insulating state (low Si content film), as determined by the extrapolation of THz conductivity data to zero frequency (σ_{dc}). Also, we hoped to get a better understanding of how the amorphous nature of the Si clusters influences the THz photoconductivity dynamics, and what effect the crystallization of the Si clusters has on the measured signals.

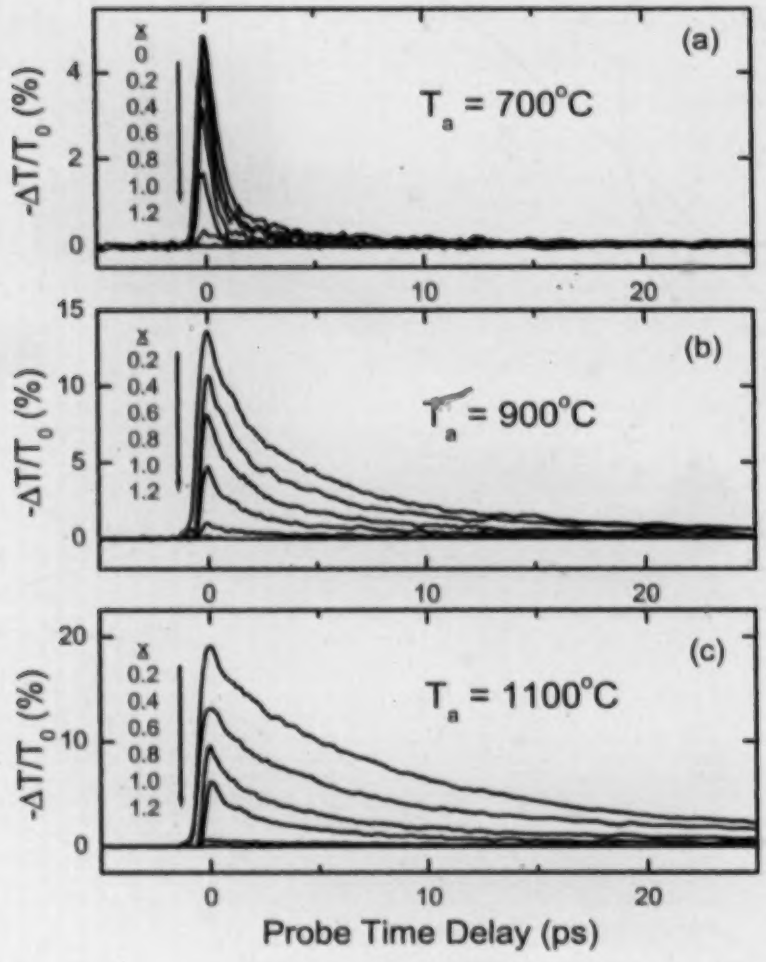

Figure 11.14: Negative differential transmission of the SiO_x series with varying Si content from x = 0.0 to x = 1.2 for T_a = 700 and x = 0.2 - 1.2 for T_a = 900 and 1100°C. The 400 nm pump fluence was 580 $\mu J/cm^2$ with the samples at ambient room temperature.

11.6.1 Carrier dynamics of SiO_x films

Negative differential THz transmission scans were performed at room temperature on the series of 200 nm thick SiO_x films with x varying from 0.2 to 1.2. For x = 0, it was found that annealing at such high temperatures (T_a > 700°C) lead to structural damage of the films leading to inhomogeneity across the sample surface, whereas the x = 0.2 films were homogeneous. For x $\geq$ 1.2 the small signals and shorter interaction length prohibited data collection. Fig. 11.14 shows the negative differential transmission for the 200 nm thick SiO_x-on-glass series with x = 0.2 - 1.2, under 400 nm excitation at a fluence of 580 $\mu J/cm^2$ for T_a = (a) 700, (b) 900, and (c) 1100°C. There are several things of note, the first being the films show a trend towards smaller peak -$\Delta T/T_0$ at all three anneal temperatures with decreasing silicon content. It was thought that this trend was due to decreased pump absorption with increasing anneal temperature, but when normalized to the pump absorption by dividing by the factor $1-exp[-200nm/\delta(x)]$ where $\delta(x)$ is the 400 nm pump penetration depth, this trend is still present, although weaker as seen in Fig. 11.15. Also, the peak $-\Delta T/T_0$ increases for the same x for higher anneal temperatures. Finally, the lifetime also shows a decreasing trend as the anneal temperature is lowered while maintaining the same x value. This is consistent with the THz studies performed on the 1 μm thick, x = 1.0 films in the previous section [83].

The decreasing trend in signal strength with decreasing Si content seems reasonable, since the amount of photoconductive material probed by the THz pulse decreases with increasing x and is replaced by insulating SiO_2. Also, the overall trend of decreasing signal with decreasing anneal temperature could be assigned again to the reduction of photoconductive silicon, since the phase segregation process will not be complete at temperatures lower than 1100°C [178]. With decreasing photoconductive material content, one would expect to reach a point where there is no longer a macroscopic percolative path for conduction, and thus the dc conductivity would drop drastically at a given x value. Literature reports that this concentration corresponds to x $\sim$ 1.0 [207], below which identifiable connectivity between nanocrystals becomes visible in TEM studies and there is a large increase in electronic transport properties [208, 209]. As mentioned above, this is also consistent with the photoexcited Si volume fraction (0.306) being close to the

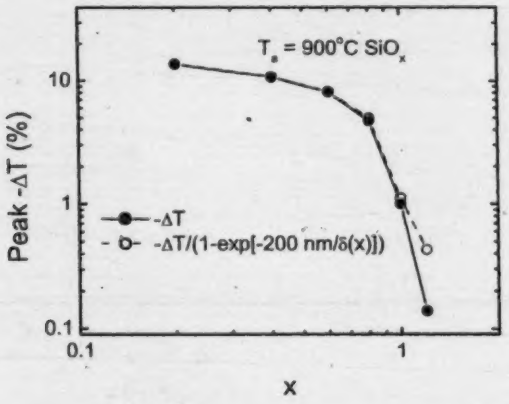

Figure 11.15: Peak negative differential THz transmission of the SiO_x $T_a = 900°C$ film with varying Si content from x = 0.2 to x = 1.2. The 400 nm pump fluence was 580 $\mu J/cm^2$ with the samples at ambient room temperature.

transition value predicted by percolation theory (~0.31) applied to cubic lattices and randomly packed hard spheres. The sharp decrease in peak -ΔT at x $\approx$ 1 is in good agreement with these estimates of the percolation threshold.

Further information can be obtained by examining the transient complex conductivity for these films, for the entire series of x values. The transient complex conductivity for the $T_a = 1100°C$ series of SiO_x films with x = 0.2 - 0.8 is shown in Fig. 11.16, for 400 nm excitation at a fluence of 580 $\mu J/cm^2$, taken 5 ps after excitation for the entire series and 20 ps for x = 0.2 - 0.6. The progression in the conductivity behaviour from x = 0.2 to 0.8 is to a lower $\sigma_1(\omega)$, while the imaginary conductivity $\sigma_2(\omega)$ remains relatively unchanged. This indicates that above the percolative transition, the dc (low ω) value of the σ_1 is the representative "order parameter" as one progresses towards the percolative transition at x $\approx$ 1.0. The complex conductivity is also shown 20 ps after excitation in Fig. 11.16 (b), showing much the same trend. Fig. 11.17 shows σ_{dc} for the $T_a = 1100°C$ film series from extrapolation to $\omega = 0$ for two pump-probe time delays versus the Si volume fraction. The volume fraction is calculated using the Si and SiO_2 molar volumes

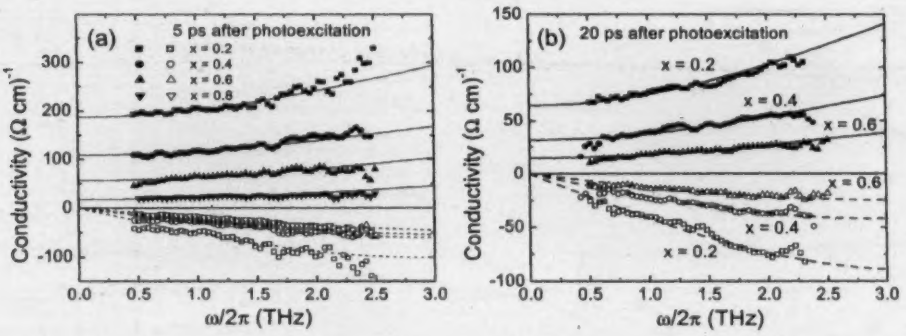

Figure 11.16: Room temperature frequency dependent complex conductivity of the 200 nm thick T_a = 1100°C SiO_x samples with x varying from 0.2 - 0.8, (a) 5 ps and (b) 20 ps after 400 nm excitation at a fluence of 580 $\mu J/cm^2$.

of 12.06 and 27.3 cm^3/mol, respectively, and is given as

$$VF_{Si} = \frac{(2-x)V_{mol}^{Si}}{xV_{mol}^{SiO_2} + (2-x)V_{mol}^{Si}} \tag{11.4}$$

The dc conductivity drops rapidly with decreasing Si content. The smaller photoconductive lifetime at lower anneal temperatures can be linked again with the smaller crystalline grain sizes, verified by TEM. Smaller crystalline grains have a higher surface-area-to-volume ratio, and therefore an abundance of surface states to trap mobile charge carriers, after which they become immobile and are no longer sensed by the THz pulse.

11.7 Summary

In summary, we have investigated the transient THz conductivity of silicon thin films with various degrees of structural disorder. A Drude-Smith model was used to describe a transition in the THz conductivity from Drude-like in bulk-Si to more localized behaviour in poly-nc-Si and Si-NCs in SiO_2. The lifetime of the transient photoconductivity in the Si-NC films was found to be dominated by trapping at interface states, decaying on a 1-200 ps time scale depending on the

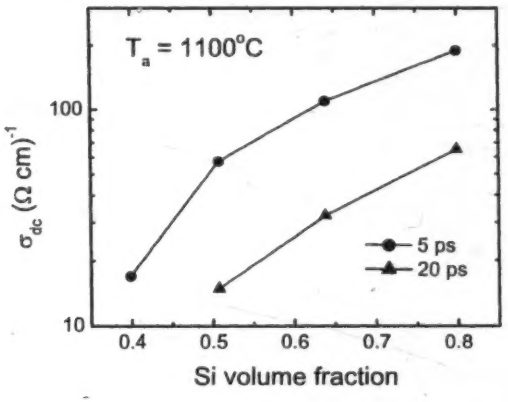

Figure 11.17: Extracted dc conductivity from Drude-Smith fits to the transient complex conductivity of the $T_a = 1100°C$ SiO_x series with x = 0.2 - 0.8 and taken at pump-probe time delays of 5 and 20 ps.

anneal temperature. The form of photoconductive decay is a power law for the amorphous films annealed below the crystallization temperature of 900°C and a stretched exponential above this temperature. This dispersive transport can be connected with the inherent disorder of the system, and the size distribution of nanocrystals. Evidence for long-range transport in the Si-NC samples was also observed.

In the Si-rich oxide system SiO_x with varying x, we have examined the THz response as the Si content is reduced through the percolative transition at $x \approx 1.0$. The peak photoconductivity drops sharply at the percolative transition, corresponding to a loss of macroscopic connectivity. The conductivity dynamics are again very well described by a Drude-Smith model of carrier backscattering. The photoconductive lifetime is dependent mainly on the anneal temperature, not Si content.

Part IV

Conclusions

In this collective work we have outlined experiments that benchmark the time-resolved THz spectroscopy technique in this lab using GaAs, as well as other semiconductors. Following this benchmark, we report on several systems of interest not only from a technological point of view, but also from a fundamental interest in systems whose electrodynamics deviate from the typical Drude metallic response.

The electronic properties of isovalent alloys of GaAs, used primarily for direct bandgap reduction, were investigated. Specifically, bismides were found to change the electron mobility very little, whereas nitrides show a significantly reduced electron mobility through resonant interaction with the conduction band. This leads to very different electrodynamics, with a large deviation in the complex conductivity from Drude behaviour valid for photoexcited GaAs. This is an extremely important technological finding, that the bandgap of GaAs can be lowered with dilute Bi doping without significantly reducing the electron mobility. There remains much work to be done on the effects of dilute nitrogen concentrations on the electronic properties of GaAs. There is controversy in the literature as to what extent N-related localized states in the conduction band interact with charge carriers, and whether or not they hybridize to form an impurity band. THz spectroscopy has been shown to be very sensitive to the localization introduced by N, and one can assume there is much to learn by doing a comprehensive study on the GaNAs system.

The carrier capture dynamics of InGaAs/GaAs quantum wire heterostructures based on high index substrate templates were examined using the polarization of the probing THz pulse, along with the inherent sensitivity to the capture process, to directly observe the capture from delocalized wetting layer states to states within the wires, localized perpendicularly. The capture event occurs over a 15-30 ps time scale, and is particularly sensitive to the thermal re-emission out of the wires back into the wetting layer states above 100 K. This is an important finding since devices based on quantum wires require an efficient capture of carriers from the wetting layer into the active wire layers. We have demonstrated that TRTS is an excellent alternative to more traditional time-resolved PL or time-resolved near field spectroscopy, as it senses changes in carrier mobility, not the population of an emitting state which can mask the bare capture time.

We have also examined the carrier capture dynamics of a novel system of

linearly aligned Stranski-Krastanow grown InGaAs/GaAs quantum dot chains. Again, using the polarization of the THz pulse the dynamics of the two-dimensional wetting layer and barrier states can be separated from that of a one-dimensional wetting layer. Capture into one-dimensional wetting layer states results in a photoconductive anisotropy until the carriers are captured into the quantum dots. Thus we have shown that by doing polarization dependent optical pump-THz probe experiments, the capture event can be observed even in more complicated systems where there are multiple wetting layer structures. The capture of injected carriers into the quantum dots occurs on a 3-5 ps time scale, and is again very sensitive to thermal reemission back into the wetting layer states, which is efficient for temperatures above 100 K.

Finally, the transient THz conductivity dynamics of silicon nanocrystal films were investigated, along with films of varying Si content made by controlling both the stoichiometry of SiO_x films and the annealing temperature which drives a phase segregation process. This phase segregation process, for non-zero x values, leads to nanocrystals of Si embedded in glass. The transient conductivity of the Si-NC films were dominated by surface trapping of injected carriers at unpassivated Si/SiO_2 interface states on a 1 - 100 ps time scale, depending on the passivation and surface-area-to-volume ratio. Transient THz electrodynamics is a very sensitive probe of the disorder of the system. For epitaxial silicon on sapphire films, the electrodynamics are well described by a bulk Drude form. However, for disordered Si films, where portions of photoconducting Si are replaced by insulating SiO_2 dielectric, the conductivity is suppressed at low frequencies corresponding to a hindrance of long range transport due to disorder, and is described well by the Drude-Smith model. The severity of this suppression is dependent on the Si content, and therefore the connected nature of the Si grains. A metal-insulator percolative transition is observed to occur at $x = 1.0$, corresponding to a volume fraction of 0.306, close to the percolative threshold value predicted by percolation theory for randomly packed hard spheres.

Bibliography

[1] F. A. Hegmann, O. Ostroverkhova, and D. G. Cooke, Probing organic semiconductors with terahertz pulses, in *Photophysics of Molecular Materials: From Single Molecules to Single Crystals*, edited by G. Lanzani, Wiley, 2006.

[2] http://www.ioffe.rssi.ru/SVA/NSM/Semicond/GaAs/

[3] R. D. Dupuis, P. D. Dapkus, N. Holonyak, E. A. Rezek, and R. Chin, Appl. Phys. Lett. **32**, 295 (1978).

[4] A. Tredicucci, C. Gmachl, F. Capasso, D. L. Sivco, A. L. Hutchinson, and A. Y. Cho, Nature **396**, 350 (1998).

[5] M. Walther, E. Kapon, C. Caneau, D. M. Hwang, and L. M. Schiavone, Appl. Phys. Lett. **62**, 2170 (1993).

[6] S. Fafard, K. Hinzer, S. Raymond, M. Dion, J. McCaffrey, Y. Feng, and S. Charbonneau, Science **274**, 1350 (1996).

[7] J. Shah, *Ultrafast spectroscopy of semiconductors and semiconductor nanostructures* (Springer, Berlin ; New York, 1999).

[8] M. C. Nuss, K. W. Goossen, J. P. Gordon, P. M. Mankiewich, M. L. Omalley, and M. Bhushan, J. Appl. Phys. **70**, 2238 (1991).

[9] R. A. Kaindl, M. A. Carnahan, D. Hagele, R. Lovenich, and D. S. Chemla, Nature **423**, 734 (2003).

[10] R. Huber, R. A. Kaindl, B. A. Schmid, and D. S. Chemla, Phys. Rev. B **72**, 161314 (2005).

[11] M. Beard, G. Turner, and C. Schmuttenmaer, Phys. Rev. B **62**, 15764 (2000).

[12] R. Huber, F. Tauser, A. Brodschelm, M. Bichler, G. Abstreiter, and A. Leitenstorfer, Nature **414**, 286 (2001).

[13] M. Walther, P. Plochocka, B. Fischer, H. Helm, and P. U. Jepsen, Biopolymers **67**, 310 (2002).

[14] F. A. Hegmann, J. B. Williams, B. Cole, M. S. Sherwin, J. W. Beeman, and E. E. Haller, Appl. Phys. Lett. **76**, 262 (2000).

[15] R. P. S. M. Lobo, J. D. LaVeigne, D. H. Reitze, D. B. Tanner, and G. L. Carr, Rev. Sci. Instrum. **73**, 1 (2002).

[16] R. W. Schoenlein, S. Chattopadhyay, H. H. W. Chong, T. E. Glover, P. A. Heimann, C. V. Shank, A. A. Zholents, and M. S. Zolotorev, Science **287**, 2237 (2000).

[17] G. L. Carr, M. C. Martin, W. R. McKinney, K. Jordan, G. R. Neil, and G. P. Williams, Nature **420**, 153 (2002).

[18] K. Holldack, S. Khan, R. Mitzner, and T. Quast, Phys. Rev. Lett. **96**, 054801 (2006).

[19] A. Cavalleri, S. Wall, C. Simpson, E. Statz, D. W. Ward, K. A. Nelson, M. Rini, and R. W. Schoenlein, Nature **442**, 664 (2006).

[20] U. Tisch, E. Finkman, and J. Salzman, Appl. Phys. Lett. **81**, 463 (2002).

[21] S. R. Kurtz, A. A. Allerman, E. D. Jones, J. M. Gee, J. J. Banas, and B. E. Hammons, Appl. Phys. Lett. **74**, 729 (1999).

[22] P. M. Asbeck, R. J. Welty, C. W. Tu, H. P. Xin, and R. E. Welser, Semicond. Sci. Tech. **17**, 898 (2002).

[23] F. Ishikawa, G. Mussler, K. J. Friedland, H. Kostial, K. Hagenstein, L. Daweritz, and K. H. Ploog, Appl. Phys. Lett. **87**, 262112 (2005).

[24] S. Fahy and E. P. O'Reilly, Appl. Phys. Lett. **83**, 3731 (2003).

[25] S. Francoeur, M. J. Seong, A. Mascarenhas, S. Tixier, M. Adamcyk, and T. Tiedje, Appl. Phys. Lett. **82**, 3874 (2003).

[26] H. C. Liu, M. Gao, J. McCaffrey, Z. R. Wasilewski, and S. Fafard, Appl. Phys. Lett. **78**, 79 (2001).

[27] J. M. Moison, F. Houzay, F. Barthe, L. Leprince, E. Andre, and O. Vatel, Appl. Phys. Lett. **64**, 196 (1994).

[28] L. Pavesi, L. Dal Negro, C. Mazzoleni, G. Franzo, and F. Priolo, Nature **408**, 440 (2000).

[29] D. H. Auston, Appl. Phys. Lett. **26**, 101 (1975).

[30] D. H. Auston, K. P. Cheung, and P. R. Smith, Appl. Phys. Lett. **45**, 284 (1984).

[31] D. H. Auston, K. P. Cheung, J. A. Valdmanis, and D. A. Kleinman, Phys. Rev. Lett. **53**, 1555 (1984).

[32] P. R. Smith, D. H. Auston, and M. C. Nuss, J. Quantum Electron. **24**, 255 (1988).

[33] C. Fattinger and D. Grischkowsky, Appl. Phys. Lett. **53**, 1480 (1988).

[34] C. Fattinger and D. Grischkowsky, Appl. Phys. Lett. **54**, 490 (1989).

[35] S. E. Ralph and D. Grischkowsky, Appl. Phys. Lett. **59**, 1972 (1991).

[36] H. Altan, F. Huang, J. F. Federici, A. Lan, and H. Grebel, J. Appl. Phys. **96**, 6685 (2004).

[37] J. T. Darrow, B. B. Hu, X. C. Zhang, and D. H. Auston, Opt. Lett. **15**, 323 (1990).

[38] D. You, R. R. Jones, P. H. Bucksbaum, and D. R. Dykaar, Opt. Lett. **18**, 290 (1993).

[39] G. Gallot, J. Q. Zhang, R. W. McGowan, T. I. Jeon, and D. Grischkowsky, Appl. Phys. Lett. **74**, 3450 (1999).

[40] P. Y. Han, M. Tani, F. Pan, and X. C. Zhang, Opt. Lett. **25**, 675 (2000).

[41] R. Huber, A. Brodschelm, F. Tauser, and A. Leitenstorfer, Appl. Phys. Lett. **76**, 3191 (2000).

[42] A. Rice, Y. Jin, X. F. Ma, X. C. Zhang, D. Bliss, J. Larkin, and M. Alexander, Appl. Phys. Lett. **64**, 1324 (1994).

[43] M. C. Beard, G. M. Turner, and C. A. Schmuttenmaer, J. Appl. Phys. **90**, 5915 (2001).

[44] F. E. Doany, D. Grischkowsky, and C. C. Chi, Appl. Phys. Lett. **50**, 460 (1987).

[45] K. P. H. Lui and F. A. Hegmann, Appl. Phys. Lett. **78**, 3478 (2001).

[46] K. P. H. Lui and F. A. Hegmann, J. Appl. Phys. **93**, 9012 (2003).

[47] Q. Wu, T. D. Hewitt, and X. C. Zhang, Appl. Phys. Lett. **69**, 1026 (1996).

[48] P. U. Jepsen, C. Winnewisser, M. Schall, V. Schyja, S. R. Keiding, and H. Helm, Phys. Rev. E **53**, R3052 (1996).

[49] A. Nahata, D. H. Auston, T. F. Heinz, and C. J. Wu, Appl. Phys. Lett. **68**, 150 (1996).

[50] P. C. M. Planken, H. K. Nienhuys, H. J. Bakker, and T. Wenckebach, J. Opt. Soc. Am. B **18**, 313 (2001).

[51] C. Kübler, R. Huber, and A. Leitenstorfer, Semicond. Sci. Tech. **20**, S128 (2005).

[52] D. Mittleman, *Sensing with terahertz radiation* (Springer, Berlin ; New York, 2003).

[53] M. Walther, B. Fischer, M. Schall, H. Helm, and P. U. Jepsen, Chem. Phys. Lett. **332**, 389 (2000).

[54] R. A. Cheville and D. Grischkowsky, Opt. Lett. **20**, 1646 (1995).

[55] R. H. Jacobsen, D. M. Mittleman, and M. C. Nuss, Opt. Lett. **21**, 2011 (1996).

[56] H. Harde, S. Keiding, and D. Grischkowsky, Phys. Rev. Lett. **66**, 1834 (1991).

[57] D. Grischkowsky, S. Keiding, M. Vanexter, and C. Fattinger, J. Opt. Soc. Am. B **7**, 2006 (1990).

[58] T. I. Jeon and D. Grischkowsky, Phys. Rev. Lett. **78**, 1106 (1997).

[59] T. I. Jeon and D. Grischkowsky, Appl. Phys. Lett. **72**, 3032 (1998).

[60] D. M. Mittleman, J. Cunningham, M. C. Nuss, and M. Geva, Appl. Phys. Lett. **71**, 16 (1997).

[61] P. C. M. Planken, M. C. Nuss, I. Brener, K. W. Goossen, M. S. C. Luo, S. L. Chuang, and L. Pfeiffer, Phys. Rev. Lett. **69**, 3800 (1992).

[62] M. C. Nuss, D. H. Auston, and F. Capasso, Phys. Rev. Lett. **58**, 2355 (1987).

[63] C. A. Schmuttenmaer, Chem. Rev. **104**, 1759 (2004).

[64] J. F. Federici, B. I. Greene, P. N. Saeta, D. R. Dykaar, F. Sharifi, and R. C. Dynes, Phys. Rev. B **46**, 11153 (1992).

[65] R. D. Averitt, G. Rodriguez, J. L. W. Siders, S. A. Trugman, and A. J. Taylor, J. Opt. Soc. Am. B **17**, 327 (2000).

[66] R. A. Kaindl, M. A. Carnahan, D. S. Chemla, S. Oh, and J. N. Eckstein, Phys. Rev. B **72**, 060510 (2005).

[67] M. Schall and P. U. Jepsen, Opt. Lett. **25**, 13 (2000).

[68] F. A. Hegmann, R. R. Tykwinski, K. P. H. Lui, J. E. Bullock, and J. E. Anthony, Phys. Rev. Lett. **89**, 227403 (2002).

[69] O. Ostroverkhova, D. G. Cooke, S. Shcherbyna, R. F. Egerton, F. A. Hegmann, R. R. Tykwinski, and J. E. Anthony, Phys. Rev. B **71**, 035204 (2005).

[70] J. Shan, F. Wang, E. Knoesel, M. Bonn, and T. F. Heinz, Phys. Rev. Lett. **90**, 247401 (2003).

[71] R. D. Averitt, A. I. Lobad, C. Kwon, S. A. Trugman, V. K. Thorsmølle, and A. J. Taylor, Phys. Rev. Lett. **87**, 017401 (2001).

[72] J. T. Kindt and C. A. Schmuttenmaer, J. Chem. Phys. **110**, 8589 (1999).

[73] M. C. Beard, G. M. Turner, and C. A. Schmuttenmaer, Nano Lett. **2**, 983 (2002).

[74] G. M. Turner, M. C. Beard, and C. A. Schmuttenmaer, J. Phys. Chem. B **106**, 11716 (2002).

[75] M. C. Beard, G. M. Turner, J. E. Murphy, O. I. Micic, M. C. Hanna, A. J. Nozik, and C. A. Schmuttenmaer, Nano Lett. **3**, 1695 (2003).

[76] D. Turchinovich, K. Pierz, and P. U. Jepsen, Phys. Status Solidi C **0**, 1556 (2003).

[77] D. A. Yarotski, R. D. Averitt, N. Negre, S. A. Crooker, A. J. Taylor, G. P. Donati, A. Stintz, L. F. Lester, and K. J. Malloy, J. Opt. Soc. Am. B **19**, 1480 (2002).

[78] R. P. Prasankumar, A. Scopatz, D. J. Hilton, A. J. Taylor, R. D. Averitt, J. M. Zide, and A. C. Gossard, Appl. Phys. Lett. **86**, 201107 (2005).

[79] T. I. Jeon, K. J. Kim, C. Kang, S. J. Oh, J. H. Son, K. H. An, D. J. Bae, and Y. H. Lee, Appl. Phys. Lett. **80**, 3403 (2002).

[80] T. I. Jeon, K. J. Kim, C. Kang, I. H. Maeng, J. H. Son, K. H. An, J. Y. Lee, and Y. H. Lee, J. Appl. Phys. **95**, 5736 (2004).

[81] D. G. Cooke, F. A. Hegmann, Y. I. Mazur, W. Q. Ma, X. Wang, Z. M. Wang, G. J. Salamo, M. Xiao, T. D. Mishima, and M. B. Johnson, Appl. Phys. Lett. **85**, 3839 (2004).

[82] D. G. Cooke, F. A. Hegmann, Y. I. Mazur, Z. M. Wang, W. Black, H. Wen, G. J. Salamo, T. D. Mishima, G. D. Lian, and M. B. Johnson, **to be submitted** (2006).

[83] D. G. Cooke, A. N. MacDonald, A. Hryciw, J. Wang, Q. Li, A. Meldrum, and F. A. Hegmann, Phys. Rev. B **73**, 193311 (2006).

[84] D. G. Cooke, F. A. Hegmann, E. C. Young, and T. Tiedje, Appl. Phys. Lett. **89**, 122103 (2006).

[85] M. Walther *et al.*, **to be submitted** (2006).

[86] R. Glover and M. Tinkham, Phys. Rev. **108**, 243 (1957).

[87] V. K. Thorsmølle, R. D. Averitt, X. Chi, D. J. Hilton, D. L. Smith, A. P. Ramirez, and A. J. Taylor, Appl. Phys. Lett. **84**, 891 (2004).

[88] O. Ostroverkhova, S. Shcherbyna, D. G. Cooke, R. F. Egerton, F. A. Hegmann, R. R. Tykwinski, S. R. Parkin, and J. E. Anthony, J. Appl. Phys. **98**, 033701 (2005).

[89] D. E. Aspnes and A. A. Studna, Phys. Rev. B **27**, 985 (1983).

[90] J. S. Dodge, C. P. Weber, J. Corson, J. Orenstein, Z. Schlesinger, J. W. Reiner, and M. R. Beasley, Phys. Rev. Lett. **85**, 4932 (2000).

[91] C. C. Homes, T. Timusk, X. Wu, Z. Altounian, A. Sahnoune, and J. O. Strm-Olsen, Phys. Rev. Lett. **67**, 2694 LP (1991).

[92] P. F. Henning, C. C. Homes, S. Maslov, G. L. Carr, D. N. Basov, B. Nikolic, and M. Strongin, Phys. Rev. Lett. **83**, 4880 (1999).

[93] N. V. Smith, Phys. Rev. B **64**, 155106 (2001).

[94] D. Mayou, Phys. Rev. Lett. **85**, 1290 (2000).

[95] N. Smith, private communication, 2006.

[96] M. Lundstrom, *Fundamentals of carrier transport* (Cambridge University Press, Cambridge, U.K. ; New York, 2000).

[97] N. S. Wingreen, C. J. Stanton, and J. W. Wilkins, Phys. Rev. Lett. **57**, 1084 (1986).

[98] M. Combescot and R. Combescot, Phys. Rev. B **35**, 7986 (1987).

[99] J. L. T. Waugh and G. Dolling, Phys. Rev. **132**, 2410 LP (1963).

[100] J. A. Kash and J. C. Tsang, Sol. State Electron. **31**, 419 (1988).

[101] P. N. Saeta, J. F. Federici, B. I. Greene, and D. R. Dykaar, Appl. Phys. Lett. **60**, 1477 (1992).

[102] G. E. Stillman, C. M. Wolfe, and J. O. Dimmock, J. Phys. Chem. Solids **31**, 1199 (1970).

[103] J. A. Kash, Phys. Rev. B **40**, 3455 (1989).

[104] O. Madelung, *Semiconductors–basic data* (Springer, Berlin ; New York, 1996).

[105] N. Laurand, S. Calvez, H. Sun, M. Dawson, J. Gupta, and G. Aers, Electron. Lett. **42**, 29 (2006).

[106] L. Bellaiche, S.-H. Wei, and A. Zunger, Phys. Rev. B **54**, 17568 (1996).

[107] W. G. Bi and C. W. Tu, Appl. Phys. Lett. **70**, 1608 (1997).

[108] N. Y. Li, C. P. Hains, K. Yang, J. Lu, J. Cheng, and P. W. Li, Appl. Phys. Lett. **75**, 1051 (1999).

[109] P. C. Chang, A. G. Baca, N. Y. Li, P. R. Sharps, H. Q. Hou, J. R. Laroche, and F. Ren, Appl. Phys. Lett. **76**, 2788 (2000).

[110] S. R. Kurtz, N. A. Modine, E. D. Jones, A. A. Allerman, and J. F. Klem, Semicond. Sci. Tech. **17**, 843 (2002).

[111] R. J. Welty, H. P. Xin, C. W. Tu, and P. M. Asbeck, J. Appl. Phys. **95**, 327 (2004).

[112] Y. Zhang, A. Mascarenhas, H. P. Xin, and C. W. Tu, Phys. Rev. B **61**, 7479 (2000).

[113] W. Shan, W. Walukiewicz, J. W. Ager, E. E. Haller, J. F. Geisz, D. J. Friedman, J. M. Olson, and S. R. Kurtz, Phys. Rev. Lett. **82**, 1221 (1999).

[114] J. D. Perkins, A. Mascarenhas, Y. Zhang, J. F. Geisz, D. J. Friedman, J. M. Olson, and S. R. Kurtz, Phys. Rev. Lett. **82**, 3312 (1999).

[115] P. R. C. Kent and A. Zunger, Phys. Rev. Lett. **86**, 2613 (2001).

[116] D. Fowler, O. Makarovsky, A. Patane, L. Eaves, L. Geelhaar, and H. Riechert, Phys. Rev. B **69**, 153305 (2004).

[117] M. P. Vaughan and B. K. Ridley, Phys. Rev. B **72**, 075211 (2005).

[118] W. Zhang, A. K. Azad, and D. Grischkowsky, Appl. Phys. Lett. **82**, 2841 (2003).

[119] Y. Zhang, A. Mascarenhas, H. P. Xin, and C. W. Tu, Phys. Rev. B **63**, 161303 (2001).

[120] R. Mouillet, L. A. de Vaulchier, E. Deleporte, Y. Guldner, L. Travers, and J. C. Harmand, Solid State Commun. **126**, 333 (2003).

[121] B. Fluegel, S. Francoeur, A. Mascarenhas, S. Tixier, E. C. Young, and T. Tiedje, Phys. Rev. Lett. **97**, 067205 (2006).

[122] K. Bertulis, A. Krotkus, G. Aleksejenko, V. Pacebutas, R. Adomavicius, G. Molis, and S. Marcinkevicius, Appl. Phys. Lett. **88**, 201112 (2006).

[123] S. Tixier, M. Adamcyk, T. Tiedje, S. Francoeur, A. Mascarenhas, P. Wei, and F. Schiettekatte, Appl. Phys. Lett. **82**, 2245 (2003).

[124] W. Walukiewicz, L. Lagowski, L. Jastrzebski, M. Lichtensteiger, and H. C. Gatos, J. Appl. Phys. **50**, 899 (1979).

[125] A. Janotti, S. H. Wei, and S. B. Zhang, Phys. Rev. B **65**, 115203 (2002).

[126] A. Mascarenhas, Y. Zhang, J. Verley, and M. J. Seong, Superlattice Microst **29**, 395 (2001).

[127] H. K. K. H. P. F. Ishikawa, K.-J. Friedland, Phys. Status Solidi C **3**, 623 (2006).

[128] K. M. Yu, W. Walukiewicz, J. Wu, D. E. Mars, D. R. Chamberlin, M. A. Scarpulla, O. D. Dubon, and J. F. Geisz, Nat Mater **1**, 185 (2002).

[129] J. Li, P. Carrier, S.-H. Wei, S.-S. Li, and J.-B. Xia, Phys. Rev. Lett. **96**, 035505 (2006).

[130] N. F. Mott, Philos. Mag. **26**, 1015 (1972).

[131] D. Stauffer and A. Aharony, *Introduction to percolation theory* (Taylor and Francis, London, 1994).

[132] D. Yu, C. J. Wang, B. L. Wehrenberg, and P. Guyot-Sionnest, Phys. Rev. Lett. **92**, 216802 (2004).

[133] M. Lax and H. Scher, Phys. Rev. Lett. **39**, 781 (1977).

[134] Y. Song, T. W. Noh, S. I. Lee, and J. R. Gaines, Phys. Rev. B **33**, 904 (1986).

[135] J. A. Reedijk, L. J. Adriaanse, H. B. Brom, L. J. de Jongh, and G. Schmid, Phys. Rev. B **57**, R15116 (1998).

[136] Y. Arakawa and H. Sakaki, Appl. Phys. Lett. **40**, 939 (1982).

[137] R. Rinaldi, A. Passaseo, M. De Giorgi, C. Turco, M. Devittorio, D. Cannoletta, and R. Cingolani, Solid State Electron. **42**, 1239 (1998).

[138] Q. Gong, R. Notzel, J. H. Wolter, H. P. Schonherr, and K. H. Ploog, J. Cryst. Growth **242**, 104 (2002).

[139] H. Wen, Z. M. Wang, and G. J. Salamo, Appl. Phys. Lett. **84**, 1756 (2004).

[140] U. Jahn, R. Notzel, J. Ringling, H. P. Schonherr, H. T. Grahn, K. H. Ploog, and E. Runge, Phys. Rev. B **60**, 11038 (1999).

[141] A. Richter, G. Behme, M. Suptitz, C. Lienau, T. Elsaesser, M. Ramsteiner, R. Notzel, and K. H. Ploog, Phys. Rev. Lett. **79**, 2145 (1997).

[142] E. Peronne, T. Polack, J. F. Lampin, F. Fossard, F. Julien, J. Brault, M. Gendry, O. Marty, and A. Alexandrou, Phys. Rev. B **63**, 081307 (2001).

[143] J. Christen, M. Grundmann, E. Kapon, E. Colas, D. M. Hwang, and D. Bimberg, Appl. Phys. Lett. **61**, 67 (1992).

[144] J. F. Ryan, A. C. Maciel, C. Kiener, L. Rota, K. Turner, J. M. Freyland, U. Marti, D. Martin, F. MorierGemoud, and F. K. Reinhart, Phys. Rev. B **53**, R4225 (1996).

[145] X. Q. Liu, A. Sasaki, N. Ohno, X. L. Wang, and M. Ogura, Appl. Phys. Lett. **77**, 1481 (2000).

[146] R. Kumar, A. S. Vengurlekar, A. V. Gopal, T. Melin, F. Laruelle, B. Etienne, and J. Shah, Phys. Rev. Lett. **81**, 2578 (1998).

[147] P. U. Jepsen, W. Schairer, I. H. Libon, U. Lemmer, N. E. Hecker, M. Birkholz, K. Lips, and M. Schall, Appl. Phys. Lett. **79**, 1291 (2001).

[148] Y. I. Mazur, Z. M. Wang, G. G. Tarasov, H. Wen, V. Strelchuk, D. Guzun, M. Xiao, G. J. Salamo, T. D. Mishima, G. D. Lian, and M. B. Johnson, J. Appl. Phys. **98**, 053711 (2005).

[149] D. S. Citrin, Phys. Rev. Lett. **69**, 3393 (1992).

[150] C. Lienau, V. Emiliani, T. Gunther, F. Intonti, and T. Elsaesser, Physica B **272**, 96 (1999).

[151] U. Bockelmann and G. Bastard, Phys. Rev. B **42**, 8947 (1990).

[152] H. Benisty, C. M. Sotomayortorres, and C. Weisbuch, Phys. Rev. B **44**, 10945 (1991).

[153] G. Wang, S. Fafard, D. Leonard, J. E. Bowers, J. L. Merz, and P. M. Petroff, Appl. Phys. Lett. **64**, 2815 (1994).

[154] B. Ohnesorge, M. Albrecht, J. Oshinowo, A. Forchel, and Y. Arakawa, Phys. Rev. B **54**, 11532 (1996).

[155] A. V. Uskov, F. Adler, H. Schweizer, and M. H. Pilkuhn, J. Appl. Phys. **81**, 7895 (1997).

[156] A. V. Uskov, J. McInerney, F. Adler, H. Schweizer, and M. H. Pilkuhn, Appl. Phys. Lett. **72**, 58 (1998).

[157] R. Ferreira and G. Bastard, Appl. Phys. Lett. **74**, 2818 (1999).

[158] D. Morris, N. Perret, and S. Fafard, Appl. Phys. Lett. **75**, 3593 (1999).

[159] U. Bockelmann and T. Egeler, Phys. Rev. B **46**, 15574 (1992).

[160] T. Inoshita and H. Sakaki, Phys. Rev. B **46**, 7260 (1992).

[161] J. Urayama, T. B. Norris, J. Singh, and P. Bhattacharya, Phys. Rev. Lett. **86**, 4930 (2001).

[162] Y. I. Mazur, W. Q. Ma, X. Wang, Z. M. Wang, G. J. Salamo, M. Xiao, T. D. Mishima, and M. B. Johnson, Appl. Phys. Lett. **83**, 987 (2003).

[163] W. Q. Ma, M. L. Hussein, J. L. Shultz, G. J. Salamo, T. D. Mishima, and M. B. Johnson, Phys. Rev. B **69**, 233312 (2004).

[164] Z. M. Wang, K. Holmes, Y. I. Mazur, and G. J. Salamo, Appl. Phys. Lett. **84**, 1931 (2004).

[165] Z. M. Wang, Y. I. Mazur, J. L. Shultz, G. J. Salamo, T. D. Mishima, and M. B. Johnson, J. Appl. Phys. **99**, 033705 (2006).

[166] V. K. Thorsmølle, R. D. Averitt, M. P. Maley, L. N. Bulaevskii, C. Helm, and A. J. Taylor, Opt. Lett. **26**, 1292 (2001).

[167] G. H. Kim, D. A. Ritchie, C. T. Liang, G. D. Lian, J. Yuan, M. Pepper, and L. M. Brown, Appl. Phys. Lett. **78**, 3896 (2001).

[168] J. Urayama, T. B. Norris, H. Jiang, J. Singh, and P. Bhattacharya, Appl. Phys. Lett. **80**, 2162 (2002).

[169] P. W. Fry, I. E. Itskevich, S. R. Parnell, J. J. Finley, L. R. Wilson, K. L. Schumacher, D. J. Mowbray, M. S. Skolnick, M. Al-Khafaji, A. G. Cullis, M. Hopkinson, J. C. Clark, and G. Hill, Phys. Rev. B **62**, 16784 (2000).

[170] E. C. Le Ru, J. Fack, and R. Murray, Phys. Rev. B **67**, 245318 (2003).

[171] S. Fafard, S. Raymond, G. Wang, R. Leon, D. Leonard, S. Charbonneau, J. L. Merz, P. M. Petroff, and J. E. Bowers, Surf. Sci. **362**, 778 (1996).

[172] A. Hryciw, J. Laforge, C. Blois, M. Glover, and A. Meldrum, Adv. Mater. **17**, 845 (2005).

[173] A. N. MacDonald, A. Hryciw, Q. Li, and A. Meldrum, Opt. Mater. **28**, 820 (2006).

[174] V. I. Klimov, C. J. Schwarz, D. W. McBranch, and C. W. White, Appl. Phys. Lett. **73**, 2603 (1998).

[175] F. Trojánek, K. Neudert, M. Bittner, and P. Malý, Phys. Rev. B **72**, 75365 (2005).

[176] H. K. Nienhuys and V. Sundström, Appl. Phys. Lett. **87**, 012101 (2005).

[177] K. Furukawa, Y. C. Liu, H. Nakashima, D. W. Gao, K. Uchino, K. Muraoka, and H. Tsuzuki, Appl. Phys. Lett. **72**, 725 (1998).

[178] L. X. Yi, J. Heitmann, R. Scholz, and M. Zacharias, J. Phys. Condens. Mat. **15**, S2887 (2003).

[179] J. Wang, X. Wang, Q. Li, A. Hryciw, and A. Meldrum, **in press** (2006).

[180] H. Scher, M. F. Shlesinger, and J. T. Bendler, Phys. Today **44**, 26 (1991).

[181] T. Tiedje, *Semiconductors and Semimetals* (Academic, New York, 1984).

[182] D. S. Ginger and N. C. Greenham, J. Appl. Phys. **87**, 1361 (2000).

[183] F. C. Bos, T. Guion, and D. M. Burland, Phys. Rev. B **39**, 12633 (1989).

[184] S. Etemad, T. Mitani, M. Ozaki, T. C. Chung, A. J. Heeger, and A. G. MacDiarmid, Solid State Commun. **40**, 75 (1981).

[185] R. A. Cheville and N. J. Halas, Phys. Rev. B **45**, 4548 (1992).

[186] P. W. M. Blom and M. C. J. M. Vissenberg, Phys. Rev. Lett. **80**, 3819 (1998).

[187] B. Sturman, E. Podivilov, and M. Gorkunov, Phys. Rev. Lett. **91**, 176602 (2003).

[188] J. Orenstein and M. A. Kastner, Solid State Commun. **40**, 85 (1981).

[189] P. Jund, R. Jullien, and I. Campbell, Phys. Rev. E **63**, 036131 (2001).

[190] R. Chen, J. Lumin. **102**, 510 (2003).

[191] S. P. Withrow, C. W. White, A. Meldrum, J. D. Budai, D. M. Hembree, and J. C. Barbour, J. Appl. Phys. **86**, 396 (1999).

[192] D. Comedi, O. H. Y. Zalloum, and P. Mascher, Appl. Phys. Lett. **87**, 213110 (2005).

[193] E. D. Palik, *Handbook of Optical Constants of Solids* (Academic, London, 1998).

[194] D. McLeod Jr., D. A. Shields, J. E. A. Maurits, and D. H. Forbes, J. Vac. Sci. Technol. A **7**, 1322 (1989).

[195] T. I. Jeon, D. Grischkowsky, A. K. Mukherjee, and R. Menon, Synthetic Met. **135**, 451 (2003).

[196] D. Brüggeman, Ann. Phys. Lpz. **24**, 636 (1935).

[197] D. Stroud, Phys. Rev. B **12**, 3368 LP (1975).

[198] T. C. Choy, *Effective Medium Theory : Principles and Applications* (Clarendon Press, Oxford, 1999).

[199] V. V. Bryksin, Fiz. Tverd. Tela. **22**, 2441 (1980).

[200] J. C. Dyre, Phys. Rev. B **47**, 9128 (1993).

[201] R. B. Laibowitz and Y. Gefen, Phys. Rev. Lett. **53**, 380 (1984).

[202] S. Kirkpatrick, Rev. Mod. Phys. **45**, 574 (1973).

[203] J. P. Clerc, G. Giraud, J. M. Laugier, and J. M. Luck, Adv. Phys. **39**, 191 (1990).

[204] J. J. Wu and D. S. McLachlan, Phys. Rev. B **58**, 14880 (1998).

[205] W. A. Curtin and N. W. Ashcroft, Phys. Rev. B **31**, 3287 (1985).

[206] A. Meldrum, A. Hryciw, A. N. MacDonald, C. Blois, K. Marsh, J. Wang, and Q. Li, J. Vac. Sci. Technol. A **24**, 713 (2006).

[207] V. Teodorescu, M. Ciurea, V. Iancu, and M. Blanchin, Semiconductor Conference **1**, 62 (2004).

[208] C. Busseret, A. Souifi, T. Baron, S. Monfray, N. Buffet, E. Gautier, and M. N. Semeria, Mat Sci Eng C **19**, 237 (2002).

[209] M. L. Ciurea, V. S. Teodorescu, V. Iancu, and I. Balberg, Chem. Phys. Lett. **423**, 225 (2006).

[210] T. Hattori, K. Ohta, R. Rungsawang, and K. Tukamoto, J. Phys. D **37**, 770 (2004).

[211] G. L. Dakovski, B. Kubera, S. Lan, and J. Shan, J. Opt. Soc. Am. B **23**, 139 (2006).

[212] L. Duvillaret, F. Garet, and J. L. Coutaz, IEEE J. Sel. Top. Quant. **2**, 739 (1996).

[213] M. Dressel and G. Grüner, *Electrodynamics of solids : optical properties of electrons in matter* (Cambridge University Press, Cambridge ; New York, 2002).

Appendix A

Experimental considerations

A.1 Water absorption

One of the main sources of noise in the determination of the optical constants by TRTS are the sharp absorption lines of atmospheric water vapour throughout the THz bandwidth. These sharp lines result in an uncertainty in the Fourier transformed pulse amplitude and phase components, which translates into an error in the extracted conductivity spectra. Fig. A.1 shows the time-domain THz pulses in ambient atmosphere, after the setup was sealed and purged with dry-N_2 for 40 minutes, and after 130 minutes. The peak electric field increases with increasing purge time, showing the overall decrease in atmospheric absorption across the bandwidth. Accompanied with the purging, a decrease in the post-pulse ringing also occurs as a result of the decreased absorption. The inset shows the Fourier transform power spectra of these waveforms, where the decrease in water absorption can be observed directly in the disappearance of the sharp dips in the power spectra, specifically at 1.1, 1.7 and 2.2 THz.

The reduction of these sharp dips in the THz power spectra are crucial to obtaining good spectroscopy. Fig. A.2 shows a comparison between the conductivity signal obtained before and after a 130 minute dry N_2 purge. The purged data does not show the rapid variation related to the sharp dips in the absorption and the accompanying phase shifts. In the future, a setup which can be completely evacuated of air would be preferable to eliminate the very long purge time.

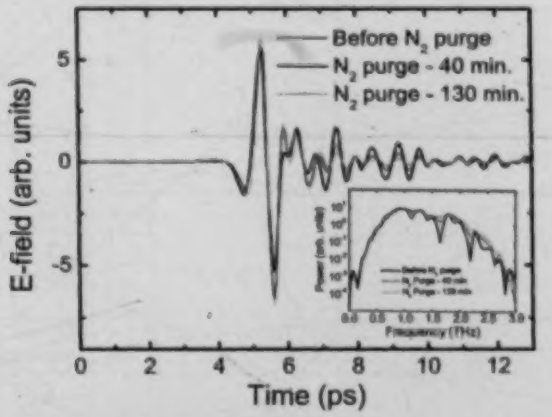

Figure A.1: Time domain data of a THz pulse before and after a 40 and 130 minute dry N_2 purge, showing the reduction of post-pulse oscillations related to water absorption. The inset shows the Fourier power spectrum for these pulses, demonstrating the reduction in water absorption.

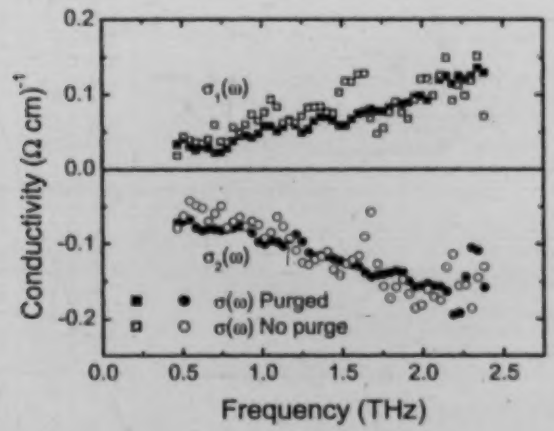

Figure A.2: Comparison plot of the derived conductivity from THz pulses taken without and with a dry N_2 purge, removing atmospheric water vapour from the setup. The sample was a 1 μm thick SiO film on fused silica, annealed at 1000°C in a N_2/H_2 environment after 400 nm excitation.

A.2 Time-domain filtering

One way to reduce the noise in the extracted spectroscopic data due to water absorption is to window out the time-domain response due to the water absorption lines, which ring for 10's of picoseconds after the main pulse. At the same time, however, care must be taken to ensure that we do not introduce artifacts into the data after Fourier transform. Also, one must keep in mind that one is effectively reducing the amount of information in the time-domain data when the pulse is windowed, reducing the number of data points by filtering them out by setting them equal to zero, and so the frequency resolution suffers as a result. Zero padding increases the number of data points so that when performing a Fourier transform, the frequency resolution appears to remain the same, however this is false resolution. One should always do the minimum amount of zero padding to the nearest power of 2, so that a discrete Fourier transform may be performed.

There are many windowing functions routinely used in Fourier analysis of time domain signals, however a common theme is that the functions the signal exponentially at the edges of the window. With this in mind, we have used the function

$$f(t) = \left[\frac{1}{e^{-(t-t_0)/\tau}+1}\right]\left[1 - \frac{1}{e^{-(t-t_0)/\tau}+1}\right] \tag{A.1}$$

to numerically damp the water line oscillations in the time domain, making for much cleaner data in the frequency domain. Fig. A.3 shows an example of the application of this filter function in the time domain, and the resulting smoothing of the power spectrum shown in the inset. When performing complex conductivity analysis, both reference and pumped waveforms must have the same filter applied.

A.3 Spatial filtering

In a TRTS system, the THz beam is usually focused to an approximately diffraction-limited spot, through an aperture upon which the sample is mounted. Because the THz pulse is broadband, with wavelengths stretching from 100 μm to 3 mm and each with its own diffraction limit, any spatial filtering imposed on the pulse will

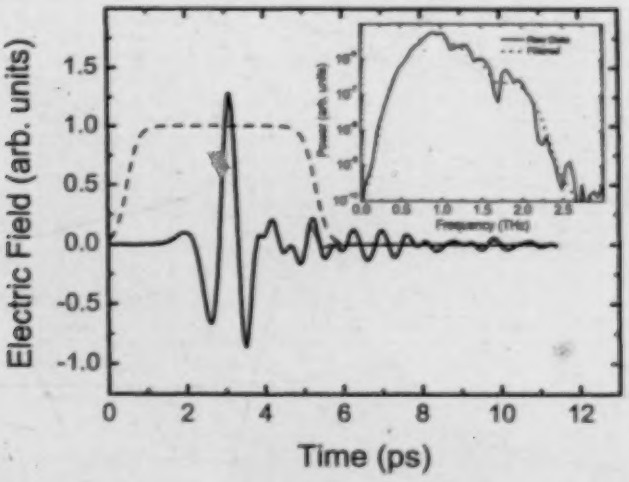

Figure A.3: THz pulse with and without numerical filter (dashed line) in the time domain, and the corresponding power spectrum (inset).

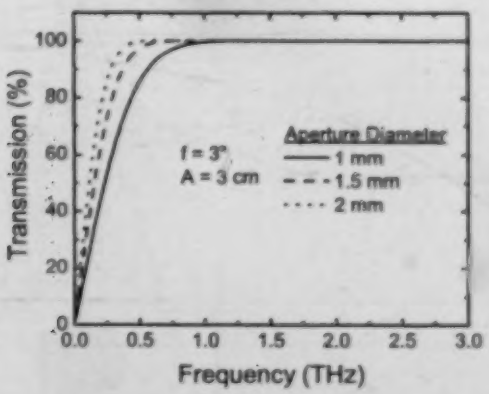

Figure A.4: Calculated transmission function from Eq. A.3 for a diffraction-limited Gaussian THz beam with 1/e width defined by Eq. A.2 through several apertures of indicated diameter. The focal length of the focusing off-axis parabolic was 3 inches and the beam diameter before focusing was estimated as 3 cm, values representative of the THz setup used in this study.

be accompanied by frequency filtering. The minimum radius, w, of a Gaussian THz pulse after focusing (1/e) is given by [210]

$$w = \frac{cf}{A\pi\nu} \tag{A.2}$$

where c is the speed of light, f is the focal length of the off-axis parabolic, A is the beam diameter prior to focusing and ν is the frequency. An aperture is necessary to ensure good spatial overlap of the pump pulse with the THz pulse, and so that the THz pulse sees a material which is more or less uniformly excited across the beam diameter. The power transmission of a Gaussian beam with a 1/e width of w through a circular aperture of diameter z can be calculated to be

$$T = \frac{P_{trans}}{P_{in}} = \frac{\int_{-z/2}^{z/2} e^{-(x/w)^2}}{\int_{-\infty}^{\infty} e^{-(x/w)^2}} = erf\left(\frac{z}{2w}\right) = erf\left(\frac{zA\pi\nu}{2cf}\right) \tag{A.3}$$

where we have substituted in Eq. A.2. Fig. A.4 plots this transmission function as a function of frequency over the THz pulse bandwidth, for three aperture diameters from 1 - 2 mm. In practice, one would like to use the smallest aperture so as to maximize the available pump fluence to excite the sample, but at the same time one can see the lower frequency components are greatly attenuated with a 1 mm aperture below 0.5 THz. As such, for the majority of this study where frequency resolved spectroscopy was performed, a 1.5 mm aperture was used as a compromise.

The majority of the THz power spectrum generated by our ZnTe source is above 0.5 THz, and so this translates into a tighter THz focus than other groups using a photoconductive antenna source which has a peak output at lower frequencies. The diffraction limit for $\nu = 0.5$ THz radiation, assuming a 3 cm diameter beam and a 3" focal length is a 1/e beam radius of 0.5 mm. Fig. A.6 gives the spatial profile of the THz beam at the focus using a knife-edge and a photodetector. The entire THz waveform was taken at each position, Fourier transformed and then integrated over the bandwidth to give an overall power. The spatial profile is fit very well to a Gaussian with a 1/e width of 0.47 mm, indicating that the spot is very near diffraction limited and that the spatial extent of the beam is basically determined by the presence of mainly high frequency components in the pulse.

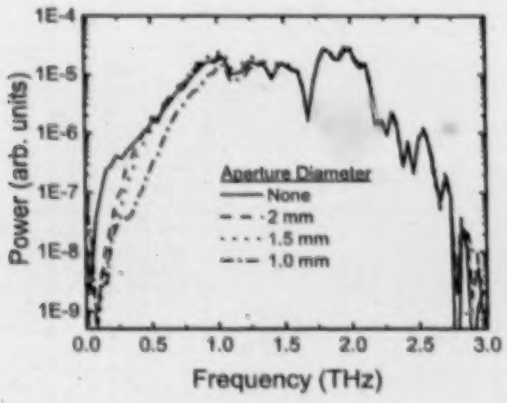

Figure A.5: Power spectrum of a THz pulse transmitted through three apertures of 1.0, 1.5 and 2.0 mm diameter placed at the beam focus.

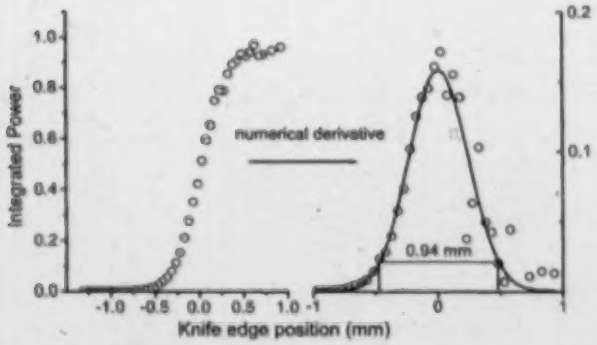

Figure A.6: Spatial profile across the focus of the THz pulse, measured by knife-edge scanning. The line is a Gaussian fit with $1/e^2$ width of 0.94 mm.

A.4 Conditioning of the pump beam

Because of the spatial separation of frequency components at the THz focus, with lower frequencies focused to a larger spot than higher frequencies, one must be careful with the conditioning of the pump beam so that an approximately uniform excitation is acheived across the sample. If the pump beam is not sufficiently large at the sample to provide uniform excitation, higher frequency components will see a higher conducting film than the outlying lower frequency components. Thus, the THz absorption will be artificially shifted to higher frequencies. This effect was first pointed out by Beard et al. [11], and later explored in detail by Dakovski et al. [211]. They found that to avoid a 10% error in the spectrum the pump beam must be 3-4 times the diameter of the THz beam (FWHM). Also, they note that the requirement is relaxed if a metallic aperature is used, as in our setup. In our TRTS setup, we have found that so long as the pump pulse diameter illuminates the entire aperture ($1/e^2$ = 1.5-2 mm) then we see no shift of optical density to higher frequencies. This may be due to the tighter THz focus or, as the authors point out, to the metallic aperture used in all of our THz experiments.

A.5 Conductivity regimes

In photoexcited materials that are well described by a simple Drude model, the electrodynamic response at a given frequency, ω, is determined solely by the scattering time, τ. As mentioned in Chapter 5.1, if the product $\omega\tau \ll 1$ then the response is purely resistive and one can approximate the real conductivity as σ_{dc}. In this situation, the dynamics of the conductivity can be completely characterized by measuring the attenuation of the THz peak, or a so-called one-dimensional scan. If, however, the product $\omega\tau \approx 1$ then the phase shift in the time-domain data prohibits any quantitative analysis of the induced photoconductivity, even though qualitative conclusions can be drawn. Here, we examine two materials, SOS and GaAs, that are well described by the $\omega\tau \ll 1$ and $\omega\tau \approx 1$ regimes respectively, and compare the mobilities extracted from analysis of the one dimensional scans to the more accurate two dimensional scans in both cases.

The conductivity spectra for a 200 nm thick SOS film and a 0.5 mm thick

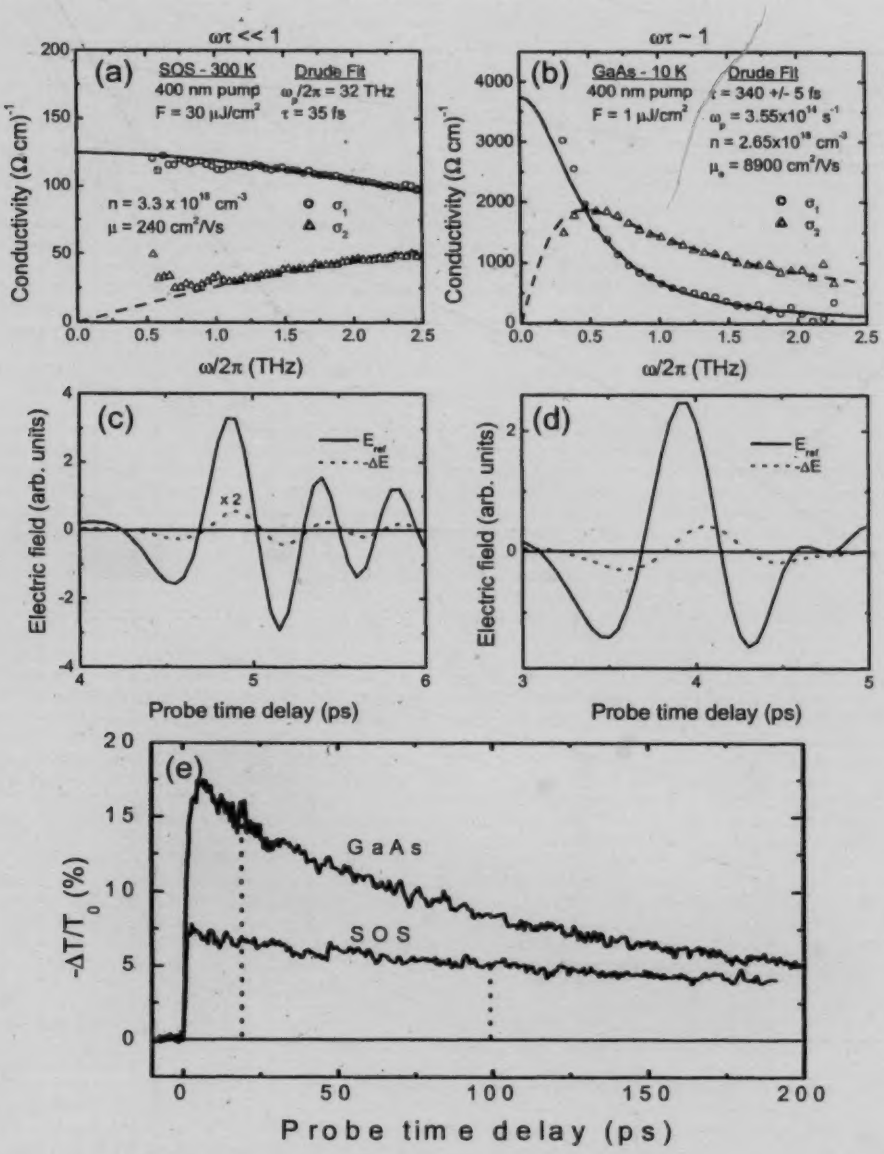

Figure A.7: Transient conductivities of (a) GaAs (10 K, 400 nm pump, 1 μJ/cm^2, 20 ps after excitation) and (b) SOS (300 K, 400 nm pump, 30 μJ/cm^2, 100 ps after excitation). Corresponding $E_{ref}(t)$ and $-\Delta E(t)$ waveforms for the (c) GaAs and (d) SOS samples. (e) $-\Delta T/T_0$ scans for both samples, with the time delay of the spectroscopies indicated.

SI GaAs sample are shown in Fig. A.7(a) and (b), respectively. SOS, with a scattering time of 35 fs, lies in the $\omega\tau \ll 1$ regime and GaAs in the $\omega\tau \approx 1$ regime with $\tau = 340$ fs. Note that these data are similar to the theoretical curves plotted in Fig. 5.3(a) and (c), respectively. The time domain data, E_{ref} and -ΔE, is shown below the conductivity plots in Fig. A.7(c) and (d). In the $\omega\tau \ll 1$ SOS data, the phase shift is small and so the peak of the modulation -ΔE occurs approximately at the THz reference pulse peak. As such, quantitative analysis of the one dimensional scan shown in Fig. A.7(e) can be performed. The 5% modulation at 100 ps after excitation corresponds to $\sigma_{dc} \approx 70$ $(\Omega\ \text{cm})^{-1}$ using Eq. 4.11 with N = 3.17 and d = 82 nm [58]. This is roughly a factor of 2 smaller than the extrapolated $\sigma_{dc} \approx 125$ $(\Omega\ \text{cm})^{-1}$ value in Fig. A.7(a). This discrepancy is likely due to a slight phase shift in the time domain data, from not being completely in the $\omega\tau \ll 1$ limit (35 fs $\times(2\pi)1$ THz = 0.22). We note that this will lead to a reduced μ estimate if the carrier density n is estimated by the pump fluence. The GaAs time domain data in Fig. A.7(d) shows a marked phase shift, and so the -$\Delta T/T_0$ scan in Fig. A.7(e) can only be analyzed qualitatively. For example, the 15% modulation at 20 ps after excitation gives a $\sigma_{dc} = 1220$ $(\Omega\ \text{cm})^{-1}$ assuming N = 3.6 and $\delta_{400nm} = 15$ nm, roughly a factor of 3 lower than σ_{dc}. Therefore, a better estimate of the carrier mobility is obtained by the one dimensional scan in the SOS scenario then the GaAs scenario. Ideally though, the full two dimensional scan is preferred for reliable extraction of the carrier mobility.

A.6 THz-TDS extraction program

The algorithm to extract the complex index of refraction for a thick slab sample (thickness $\gg \lambda$) from THz-TDS transmission data follows the procedure outlined by Duvillaret et al. in Ref. [212]. This algorithm solves the coupled system of nonlinear equations for the index of refraction, n, and the extinction coefficient, k, given a frequency, amplitude and phase of the complex transmission function obtained by measuring the THz pulse with and without the sample in place. The usual method for solving this system of equations is the Newton-Raphson method. This technique is computationally the fastest of all algorithms provided the starting guess of the solution is close enough so that it converges. This requires a very good

This Maple 9.0 program calculates n and k, the real and imaginary parts of the complex index of refraction for a thick material, for a given frequency. It does this by inverting the appropriate Fresnel equations described in the text. It reads in an ASCII file in the same directory as this program with three columns: 1) the radial frequency, omega, in s^(-1), 2) the amplitude of the complex transmission function defined in the text, and 3) the phase of the transmission function. The thickness of the thick slab, L, is entered manually into the program in meters. This assumes that any multiple reflections have been windowed out in time (does not take into account Fabry-Perot effects). The results of the extraction are output to a file called Complex_n.txt in the same directory as the program.

```
> restart;
> L:=0.00051:
> c:=3e8:
> output:=fopen("Complex_n.txt",WRITE,TEXT):
> Data:=readdata("TransmissionData.txt",3);
> out:=array(1..,60,1..3):
> np:=1:
> kp:=0:
> with(LinearAlgebra):
> assume(n>0,k>0,omega>0):assume(n,real,k,real):Amp:=4*sqrt(n^2+k^2)/((n+1)^2+k^2)*exp
  (-k*omega*L/c):
> B:=-(n-1)*omega*L/c+arctan(k*(n^2+k^2-1)/(n^3+2*n^2+n+n*k^2+2*k^2)):
> rho:=ln(abs(Amp))-ln(abs(a)):
> phi:=B-b:
> delta:=rho^2+phi^2:
> A1:=diff(diff(delta,n),n):
> A2:=diff(diff(delta,k),n):
> A3:=diff(diff(delta,n),k):
> A4:=diff(diff(delta,k),k):
> for j from 1 to 60 do
> printlevel:=-1:
> for i from 1 to 4 do
  printlevel:=-1:A:=Matrix([[evalf(subs({n=np,k=kp,a=Data[j,2],b=Data[j,3],omega=Data[
  j,1]},A1)),evalf(subs({n=np,k=kp,a=Data[j,2],b=Data[j,3],omega=Data[j,1]},A2))],[eva
  lf(subs({n=np,k=kp,a=Data[j,2],b=Data[j,3],omega=Data[j,1]},A3)),evalf(subs({n=np,k=
  kp,a=Data[j,2],b=Data[j,3],omega=Data[j,1]},A4))]]);
> Ainv:=MatrixInverse(A):
> del:=Vector([evalf(subs({n=np,k=kp,a=Data[j,2],b=Data[j,3],omega=Data[j,1]},diff(del
  ta,n))),evalf(subs({n=np,k=kp,a=Data[j,2],b=Data[j,3],omega=Data[j,1]},diff(delta,k)
  ))]):
> rp:=Vector([np,kp]):
> rplusone:=evalf(rp-Ainv.del):
> if (i > 3 ) then out[j,1]:=Data[j,1]:out[j,2]:=rplusone.Vector([1,0]):out[j,3]:=
  rplusone.Vector([0,1]) else printlevel:=-1 end if;np:=rplusone.Vector([1,0]):
> kp:=rplusone.Vector([0,1]):end do; end do;
> writedata(output,out,float):
> fclose(output):
```

Table A.1: Relationships between complex optical parameters, given in SI units.

	Dielectric function	Conductivity	Index of refraction
$\tilde{\epsilon}$	$\tilde{\epsilon} = \epsilon_1 + i\epsilon_2$	$\epsilon_1 = \epsilon_b - \frac{\sigma_2}{\epsilon_0\omega}$ $\epsilon_2 = \frac{\sigma_1}{\epsilon_0\omega}$	$\epsilon_1 = n^2 - k^2$ $\epsilon_2 = 2nk$
$\tilde{\sigma}$	$\sigma_1 = \omega\epsilon_2\epsilon_0$ $\sigma_2 = (\epsilon_b - \epsilon_1)\epsilon_0\omega$	$\tilde{\sigma} = \sigma_1 + i\sigma_2$	$\sigma_1 = 2nk\epsilon_0\omega$ $\sigma_2 = (\epsilon_b - n^2 + k^2)\epsilon_0\omega$
$\tilde{n}$	$n^2 = \frac{1}{2}(\epsilon_1^2 + \epsilon_2^2)^{\frac{1}{2}} + \frac{\epsilon_1}{2}$ $k^2 = \frac{1}{2}(\epsilon_1^2 + \epsilon_2^2)^{\frac{1}{2}} - \frac{\epsilon_1}{2}$	$n^2 = \left[\left(\epsilon_b - \frac{\sigma_2}{\epsilon_0\omega}\right)^2 + \left(\frac{\sigma_1}{\epsilon_0\omega}\right)^2\right]^{\frac{1}{2}} + \frac{\epsilon_b}{2} - \frac{\sigma_2}{2\epsilon_0\omega}$ $k^2 = \left[\left(\epsilon_0 - \frac{\sigma_2}{\epsilon_0\omega}\right)^2 + \left(\frac{\sigma_1}{\epsilon_0\omega}\right)^2\right]^{\frac{1}{2}} - \frac{\epsilon_b}{2} + \frac{\sigma_2}{2\epsilon_0\omega}$	$\tilde{n} = n + ik$

initial estimate of n and k with catastrophic convergence failure if the guess is slightly off. The method of Duvillaret has the advantage of being convergent over a much wider range of initial guesses, and is nearly as fast as Newton-Raphson. We outline the technique below and attach Maple 9.0 code which implements this algorithm.

A.7 Relation between optical parameters

As mentioned in the text, it is solely a matter of preference as to whether one refers to the dielectric function, conductivity or index of refraction since they are all related. Following is a table which summarizes these relationships, given in SI units for convenience. Table A.1 has been adapted from a Table given in Ref. [213].

Appendix B

Walk-through tutorial

In this Appendix, we will outline step by step procedures for performing both one and two dimensional TRTS scans, using GaAs as the prototypical sample. This section is meant for future students that may take up the THz setup in their projects, so that they may perform standard spectroscopy by following this written procedure. This by no means suggests that this is the best way to do it, and the reader should feel free to explore ideas for improving the technique.

B.1 The laser system

The output of the Odin multipass amplifier system largely determines the performance and stability of the THz pulse generation and detection, and thus requires some attention. Beyond turning the laser system on, there are a few details which are of particular importance. The output power should be ≈ 600 mW, with a main pulse to pre-pulse contrast ratio of at least 100:1. This can usually be accomplished by adjusting the slit position, and through the adjustment of the Au mirror. Next, the beam spot should be circular with an approximate TEM_{00} spatial intensity profile, which is accomplished by properly aligning the beam through the Teflon pinhole spatial filter before the compressor. Lastly, the compressor setting should be set to ≈ 9 mm, which is about 3.5 mm further than the position which gives the best spark when focusing the output and observing the colour profile on a screen. The best spark usually corresponds to the most colours produced. This compressor setting puts a linear chirp on the pulse, which after passing through

various optical elements on the way to the THz setup, is negated and gives the shortest possible pulse for use. Another way to iteratively find this is to take THz scans at each compressor setting and find the most intense THz pulse with the highest bandwidth.

B.2 Obtaining a THz pulse

The next step, once the laser pulse is directed through the coarse delay stages and down to the THz setup, is to record a THz pulse. First, it is important to ensure that the input 800 nm beams are all aligned to the indicated beam lines on the bench, and that all are at the 6" height. Next, we must overlap the sampling beam with the THz focus at the ZnTe detection crystal. This is accomplished by reducing the power of the generation beam by rotating the $\lambda/2$ waveplate at the entrance to the THz setup. Remove the black polyethylene beam stop before the second parabolic to let the generation beam propagate to the detection ZnTe crystal, where it should fluoresce as a small green spot. This spot is a good approximation as to where the THz focus should be. Next align the sampling beam through the hole in the last parabolic so that it overlaps with the generation beam spot on the crystal. Make sure that at the same time it is going through the center of the parabolic hole, and that it proceeds down the beam line to the polarization analyzer. With a IR viewer, make sure that both arms of the sampling beam after the Wollaston polarizer are illuminating each photodiode without any clipping. Return the black polyethylene beam block and increase the generation beam power to maximum.

Next, we must zero the $\lambda/4$ waveplate so that the polarization into the Wollaston polarizer is circular. This is best accomplished by blocking the THz beam, and syncing the lock-in to the 1 kHz amplifier repetition rate. With the lock-in set to "r-mode", rotate the $\lambda/4$ waveplate until the A-B signal reads zero, or is approximately so. A quick check to verify that each photodiode is reading the same signal is to examine A+B, and block one diode and then the other. They should read be equal and approximately half of A+B.

Now we are ready to detect a THz pulse. The optical chopper modulating the THz generation beam should be turned on, and the lock-in should be synced to its sync-out signal of 270 Hz. After turning on the delay stage unit, the THz Lab-

View program should be opened which will immediately initialize the computer-controlled delay stages to their zero position. After choosing a folder to save the data in, we can move the THz generation beam stage (white stage) to approximately 65 mm. The lock-in should initially be in r-mode, with the A-B output being sent into channel 0 on the DAQ. A typical sensitivity scale is 1 mV. Initially, a lock-in time constant of 30 ms is fine, with the delay between data points set to 120 ms on the LabView program. Scan for approximately 400 points at 100 fs resolution, which should be long enough to locate the THz pulse in time. Next position a 1.5 mm circular aperture at the THz focus, either by hand or with micrometer stage, so that the THz pulse does not change characteristics when the aperture is removed. After placing the sample on the aperture, take another THz scan and note the stage position corresponding to the THz peak by using the fact that 0.15 mm of stage movement corresponds to 1 ps of delay time. After finding the peak, set the lock-in to x-mode and zero the phase.

B.3 One-dimensional scan

With the sample in place and the lock-in reading the THz peak signal, we are now ready to perform a one-dimensional pump-probe scan. After choosing a suitable pump fluence, align the pump beam through the center of the small hole in the parabolic just before the sample so that the pump completely illuminates the sample aperture. With the lock-in synced to 270 Hz, scan the B stage (yellow stage) around the 100 mm position until there is a drop in THz transmission registered by the lock-in. Note the B stage position where this drop occurs, as it defines the zero pump-probe delay time. This scan provides the absolute change in THz transmission, and only the peak scan is needed. An example is shown in Fig. B.1(a), using GaAs taken at 10 K, showing a change in transmission of approximately 20% with a pump fluence of $2\mu J/cm^2$. Next a more sensitive, zero baseline scan is taken by measuring only the modulation of the THz peak, $-\Delta T$. The optical chopper modulating the pump beam is turned on at 540 Hz, and the lock-in is referenced to the sync-out of the chopper. The phase of the lock-in should be zeroed again at this point, and the sensitivity can be increased. The previous scan can be run again, only for longer lengths facilitated by increasing the

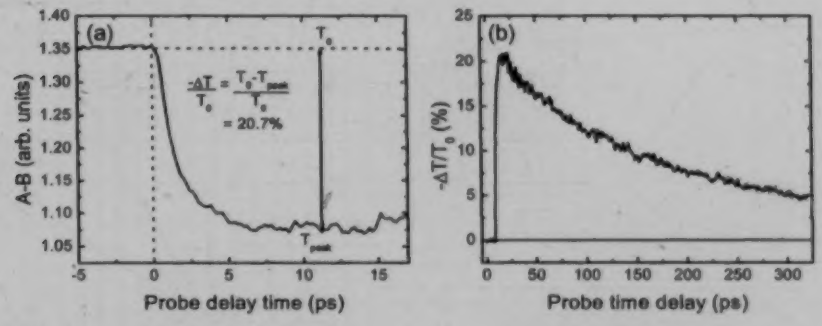

Figure B.1: (a) Absolute change in THz peak transmission and (b) negative differential THz transmission as a function of pump-probe delay time, for a bulk GaAs sample at 10 K, with 400 nm pump at a fluence of 2 $\mu J/cm^2$.

resolution at later times when the decay becomes slower and for multiple averages if so desired. An example of this scan is shown in Fig. B.1(b).

B.4 Two-dimensional scan

The procedure for frequency resolved transient spectroscopy is now outlined. The enclosure is usually sealed and purged with dry nitrogen for up to an hour. Usually THz scans are taken and Fourier transformed periodically while purging until there is no change to the large water absorption lines at ≈1.7 THz, at which point the flow is reduced to a slight overpressure. With the pump beam time delay at large negative times (10 mm away from t=0 is sufficient) a reference scan is taken, with the lock-ins synced to the 270 Hz modulation of the THz source beam and the phase zeroed on the THz peak. The chopper modulating the pump beam is turned off, and the pump beam is let through the blades. Usually the time constant is set to 100 ms on the lock-in, so that the LabView program is set to take data every 400 ms. At least three averages are standard, with each scan of the white stage set to start at least 4 ps before and 8-9 ps after the main peak until the main reflection from the source ZnTe crystal is observed. After the reference scan is measured and recorded in a file, a differential THz scan, -ΔE, must be taken

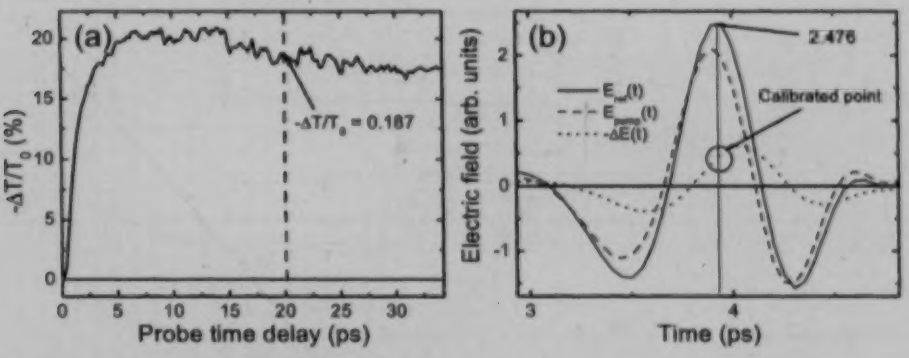

Figure B.2: (a) Scan for calibration of -ΔE(t) waveform. (b) Calibrated waveforms, with the point used for calibration indicated by a circle.

at the desired pump-probe delay time. Turn off the chopper modulating the THz generation beam and let the beam go through the blades. Turn on the chopper modulating the pump, and reference the lock-in to the 540 Hz sync-out signal. Zero the phase of the lock-in for the modulated signal on the peak of the -ΔE. Increase the lock-in sensitivity to the highest level just below saturation. Repeat the same scan performed as the reference, with more averages as needed to obtain sufficient S/N.

B.5 Data analysis

With both E_ref(t) and -ΔE(t) scans, we can extract the complex conductivity of the photoexcited layer. The first task is to calibrate the -ΔE(t) scan, using the one-dimensional -$\Delta T/T_0$ scan. An example is shown in Fig. B.2. At 20 ps after excitation, -$\Delta T/T_0$ = 0.187, shown in Fig. B.2(a). Examining E_{ref} in Fig. B.2(b), the peak value is 2.476. Thus, the -ΔE(t) scan is calibrated so that -ΔE(20 ps) = 2.476 × 0.187 = .463. Once the scan is calibrated, E_{pump}(t) is calculated by E_{pump} = E_{ref}-ΔE, shown in Fig. B.2(b). We now Fourier transform E_{ref}(t) and E_{pump}(t) to $E_{ref}(\omega)$ and $E_{pump}(\omega)$ using the amplitude FFT algorithm in Origin 6.0 to get the amplitudes and phases of the reference and pumped waveforms, shown in Fig.

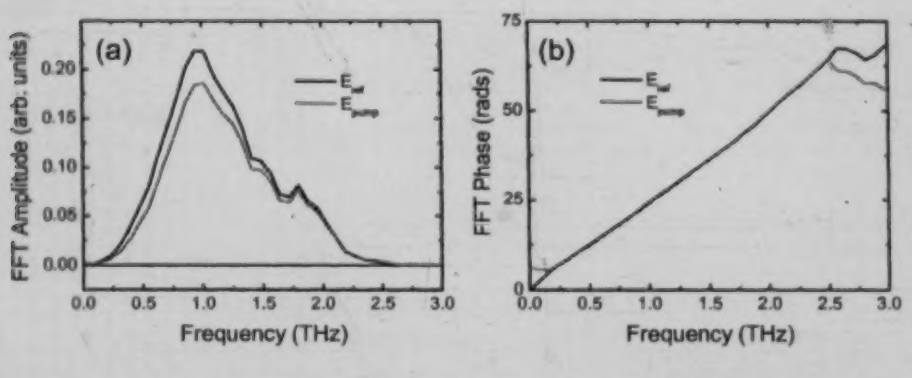

Figure B.3: Fourier transform (a) amplitude and (b) phase of the waveforms shown in Fig. B.2(b).

B.3(a) and (b), respectively. Division of the amplitude spectra in Fig.B.3(a) gives the amplitude of the complex transmission function, $|T(\omega)| = \frac{|E_{pump}(\omega)|}{|E_{ref}(\omega)|}$ shown in Fig. 4.5(a). Subtraction of the phases in Fig. B.3(b) gives the phase of the complex transmission function, $\Phi(\omega) = \phi_{pump}(\omega) - \phi_{ref}(\omega)$, shown in Fig. 4.5(b). Using Eq.'s 4.15 and 4.16, both $\sigma_1(\omega)$ and $\sigma_2(\omega)$ can be obtained analytically from $|T(\omega)|$ and $\Phi(\omega)$, and are shown in Fig. 4.5(c).